Graphene Sensors and Perovskite Solar Cells for Water Detection

A DISSERTATION
SUBMITTED TO THE FACULTY OF
UNIVERSITY OF MINNESOTA
BY

Jungyoon Kim

IN PARTIAL FULFILLMENT OF THE REQUIREMENTS
FOR THE DEGREE OF
DOCTOR OF PHILOSOPHY

Advisor: Tianhong Cui

August 13th, 2020

Acknowledgment

I would like to give my sincere gratitude to my advisor, Professor Tianhong Cui for his constant support and guidance during my Ph.D. study. Professor Cui always inspires me and encourages me to make success in the research. When I lost my motivation by the bad results for publications and fellowships, he always led me in the right direction and supported me with warm words. I believe all my success during my Ph.D. course comes from his great support including doctoral dissertation fellowship. I would also like to express sincere appreciation to the committee members including Professor Terrence Simon, Professor Rajesh Rajamani, and Professor Roger Ruan.

I also got much help from my colleagues in the Technology Integration and Advanced Nano/micro Systems Laboratory. I cannot forget Shota Sando because of his kindness and supportive behavior. I met several great colleagues during my Ph.D. course including Dr. Tianyi Zhang, Mr. Qingyuan Liu, Mr. Peng Zhou, Mr. Chongqui Yang, Mr. Yanke Peng, Ms. Wang Li, Ms. Guihua Xiao and Ms. Jitong Duan. I want to give many thanks for the assistance, and cannot forget all the moments we shared. I would express my special thanks to Legislative-Citizen Commission on Minnesota Resources (LCCMR) for financial support.

Finally, I am indebted to my father, mother, father-in-law, mother-in-law, sister, and brothers-in-law for their endless support. Above all, I appreciate the patience and encouragement provided by my dear wife Kayla Lee. I will try to return all the favors from now on.

Abstract

Water quality test is the first step for cleaning water which is a fundamental element for human health and the environment. The objective of this research is to develop very small, cheap, fast, accurate sensors to detect pollutants including phosphate, nitrate, mercury, and chloride in waters. This is a new testing and analysis technique, which can provide accurate sensing capability to assess the cleanness of waters at a very low cost. The proposed new technology is to manufacture graphene based sensors using the micro-manufacturing. Graphene is a monolayer of carbon atoms with outstanding electrical properties well studied material for a decade by many research groups. Since graphene sensitively responds to molecules in liquids, this property will enable the tiny sensors to detect pollutants in water with very high sensitivity and super short response time to pollutants. Even though graphene responds to the surroundings, it does not have the selectivity to the specific target. In this research, the selective membranes are synthesized and applied to the graphene based sensors to detect the target ions such as nitrate, phosphate, chloride, and mercury. The selective membranes are prepared with two different key materials including molecular imprinted polymer and ionophore. The sensor is characterized by a semiconductor analyzer, and the sensors are tested with several ion solutions to verify their selectivity. The detection limits of the sensor are 0.82, 0.26, 0.87 mg/L and 1.125 μg/L for nitrate, phosphate, chloride and mercury, selectively. In addition, the detection limit of nitrate is enhanced to 0.32 mg/L using the AAO substrate.

Here, this research also includes developing perovskite solar cells as the power source of the sensors. Since solar energy is clean and independent, it is one of the important renewable energy resources. Silicon solar cells have already been commercialized and used to generate electricity in various fields because solar cells can directly generate electricity from photons, and they do not cause a problem to our environment as well. Among several types of solar cells, the perovskite solar cells have been studied by many research groups owing to low-cost fabrication, low fabrication temperature and high efficiency. This research includes the preparation of the materials and fabrication of flexible perovskite solar cells. We also characterize the surface morphology of the perovskite to check the grain size by atomic force microscopy (AFM) and scanning electron microscopy (SEM). The efficiency of solar cells is measured by the solar simulator. We study the relationship between the grain size and the CVD process time and successfully demonstrate the performance of devices. The flexible solar cells show the power conversion efficiency of 7.6 % under the AM 1.5 G. As extended research, we have tried to find the proper hole transport layer (HTL) for the device and applied two HTLs, including PEDOT:PSS and PTAA to the devices.

Table of Contents

List of Figures

CHAPTER 1

INTRODUCTION

1.1 Motivation and Background

Colorimetric detection is one of the widely used current techniques for water quality analysis, which determines the concentration of a target chemical element [1]. The colorimetric method can be used for organic and inorganic compounds. For example, the detection range of nitrate ranges from 1 to 15 ppm with a sensitivity of 1 ppm. It is useful where rough estimation is acceptable and direct monitoring is not necessary. The colorimetric method requires the equipment, a colorimeter, to detect the color difference between samples. This method also requires several time-consuming steps to prepare the samples. For these reasons, it is difficult to expect accurate and fast results with this technique.

Another current approach for water quality analysis uses an ion selective electrode (ISE), which can convert the ion activity in the water into electrical signals [2]. The ISE requires multiple types of membranes for different target ions. The type of membranes includes a compound electrode, solid state, liquid based and glass. Among those, the glass membrane shows an excellent selectivity, but it is only limited to few cations such as Na^+, Ag^+ and H^+. Although the ISE is more selective than the colorimetric method, it still has some disadvantages to be a part of the online water monitoring system. For example, the sensor probe is very fragile and difficult to handle. For this reason, the ISE requires a high maintenance fee. Another disadvantage is that the accuracy of the electrodes is

affected by high concentrations of chloride or bicarbonate ions in the sample water. Fluctuating pH levels can also easily alter the results. To solve those problems, we suggest the ion sensitive field effect transistor using graphene and ion selective membrane.

Graphene is a single layer of graphite that has a two-dimensional (2D) honeycomb structure. It can be distinct depending on the structure. When it is stacked into 3D, it is graphite. It also can be rolled into 1D which is a carbon nanotube. Although it was initially observed by electron microscopes in 1962, Graphene had been rediscovered by Geim and Novoselov in 2014. In the paper, they reported the isolation and properties of Graphene. They won the Nobel Prize in Physic in 2010 with the groundbreaking experiments regarding the two-dimensional material graphene [3]. By discovering the novel material, many research groups started to investigate the material and the applications for a decade. Therefore, the global graphene market has been increasing and is expected to keep increasing within the semiconductors, electronics, and energy fields [4-6].

In the single layer of graphite, the carbon atoms are bonded by sp2 bonds which cause the honeycomb structure. The strong bond makes graphene not only mechanically strong but also chemically inert [7]. It is about 100 times stronger than steel because of chemical bonds [8]. It is also quite stable under harsh conditions. These mechanical and chemical properties make graphene more useful for several applications [9-11]. Among several

properties, the most important property of graphene is electrical properties for sensor applications [12].

Graphene has both properties of conductor and semiconductors [13]. While the valence and conduction bands are overlapped in the conductive materials, the semiconductor has a gap between the conduction and valence bands. Graphene is an excellent conductivity, but it is not a metal. It is categorized as a semiconductor because of its a zero-gap. The conduction and valence bands are not overlapped, but they meet at the Fermi level [14]. Each carbon atom in the honeycomb structure has 6 electrons. Two electrons are in the inner orbital and four electrons are in the outer orbital. Among the 4 electrons in an outer orbital, only 3 electrons are connected to near three other carbons. The left one electron can freely move in a three-dimensional plane which makes graphene highly conductive. The free electrons are called pi electrons which are presented upper and lower in the layer. These pi orbitals in each carbon are overlapped and have bonding and antibonding orbitals which are the valence and conduction band, respectively. The cone shaped 6 overlapped orbitals have a Fermi energy at the intersections where the effective mass of electrons is zero. It causes the new transport mechanism in graphene which is totally different from metals. The charge carriers in graphene can be ballistically moved over the 2D material. As a result, it has a lower resistivity (10^{-6} $\Omega \cdot$cm) than metals at room temperature [15]. Since the electrical conductivity (Fermi level) of graphene can be changed by doping with holes or electrons, there have been a lot of trials for applications [16].

Graphene was discovered by an exfoliation method with scotch tape. It is hard to get a large scale of monolayer graphene with the method. A lot of research groups have been used the chemical vapor deposition (CVD) method to synthesize the large size graphene [17]. In general, Ni film and Cu film are used in the CVD process because these metal films can absorb the carbon source (methane gas) in the surface and form the thin layer graphene sheet. The synthesis process is conducted under high temperature (1000 °C). The synthesized graphene needs to be transferred to the target substrate. Traditionally, PMMA has been used in the transfer process [18]. Although the PMMA method is a stable transfer method, it is difficult to transfer graphene to a specific location in the target substrate. Another transfer method is using a thermal release tape in the transfer process [19]. Handling graphene is much easier with the thermal release tape during the transfer process.

While graphene is an extremely sensitive material to the surroundings, it doesn't have a selectivity [20]. Therefore, the selective membrane is a crucial factor for the graphene based sensors to detect specific ions in water. Two different types of selective membranes are introduced and used in work. The first type is using ionophore based selective membrane. Since there are several commercialized ionophores, it can be used for the fabrication of the membrane solution. Ionophore can recognize a specific ion and bind the ion [21]. The bonded ion can also be released depending on the surrounded condition. The second type of selective membrane is based on a Molecularly Imprinted Polymer (MIP) which is using the molecular imprinting technique [22]. In the MIP, the template

molecule leaves cavities in the polymer matrix to give affinity to the polymer. Once the polymer has an affinity for the specific molecule, it can be used in the graphene based sensor for the selectivity. In this work, ionophore based selective membranes are used for nitrate, chloride and mercury detection. MIP based selective membrane is used for phosphate detection.

A voltage should be applied to the electrodes during the measurement and the sensor measurement system also needs a power source to be operated. Therefore, developing a power source is an important topic for the sensor system. A solar cell is one of the best candidates for the power source because of its cleanness, independence and low price [23]. For the power source in the sensor system, a perovskite solar cell can be used because of high efficiency and low cost. The perovskite has an ABX_3 crystal structure. A is an organic cation (methylammonium or formamidinium) and B is a big inorganic cation (Pb_2^+). X_3 is a halogen anion (chloride or iodide) [24]. Since the material has an optical bandgap (1.48 ~ 2.3 eV), it can generate an electron-hole pair from the visible light [25]. In this work, the perovskite film is fabricated by the CVD process and the processing time is controlled to get a perovskite film which has a large grain size [26]. The perovskite films are synthesized on the flexible substrate to fabricate flexible solar cells.

1.2 Objectives of Research

The first object is developing tiny sensors with graphene, which is very tiny, cheap, fast, accurate, sensitive, and durable for monitoring pollutants in waters. Each sensor will be

designed and fabricated for measuring phosphate, nitrate, mercury, and chlorine in waters. The size of a sensor will be as small as a dime. The sensor system including the sensors will be decreased at least 10,000 times compared to the current existing equipment. We can also expect at least 1,000 times cheaper devices than the bulky machine currently used for water quality detection. I propose a new type of sensor that is accurate, cheap and fast to exchange the current sensor system. Graphene is going to be used as a sensing material in our sensors. Graphene exhibits the following excellent characteristics: first, it is easily applied with current microfabrication technology. Second, it shows high sensitivity due to exposure of species to every single carbon atom. Third, it also shows a low electrical noise level. Last, it can be integrated into tiny sensors. I believe that graphene sensors solve major problems with the current sensors for environmental protection due to its high performance.

The second object is a search and synthesis of the proper selective membranes. Although the graphene sensor has high sensitivity, the graphene doesn't have a selectivity. Therefore, graphene based sensor needs selectivity. The selective membranes will be synthesized using ionophore or MIP for specific ions. Once the selective membranes are successfully synthesized, the membrane will be applied to the sensing area in the sensors. The membrane applied sensors are characterized by two different methods which are resistance change and FET properties. The demonstration of the mechanism is also an objective in this research.

The last aim is to fabricate the flexible perovskite solar cells that can be used in the water monitoring system as a power source. Since solar power is clean and independent, it has been applied to several applications. The perovskite solar cells have a lot of advantages such as high efficiency, low cost, broad absorption range of light, long carrier lifetime, and simple structure. Especially, it can be synthesized to the flexible substrates. For these reasons, the perovskite solar cell can be a great candidate for the power source in the sensor system. The proposed technology will make great impacts on environmental protection and human health safety due to its clean and low-cost analysis method for water analysis.

1.3 Methodology

Graphene is used as a sensing material in IS-FET of Graphene's properties include applicability to microfabrication technology, high sensitivity, long-term stability, and fast response [27]. Figure 1.1 (a) shows the schematic diagram for the structure of the IS-FET and the circuit [28]. The ion selective membrane is coated on graphene surface for detecting target pollutants selectively. Since the selective membrane protects the graphene surface, the sensing components can survive a long time without failure. For the test of the devices, the voltage between drain and source is fixed and the reference voltage is swiped. As a result, we can get the transfer curve of IS-FET which displays Dirac point of graphene.

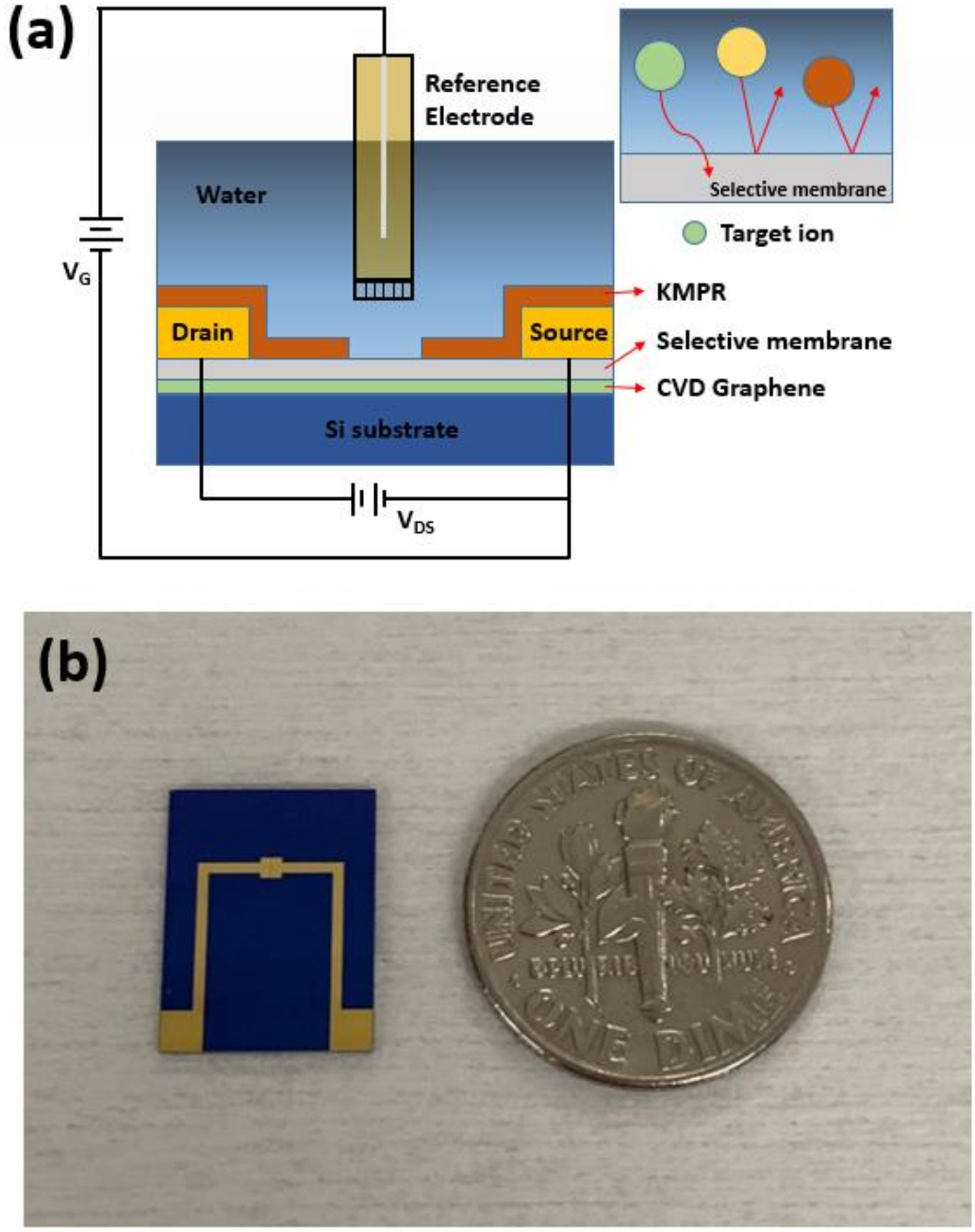

Figure 1.1 (a) Schematic of the graphene based IS-FET (b) Images of the fabricated sensor.

As shown in figure 1.1 (b), the proposed sensor is much smaller than the current existing equipment. The total cost of the sensor system is also at least 100 times slower than the bulky equipment currently used in the water pollutant detection. Besides, the new sensor is small, simple, yet high performance. The novel system can solve the problems of the current system and provide high quality data to us.

The proposed research can develop fundamental knowledge of the device mechanism as it allows the understanding of graphene property and application of it to the novel water monitoring system. Although a zero band gap property of graphene can be a barrier in the semiconductor field, we can make an advantage out of it by using the zero band gap property (Dirac point) for ion detection in IS-FET device. Dirac point change shows the change of the charge carrier density in graphene, and the concentration of solution changes the charge carrier density of graphene [29]. Therefore, the Dirac point shift indicates that the charge carrier density is changed by ions in the solution. It can be also expressed by a surface potential change between the solution and graphene because the surface potential change can affect the carrier density of graphene [30]. For these reasons, the concentration of the target ion can be detected by measuring the Dirac point shift. Theoretically, the Nernst equation can explain the relationship between the solution-membrane interface potential and the target ion concentration [31]. Since the potential drop between the gate electrode and the sample solution is usually fixed by design, the ion concentration only causes the change of the charge carrier density in graphene. The above mechanism needs to be verified and developed through the experiment.

1.4 Thesis Overview

Graphene synthesis and transfer methods are studied and reported in Chapter 2. Graphene is synthesized by the CVD method and the detailed process is described in the chapter. The synthesized graphene needs to be transferred to the target substrates using PMMA or thermal release tape. The synthesized graphene layers are characterized by Raman spectroscopy which can give us information such as quality, thickness and oxidation degree, etc. In the second part in Chapter 2, graphene based sensors are fabricated using MEMs technology including metal deposition, photolithography, etching processes. Two different types of sensors are prepared for the experiment. The first one is graphene based ion sensitive field effect transistor which is the main device in the work and the second type is graphene based sensor that can detect the target materials by measuring the resistance change of graphene. In Chapter 3, the selective membrane is introduced for the selectivity in the sensor. After introducing the selective membrane, the working principle of the devices is discussed in the chapter. In the second part of the chapter, four different selective membranes are introduced for nitrate, phosphate, chloride and mercury detection. The sensors are tested and characterized in this chapter. For enhancing the performance of the sensors, the porous structured AAO substrate is introduced in Chapter 4. First, the fabrication method and characterization of the AAO substrate are depicted in the chapter. Then two different approaches are discussed for nitrate detection and temperature sensor. Each subchapter contains the performance of sensors.

Chapter 5, the perovskite solar cells are introduced and investigated for the power source of the sensor system. First of all, the background and working principle of the perovskite solar cells are discussed. The new type of fabrication process, called the CVD process, is investigated for high efficiency solar cells. In the last part of the chapter, the fabrication process of the flexible perovskite solar cells is studied and the performance of devices is reported. In the final chapter, Chapter 6, the overall results are summarized including the water pollutant sensors and the perovskite solar cells. Future work is also recommended for the additional research work about the graphene based sensors and the perovskite solar cells.

CHAPTER 2

FABRICATION AND CHARACTERIZATION OF GRAPHENE BASED ION SENSITIVE SENSORS

2.1 Graphene synthesis and transfer

2.1.1 Single layer graphene on copper and transfer using PMMA

Figure 2.1 (a) shows a Chemical Vapor Deposition (CVD) system. Graphene was synthesized by the CVD system. The methane gas was used as the source material for the carbon and a Cu foil (Figure 2.1 (b)) was used for a substrate. The Cu foil which has 25-50 μm thickness is annealed at 1000 °C with H_2 gas for 30 minutes to remove the copper oxide layer on the surface.

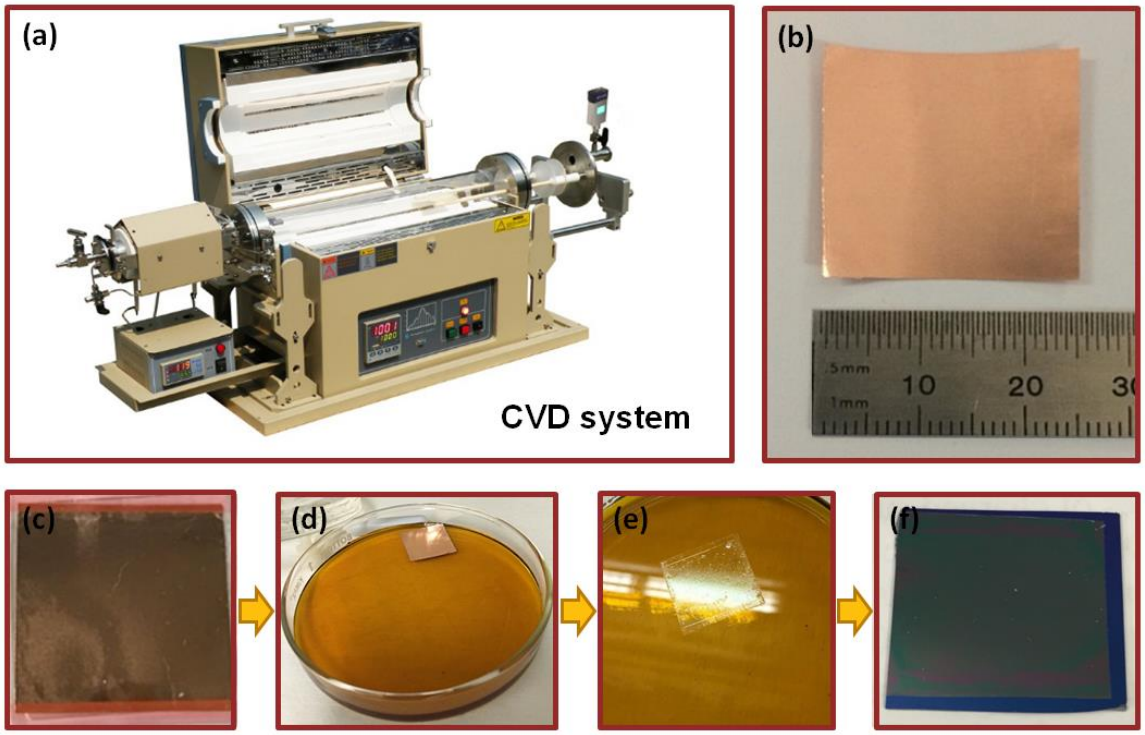

Figure 2.1 (a) CVD system and the procedure of Graphene transfer (b) graphene on the Cu foil, (c) coating PMMA, (d) etching Cu (e) PMMA/Graphene film and (f) transfer PMMA/Graphene on Si/SiO_2 substrate.

Next, the methane gas passed through the chamber along with H_2. In this step, the methane gas decomposed in the high temperature and absorbed into the Cu surface. Graphene seeds randomly formed on the surface of Cu foil and started to grow. H_2, essential gas for graphene growth, has correlation graphene grain size, hence controlling the amount of H_2 gas is a key point in the graphene growth process. After the growing time, the furnace turned off to cool to room temperature [32].

The as-synthesized graphene sheet was transferred to the Si/SiO_2 substrate. The first step

was the coating of PMMA solution on the graphene surface with the spin-coating method. We coated the polymer with 4000 rpm for 1 minute and the coated PMMA film is shown in figure 2.1 (c). For the spin-coating process, the Cu foil needs to be attached to the supporting substrate. After coating, the Cu foil annealed on the hot plate (60 °C for 2 min). Then the Cu foil was floated on the Cu etchant, as shown in figure 2.1 (d). After completely dissolving of the Cu foil into the etchant, the remaining PMMA/Graphene layer can be seen in Figure 2.1(e). After finishing the etching process, the PMMA/graphene layer rinsed to remove the residue of the etchant. Finally, the PMMA/graphene sheet transferred to the objective substrate and dried on the hot plate (80 °C for 2 min). Figure 2.1 (f) shows the transferred PMMA/graphene film on the Si/SiO_2 substrate. The PMMA is removed by acetone.

2.1.2 Multilayer graphene on nickel and transfer using thermal release tape

Figure 2.2 shows the structure of the graphene film and the procedure for the transfer with thermal release tape. Before the graphene synthesis process, Ni needs to be deposited on the Si/SiO_2 substrate using ebeam evaporator. Then the film was thermally annealed to get the large grain size between 1 μm to 20 μm. Graphene was grown on the Ni film under high temperature (900 ~ 1000 °C). As well known, graphene can be grown on the copper and nickel surface [33]. But the synthesized graphene layer can be changed depending on the substrates.

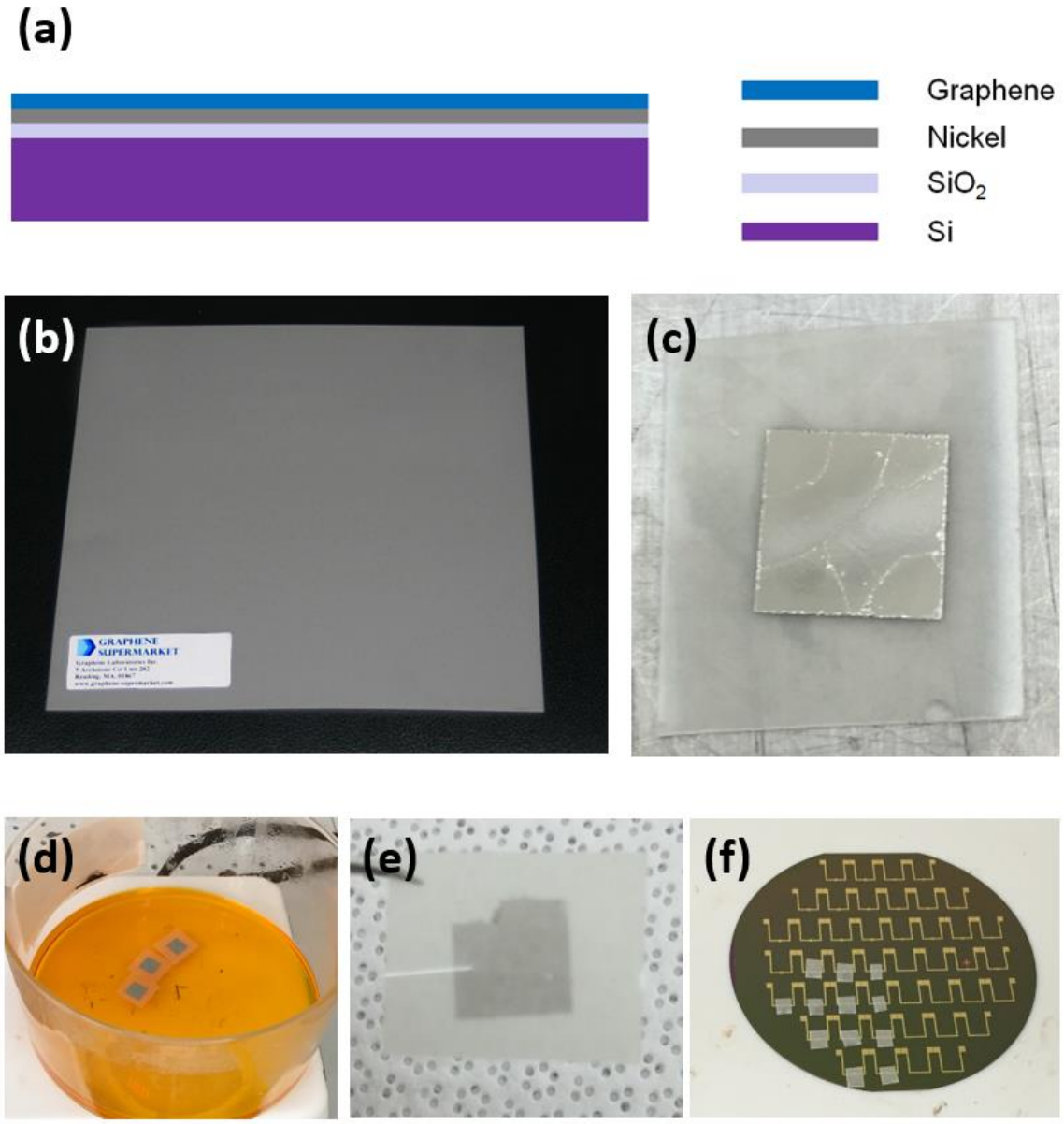

Figure 2.2. (a) Graphene on Ni film structure, (b) Thermal release tape, (c) Transferred graphene and Ni film to the tape, (c) Ni etching process, (e) Graphene on the tape and (f) transfer process to the target location.

This means that the substrate can change the thickness and the grain size of graphene under the same process. There have been some researches about the substrate effect related to Cu, Ni and Cu-Ni alloy. In the research, the growth of graphene on Cu is called a catalytic, self-limiting process and the growth of graphene on Ni is called a C segregation or precipitation process. The result also shows that Ni film usually leads to few layer graphene films, while Cu film leads to a single or bilayer graphene [34]. Therefore, the Ni film was used for the synthesis of few layer graphene films in the research. Figure 2.2 (a) shows the structure of the graphene/Ni on Si/SiO_2 substrate. Thermal release tape is used to transfer the few layer graphene film. Since it is hard to get a continuous film with the transfer method, this method is only suitable for the few layer graphene because of the disadvantage [35]. However, it is a much easier method to handle the graphene during the transfer process. Figure 2.2 (b) shows the commercialized thermal release tape. The tape needs to be attached to the surface of graphene then the Ni film was detached from the Si/SiO_2 substrate. The Ni film can be easily separated in the water. Figure 2.2 (c) is the image of the tape which has graphene and Ni film. In the next step, the Ni film needs to be etched by the etchant as shown in figure 2.2 (d). Figure 2.2 (e) is the graphene image on the tape. After cutting the tape, the tape attached to the target location, like in figure 2.2 (f). Once all graphenes are on the location, the substrate needs to be heated up to 100 ~120 °C which makes the adhesion of the tape weak.

2.1.3 Raman Spectroscopy

The synthesized and transferred graphene sheets on Cu are characterized by Raman spectroscopy. In the Raman spectra, graphene shows three main features, D peak (1350 cm^{-1}), G peak (1582 cm^{-1}) and 2D peak (2700 cm^{-1}) [36]. Figure 2.3 (a) shows the Raman spectrum of graphene on Cu foil. The broad background comes from the surface plasmon emission of Cu substrate [37]. Although there is a broad background band, G peak and 2D peak are demonstrated in the graph. The inset image is the optical image for the surface of graphene on Cu substrate. Graphene sheet transferred on Si/SiO_2 substrate also characterized by Raman spectroscopy.

The result is shown in figure 2.3 (b). After the transfer process, the graphene sheet shows a much clearer G peak and 2D peak than before transfer in the Raman spectrum. Since the forces between stacked graphene layers make 2D peak wider and shorter, the intensity of G peak and 2D peak can show the number of graphene layers [38]. In the spectrum, the intensity of 2D peak is almost 2 times higher than G peak. This means the synthesized graphene is a single layer. In other words, the intensity of 2D peak decreases as increasing the number of graphene layers. The inset of Figure 2.3 (b) is the optical image which shows the transferred graphene sheet on the Si/SiO_2 substrate. In the Raman spectra, we couldn't find D peak which is related to the disorder of graphene structure [39]. These Raman spectra demonstrate that the synthesized graphene sheet is a single layer and doesn't have defects.

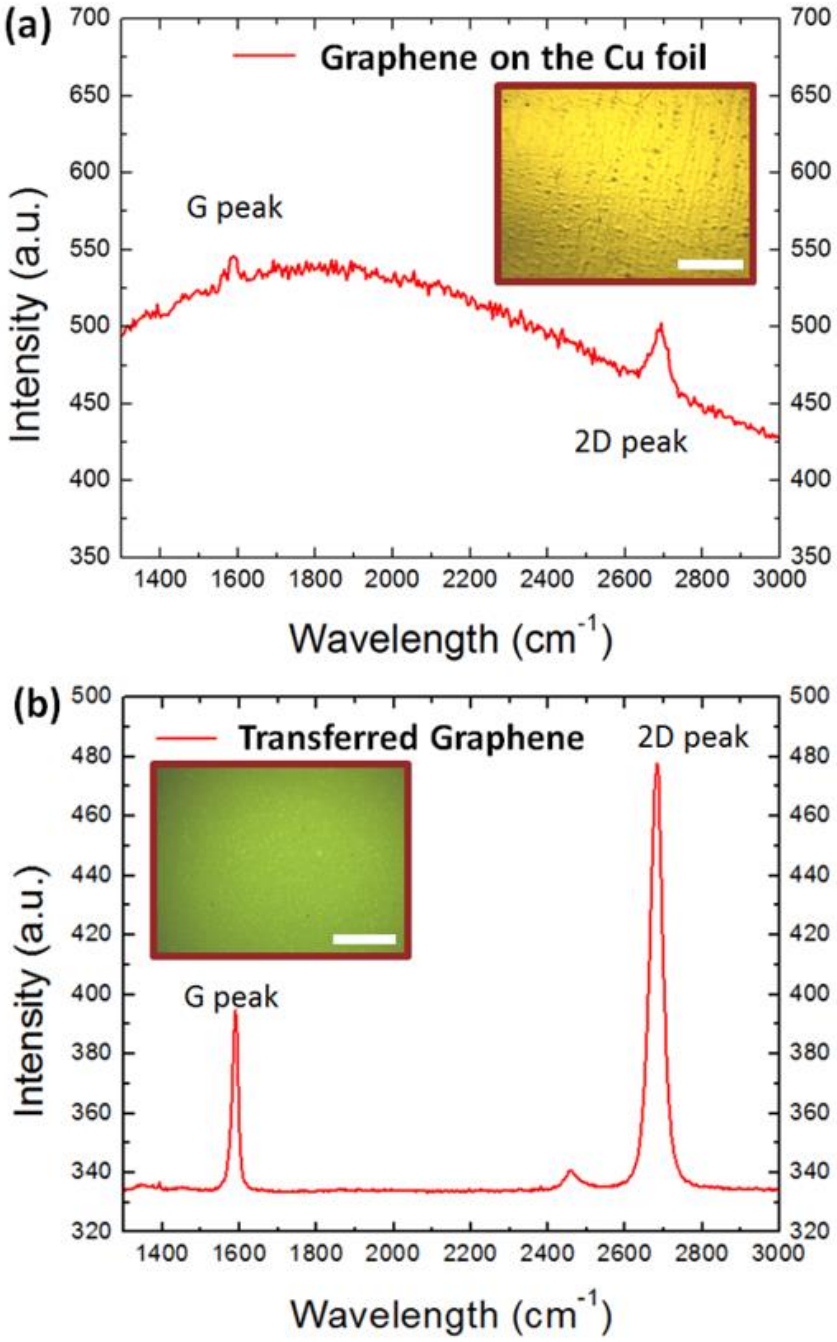

Figure 2.3 Raman spectroscopy of single layer graphene from Cu film (a) before transfer and (b) after transfer. Insets are the optical image of Graphene on Cu foil and Si/SiO_2 substrate (scale bar is 10 μm).

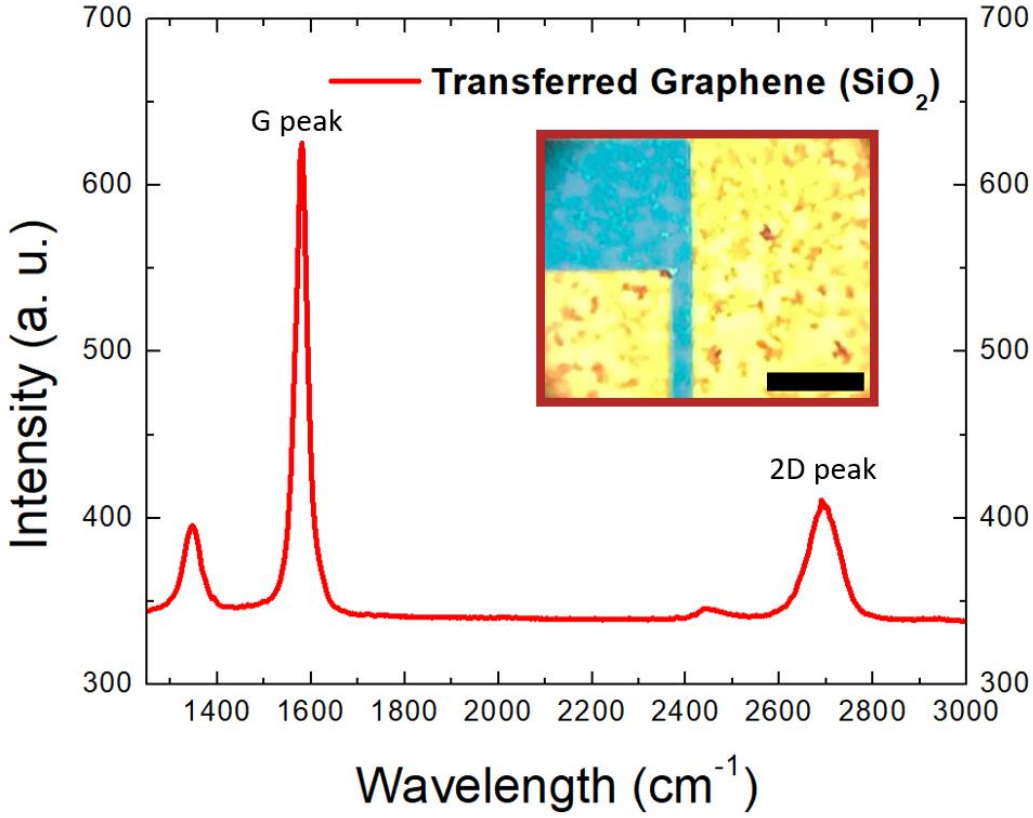

Figure 2.4 Raman spectroscopy of few layer graphene from Ni film. Insets are the optical image of Graphene on Si/SiO_2 substrate (scale bar is 10 μm).

Figure 2.4 shows Raman spectroscopy of few layer graphene which was transferred from Ni film. For the measurement, the synthesized graphene was transferred to Si/SiO_2 substrate and measured by Raman spectroscopy. The inset image is the optical image of the transferred graphene on Si/SiO_2 substrate. The grains of graphene are observed in the image because it has about 4~5 layers of graphene. In the graph, there are three main peaks for graphene. The difference between the results is the intensity of the peaks. The

relationship between the ratio of peak intensity and the thickness of graphene has been well investigated by several research groups [40,41]. In terms of the single layer of graphene, the ratio of the peaks between G and 2D peaks was opposite to the result from the few layer graphene. The intensity of 2D peak was much stronger than G peak for the single layer graphene but the intensity of G peak was stronger than 2D peak for the few layer graphene. The results demonstrate that the transfer with thermal release tape was successful and confirm that the number of graphene layers.

2.2 Fabrication of Ion Sensitive Field Effect Transistor

2.2.1 Device structure and fabrication

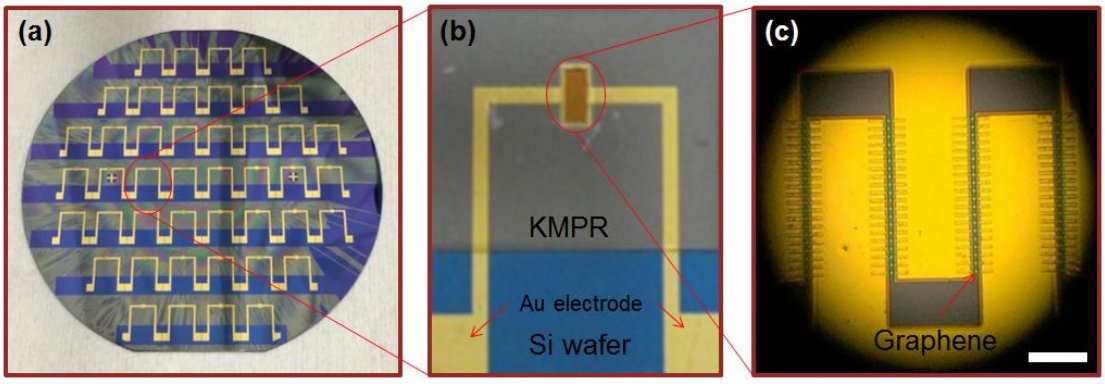

Figure 2.5 Structure of CVD Graphene sensor (a) 44 sensors in the wafer, (b) Each sensors structure, and (c) Optical image of sensing part (the scale bar is 10 μm).

Figure 2.5 (a) shows 44 sensors fabricated on the Si wafer. To fabricate electrodes, Cr (30 nm) and Au (100 nm) were deposited on Si wafer and wet-etched after UV photolithography. Graphene was transferred between the electrodes in the sensing area

and patterned with oxygen plasma. Last, we coated KMPR to cover electrodes parts and patterned the KMPR to open the graphene area. This KMPR can prevent leaking current through the solution by covering electrodes. In figure 2.5 (b), the structure of the device is depicted. Figure 2.5 (c) is the optical image of the sensing region which has an interdigitated shape. The graphene sheet is located between the electrodes and connects both electrodes. The electrodes are fully covered with KMPR, but KMPR was patterned using UV photolithography to make a window between electrodes. We will measure the interaction between solutions and Graphene through the window. O-ring was attached to the sensing region to reserve the solution during the measurement.

2.2.2 Performance of the devices

Figure 2.6 shows the response of the CVD graphene sensor. The two different phosphate buffer solutions (pH6 and pH8) and the different concentrated sodium nitrate ($NaNO_3$) solutions were used for the measurement. To perform pH sensing experiments, a wetting and drying process was used. After the resistance of the device was stabilized, the pH6 buffer drop was carefully placed on top of the sensing region which is inside o-ring. And then the buffer solution was changed with pH8 buffer solution after the resistance became stable. When we changed the solution, the previous solution should be removed from the sensing region with careful pipetting. Because the remained buffer solution could affect the next solution, it is important to suck up the previous buffer solution.

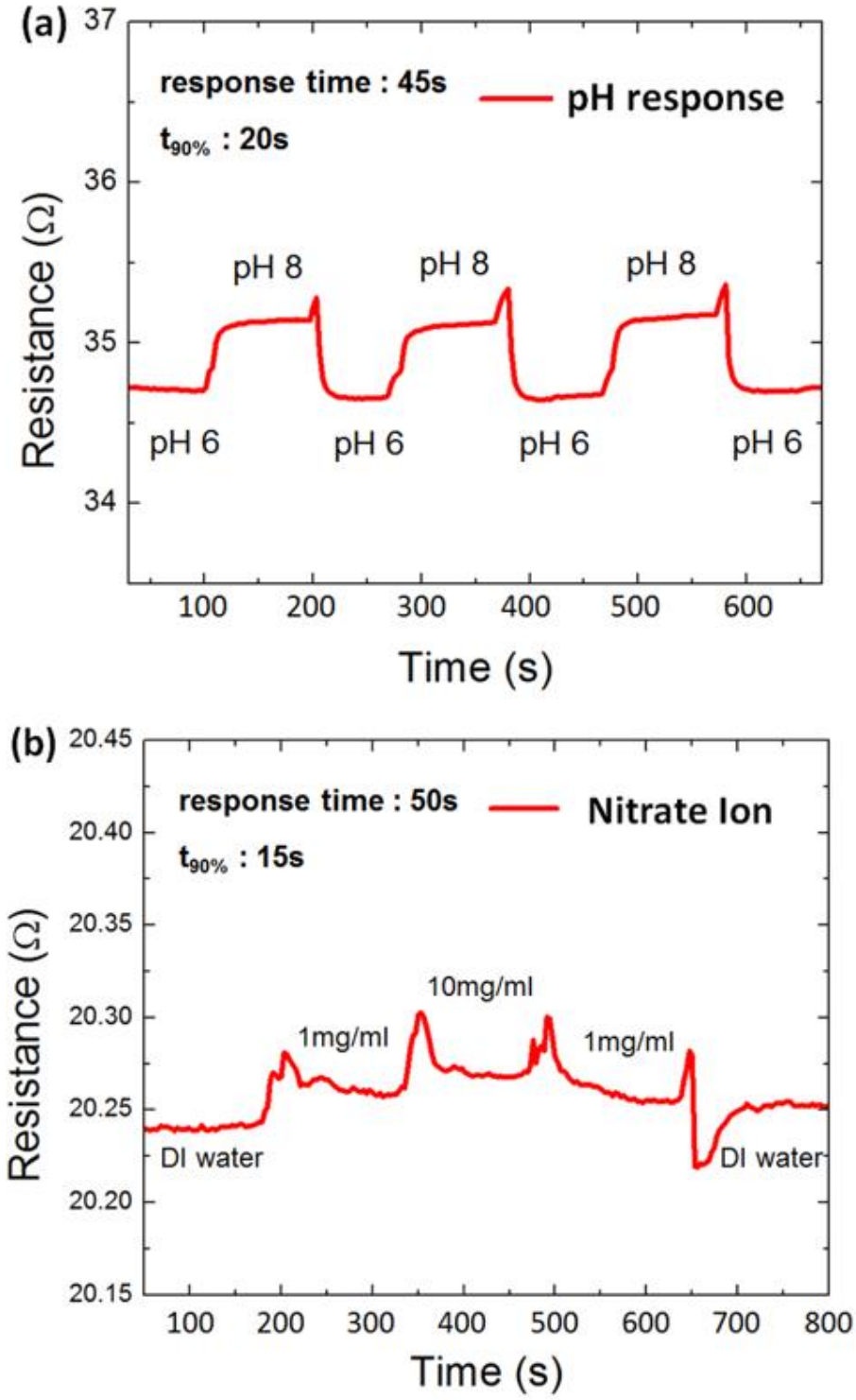

Figure 2.6 Response of Graphene sensor with (a) Buffer solution and (b) Nitrate ion solution.

Figure 2.6 (a) shows the resistance depends on the different pH solutions. In the CVD graphene case, the results demonstrated that the graphene has n-type property which is opposite to p-type [42]. Since the main carriers are electrons in the n-type graphene, the resistance is decreased with pH6 buffer solution. In other words, H^+ ion attracted electrons in the graphene sheet and the current easily flows between the electrodes [43]. In contrast, the resistance is increased with a pH8 buffer solution. The response time was 45 s and T90 %, the time to reach 90 % of final value, was 20 s.

For sensing the nitrate ion, the nitrate ionophore solution was coated on the graphene before applying the $NaNO_3$ solution. The synthesis method will be discussed in the next chapter. This membrane allows only nitrate ions and blocks other ions. By using this selective membrane, we can detect nitrate ions in the solution. Figure 2.6 (b) is the response of the sensor with $NaNO_3$ solutions which have different concentrations. Since the NO_3^- ions repel the electrons in the graphene sheet, the resistance was increased as increasing the amount of ions. The response time and T90 % were 50 s and 15s, respectively.

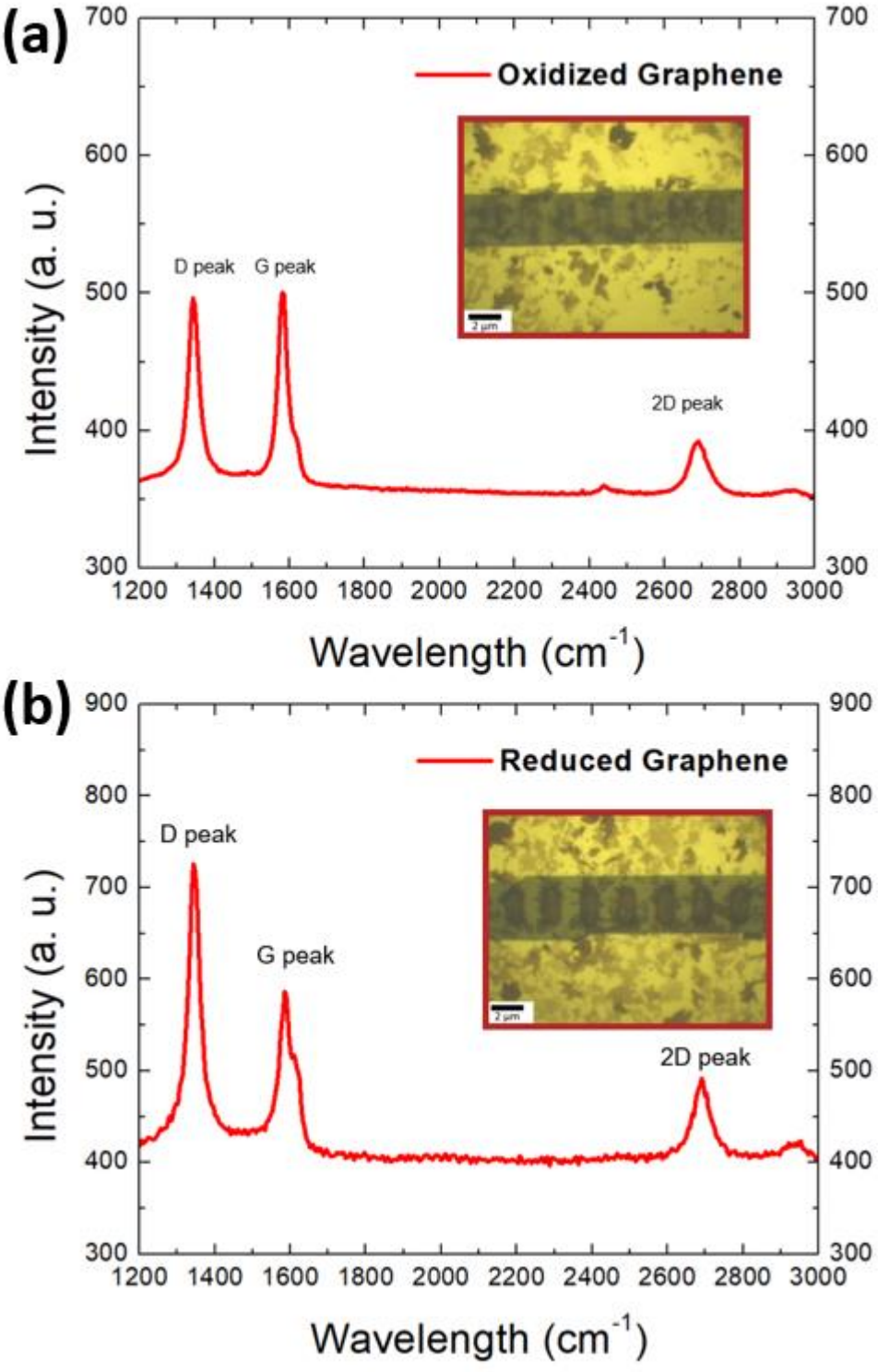

Figure 2.7 Raman spectroscopy after measuring the resistance change.

As described above, the resistance measurement of graphene is an available method for sensing pH and ion in water. However, there is a serious disadvantage to the measurement. When the resistance was measured by the equipment, the applied voltage in graphene causes the oxidation and reduction of graphene [44]. Once graphene changes to the graphene oxide or reduced graphene, the properties of the material are changed [45]. As a result, the resistance can be keep changed by the electrochemical reaction. Figure 2.7 (a) shows Raman spectroscopy which shows the three main peaks for graphene oxide including D, G and 2D peaks. In the graph, the intensity of D peak is much enhanced compared to Raman spectroscopy of the pristine graphene. This means that the graphene was oxidized during the measurement. Figure 2.7 (b) shows Raman spectroscopy of the reduced graphene. Although the graph in figure 2.6 (a) and (b) shows quite stable results, it was hard to get those stable data due to the oxidation and the reduction.

2.3 Conclusion

In Chapter 2, the synthesis of graphene in two different substrates has been discussed. Also, the graphene transfer method was investigated for the fabrication of sensors. First, the single layer of graphene was synthesized by the CVD method on Cu foil and transferred to the Si/SiO_2 substrate using PMMA. The transferred graphene was characterized by Raman spectroscopy. The result showed that the synthesized graphene was a single layer. Next, the few layer of graphene was synthesized on Ni film which is

deposited on Si/SiO_2 substrate. The graphene was successfully transferred from Ni film to the Si/SiO_2 substrate with thermal release tape. The thickness of graphene was also confirmed by Raman spectroscopy.

The graphene based sensors were fabricated and the performance was tested by measuring the resistance change. The sensors were tested for the pH and nitrate ion measurement. Although the sensor worked for the target materials, the oxidation problem of graphene was observed after the measurement. This means that graphene is not a suitable material for the sensor. During the measurement, the applied voltage causes the oxidation in graphene. The oxidation was confirmed by Raman spectroscopy. For this reason, the resistance measurement system was changed to the solution gated field effect transistor measurement system because the applied voltage doesn't need to be high in the new measurement system. The detailed structure of the sensor and system are discussed in the next chapter.

CHAPTER 3

SELECTIVE MEMBRANE AND VARIOUS IONS DETECTION OF GRAPHENE SENSORS

3.1 Nitrate Detection

In this work, we report the fabrication of ion sensitive field effect transistor which can detect nitrate in the water, and we clarify the sensing mechanism using a membrane-solution potential change model. For the device, CVD graphene is used for a sensing

material and a polymer based nitrate selective membrane is used for the selectivity. While graphene can very sensitively respond to the surrounding environment, graphene needs the selectivity to detect specific ions in water. To solve the problem in graphene based sensor, the selective membrane including nitrate ionophore, PVC and plasticizer is directly applied to the graphene surface. The quantity of nitrate in water is estimated by measuring the Dirac point shift of graphene with a semiconductor analyzer because Dirac point sensitively responses to a graphene's carrier density which can be changed by the membrane-solution potential difference. Nitrate is the only ion that can be recognized by the selective membrane. Therefore, the sensor can detect the quantity of nitrate in water without the interference of other ions. In the experiment, four different solutions (phosphate, sulfate, chloride and nitrate) are applied to the sensors to test the selectivity and four different concentrations (0.1, 1, 10 and 100 mg/L) are used for the sensitivity test. The detection limit is 0.82 mg/L, and the response time is about 10 seconds.

3.1.1 Introduction

The fertilizers have been increased by agricultural production to satisfy our demand. With increasing the consumption of agricultural products, the usage of the fertilizer has also been increasing. Nitrate is one of the major components of fertilizer [46]. Increasing the amount of nitrate in the soil also results in the rise of nitrate in water [47]. Another source of nitrate is cattle urine. The high concentration of nitrate in water is the major concern in New Zealand because the cattle farming rate has been significantly increased

over the last two decades [48]. Since nitrate from the fertilizers and urine dissolve into the drinking water, human being and other lives are exposed to water that contains highly concentrated nitrate. Even though nitrate is an essential element of our body and ecosystem, an excessive amount can cause various problems such as eutrophication in water and health problems in animals. The high concentration of nitrate in surface water can make algae and phytoplankton growth. The eutrophication leads to depleted oxygen in water resulting in fish kills [49]. For the human body, excessive nitrate can cause heart problems for the infant. It is called blue baby syndrome. The body color of infants shows blue because of the lack of oxygen [50]. Therefore, it is necessary to detect and control the concentration of nitrate in water.

To measure the concentration of nitrate in water, various methods have been developed, such as colorimetric devices, conductometric sensors, and ion-selective electrodes that have high accuracy and low detection limits [51-53]. However, these methods still need to be overcome the following disadvantages. The colorimetric method needs several pretreatment processes for preparing the samples, and the conductometric method can cause an electrochemical reaction such as reduction and oxidation during the measurement. These reactions cause the noise in the sensor response. The precision of the ion-selective electrode is rarely better than 1%. But it still can be affected by other ions. These mentioned processes have a complicated fabrication process, and the samples need to be prepared by trained people. Besides, equipment is expensive and complex to operate.

Here, we suggest graphene based ion-sensitive field effect transistor (IS-FET) for the simple, cheap, sensitive and accurate nitrate sensor. IS-FET is a FET used to measure ion concentrations in solution. Although several research groups have studied the topic, no one used the hybrid film which consists of chemical vapor deposition (CVD) graphene and nitrate selective membrane to the IS-FET for nitrate detection yet [54]. In this paper, we focus on the synthesis process of the hybrid film, the sensor fabrication and the mechanism of the sensor. In terms of the hybrid membrane, each layer has a different function. Graphene is used for the sensing material and the nitrate selective membrane including nitrate ionophore is used for the selectivity of the sensor. After discovering graphene, the synthesis methods of graphene and graphene derivatives have been intensively studied to apply the materials for various applications such as diodes and solar cells to substitute metal electrodes and other functional layers because of its electrical conductivity [55-59]. Although a zero band gap property of graphene can be a barrier in the semiconductor field [60], we can take advantage of it by using the zero band gap property (Dirac point) for ion detection in an IS-FET device. Dirac point change shows the change of the charge carrier density in graphene, and the concentration of solution changes the charge carrier density of graphene. Therefore, the Dirac point shift indicates that the charge carrier density is changed by ions in the solution. It can also be expressed by a surface potential change between the solution and graphene because the surface potential change can affect the carrier density of graphene. For these reasons, the concentration of the target ions can be detected by measuring the Dirac point shift.

Although graphene has the sensitivity to the ions in water, it still needs the selectivity. To solve this problem, we synthesize the nitrate selective membrane solution and directly coat the solution on the graphene. The selective membrane is PVC based polymer membrane with the nitrate ionophore.

Theoretically, the Nernstian equation can explain the relationship between the solution-membrane interface potential and the target ion concentration. Since the potential drops between the gate electrode and the sample solution are usually fixed by design, the ion concentration only causes the change of the charge carrier density in graphene. The fabricated sensors are characterized by a semiconductor analyzer with several ionic solutions (chloride, phosphate, sulfate and nitrate) and different concentrations (0, 0.1, 1, 10 and 100 mg/L). IS-FETs show the Dirac point shift from 0 V to 0.3 V with nitrate solutions. However, the devices do not show a clear shift with other ion solutions. We successfully demonstrate the relationship between the Dirac point shift and the nitrate concentration in the graphene based IS-FET.

3.1.2 Fabrication of graphene based sensor

Graphene is synthesized by the CVD method [61]. Cu foil (25 μm) is used as a substrate for graphene. Then the cleaned Cu foils are located in the furnace to anneal the Cu film under Ar/H_2 atmosphere at 1000 °C.

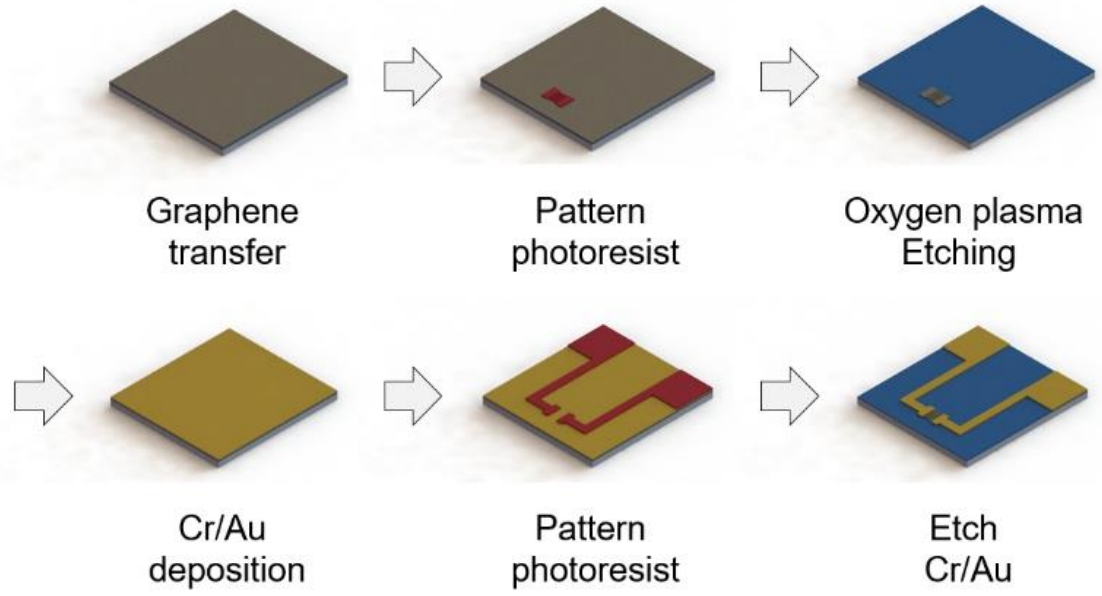

Figure 3.1 Fabrication flow chart for graphene based IS-FET.

In this annealing process, the grain size of Cu is increased. At this point, the H_2/CH_4 gas can be absorbed in the Cu foil. The absorbed methane gas diffuses out to the surface and forms the graphene layer during the cooling down process. The monolayer graphene is successfully synthesized on the Cu foil [62]. Figure 3.1 shows the fabrication flow chart of the graphene based IS-FET device. First, we need to transfer the graphene to the target substrate. Thermal release tape is used for the transfer process [63]. The thermal release tape is attached to the graphene. Then the Cu foil etches in the Cu etchant for 1 h. Before the transfer process, the target substrates need to be cleaned by oxygen plasma etching. This process increases the surface energy of the substrate. It is important to transfer graphene to the SiO_2/Si substrate right after the oxygen plasma process for the successful transfer. Then remove the tape under the temperature (120 °C). The thermal release tape

loses the adhesion at the temperature. As described in figure 3.1, the transferred graphene needs to be patterned by photolithography. For the electrodes, the Cr/Au (30/100 nm) films are deposited by an e-beam evaporator and patterned by another photolithography process. The fabricated graphene FET is characterized by Raman spectroscopy and semiconductor analyzer.

3.1.3 Synthesis of the nitrate selective membrane

Figure 3.2 (a) shows the procedure of the synthesis procedure for the nitrate selective membrane. The membrane consists of three main materials including polyvinyl chloride (PVC), plasticizer and nitrate ionophore [64]. PVC is the polymer as the base material in the membrane. After adding ionophore in the polymer solution, the PVC solution needs the plasticizer to form the membrane. 1-(2-Nitrophenoxy)octane (NPOE) is used as the plasticizer. NPOE is well-known as a highly lipophilic plasticizer in polymer membrane fabrication. First, PVC powder 90 mg (45 wt%) is dissolved in 2 mL of the tetrahydrofuran (THF) which is a main solvent for the membrane. The nitrate ionophore mixture 30 mg (15 wt%) adds to the prepared solution before adding NPEO in the solution. The ionophore mixture consists of Methyltriphenyl phosphonium bromide, nitrocellulose, moistened with 2-propanol and tridodecyl-methyl ammonium nitrate. For the final step, 80 mg (40 wt%) NPOE adds to the THF solution including PVC and ionophore. The synthesized solution is coated on the surface of the device using a spin-coater (2000 rpm for 30 s).

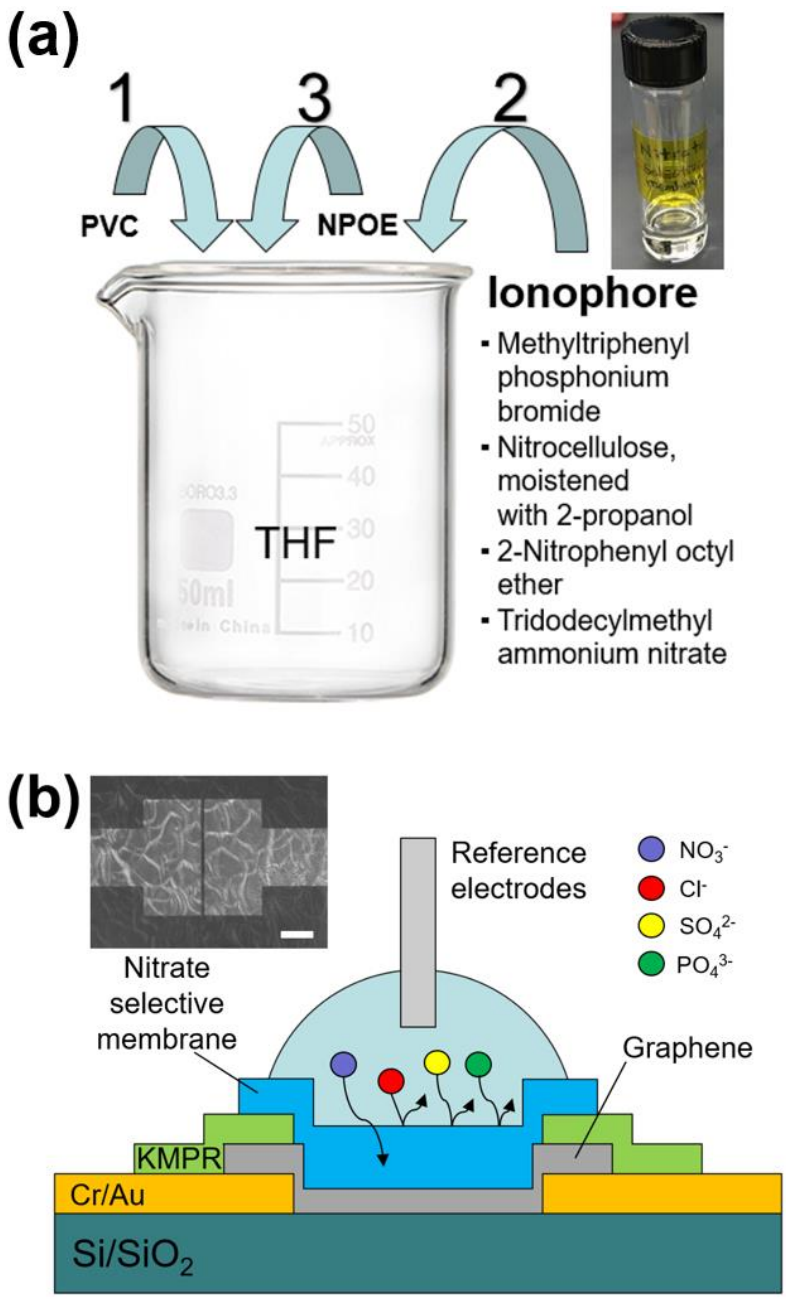

Figure 3.2 (a) Schematic diagram for the synthesis of nitrate selective membrane. Inset image shows the synthesized solution in (b) Schematic diagram for the mechanism of nitrate selective membrane. Optical image shows the surface of the sensing area after coating the membrane. Scale bar is 10 μm.

The order of the procedure is important for the synthesis of the membrane solution. As shown in the inset image, the solution is transparent. The solution has a higher viscosity than water as the polymers are dissolved in THF. Figure 3.2 (b) depicts the side view of the device structure to explain the mechanism of the nitrate selective membrane. There are three electrodes in the structure including the source, drain and reference electrodes. The graphene layer is between the source and drain electrodes on the Si/SiO_2 substrate. The nitrate selective membrane is coated on the graphene. The ionic solution is located between the graphene/selective membrane and the reference electrode. Dirac point of graphene can be shifted depending on the concentration of the ionic solution because the charge carrier density in graphene can be changed by the potential difference between the solution and the selective membrane [65]. This potential change shows the doping effect in graphene [66]. The nitrate can only be recognized by the nitrate selective membrane [67]. Therefore, we can only detect the relationship between the nitrate concentration and the Dirac point shift without the interference of other ions in the solutions, using the nitrate selective membrane. The performance of the IS-FETs and the detailed mechanism is demonstrated in the results and discussion section.

3.1.4 Fabricated sensor structure and transferred graphene

Figure 3.3 (a) shows the sensor structure and the circuit for the measurement. In the measurement, the V_{DS} is fixed to 0.05 V and the V_G is swept from -1 V to 1 V.

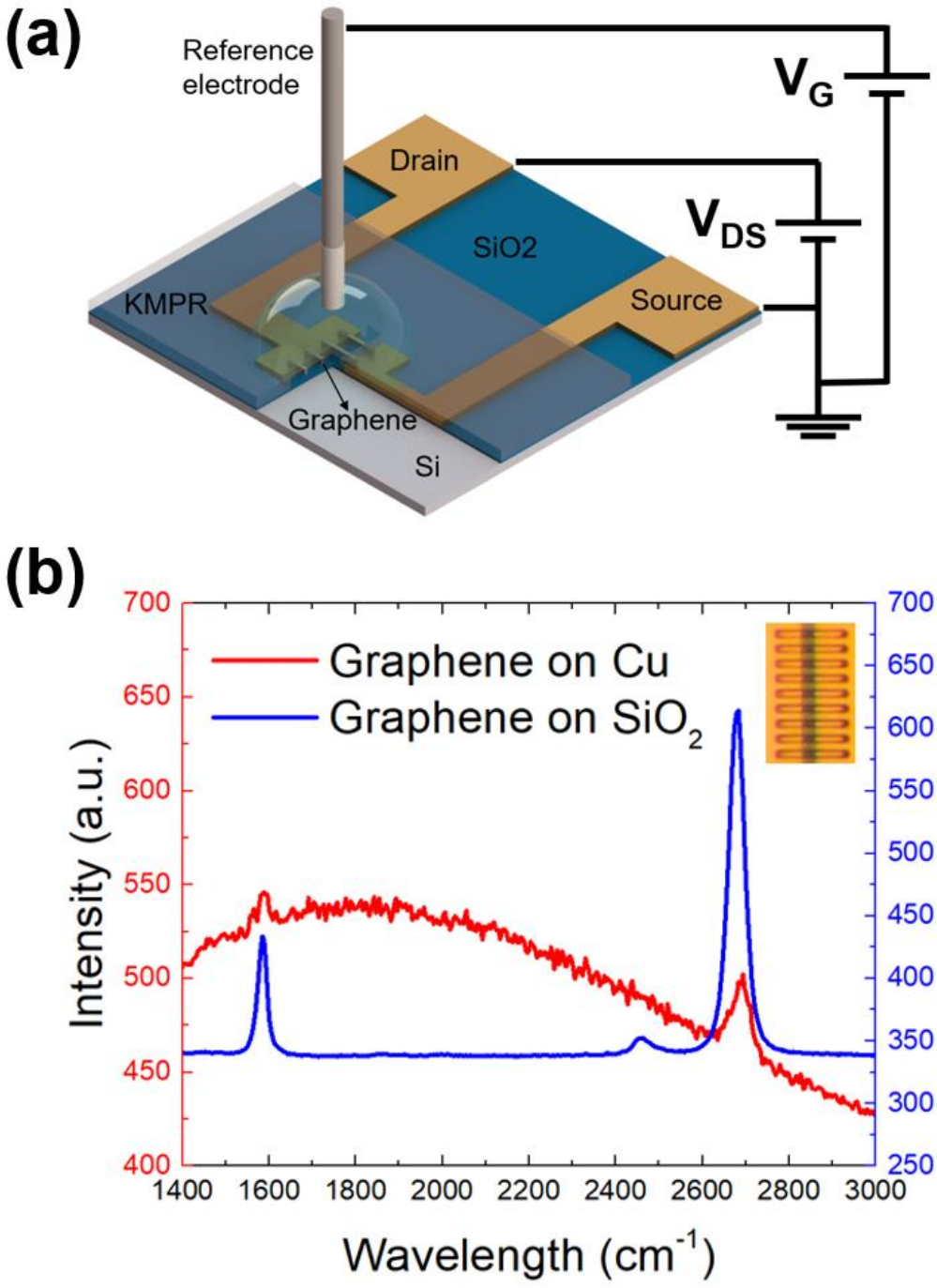

Figure 3.3 (a) Schematic diagram of graphene IS-FET (b) Raman spectroscopy of graphene on Cu and SiO_2. Inset image shows an optical image of the sensing area.

The voltage between the drain and source electrodes should be less than 0.1 V to prevent graphene from oxidation because graphene can be easily oxidized by the voltage. We use the Ag/AgCl as the reference electrode. Although the other metal electrode can also be used as the reference electrode, the Ag/AgCl electrode can provide a stable gate voltage [68]. As shown in the illustration, the KMPR layer protects the Au electrodes from the solution. KMPR, a negative photoresist, is coated on the device to block the leakage current from the electrodes to the solution.

The graphene layer is only exposed to the solution through the patterned KMPR windows. Before and after the graphene transfer process, graphene is characterized by Raman spectroscopy. In figure 3.3 (b), the red curve demonstrates the Raman response of graphene on the copper substrate. The blue curve shows the response after the transfer process. The two main peaks including G (1530 cm^{-1}) peak and 2D peak (2700 cm^{-1}) are shown in both graphs [69]. Since the red curve includes the broad peak that comes from the copper substrate, the intensity of the peaks is much higher in the SiO_2 substrate. However, the G and D peaks are in the same position. We also confirm that the synthesized graphene is monolayer with the peak intensity ratio between G and D peaks in the graph. The inset image in figure 3.3 (b) shows the sensing area. In this sensing area, there are 9 patterned graphene strips between two Au electrodes. The device performance is described in the following section.

3.1.5 Measurement and mechanism of the devices with the nitrate selective membrane

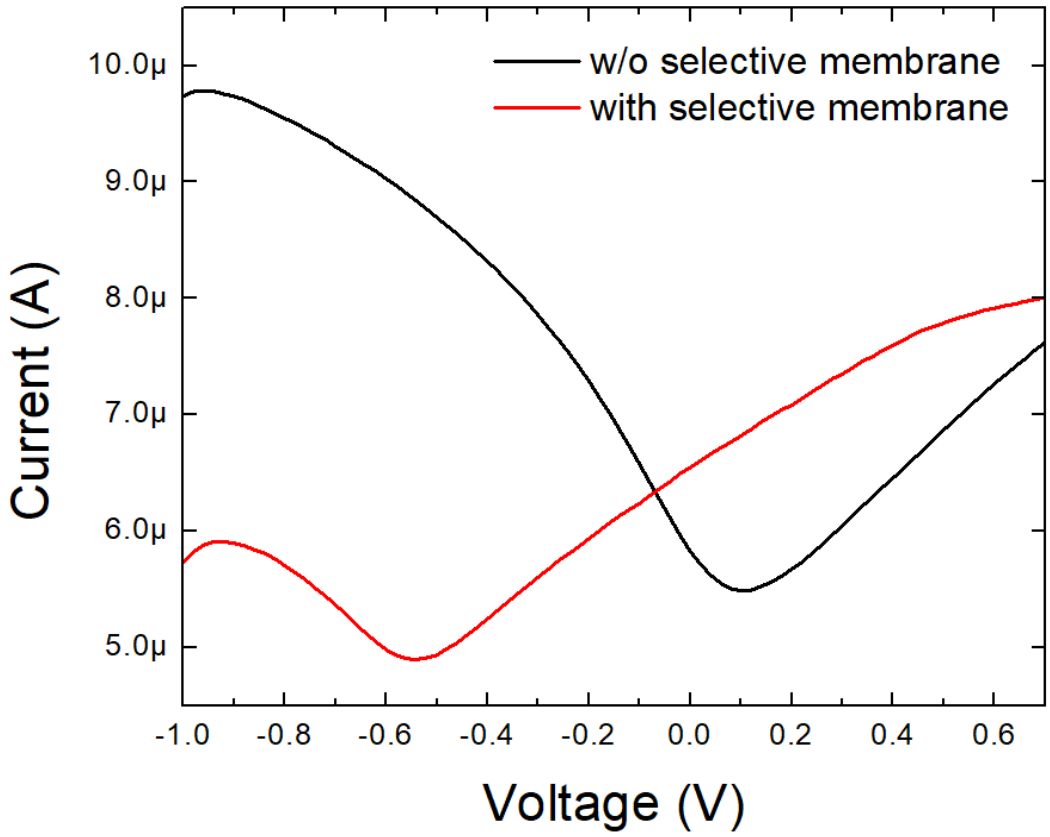

Figure 3.4 Transfer curve of graphene FET before and after coating the nitrate selective membrane.

The IS-FETs are tested by a semiconductor analyzer. For the measurement, deionized (DI) water is used. The graphene based IS-FET shows Dirac point in DI water. First, Dirac point of graphene is measured before and after coating the nitrate selective membrane on the sensing area. Figure 3.4 shows the transfer curve of the IS-FET. The black curve is the response without the nitrate selective membrane, and the red curve

shows the response of the sensor after coating the membrane. Before coating the membrane, Dirac point is located on the right side (about 0.1 V) from the origin in the graph. This means that graphene shows p-type property due to the residues and the defects in the graphene surface. The residues and the defects on graphene can cause the p-doping effect to graphene [70,71]. As a result, the main carrier in graphene is holes. However, the main carrier is changed from holes to electrons after coating the selective membrane. In the red curve, the location of Dirac point is changed to the left side (about -0.55 V) from the origin. This means that the main carriers are electrons after coating the membrane. The electrical charge of the selective membrane can cause the doping effect on graphene [72]. Our results also support this phenomenon.

As shown in Figure 3.4, Dirac point, the lowest point of the current level, is located on the negative side in the graph after coating the nitrate selective membrane. Figure 3.5 shows the responses of the IS-FET with different solutions (chloride, sulfate, phosphate and nitrate) that have different concentrations (0.1, 1, 10, 100 mg/L). The black curves are the responses of the device in DI water. Every sensor shows the same location of Dirac point at -0.55 V with DI water. The prepared different solutions are applied to the IS-FET, and we measure the shifts of Dirac points. As increasing the concentration, Dirac points are shifted from -0.55 V to the right side (p-doping effect). In other words, Dirac point is also increased by increasing the concentration of solutions because of the potential change between graphene and solutions.

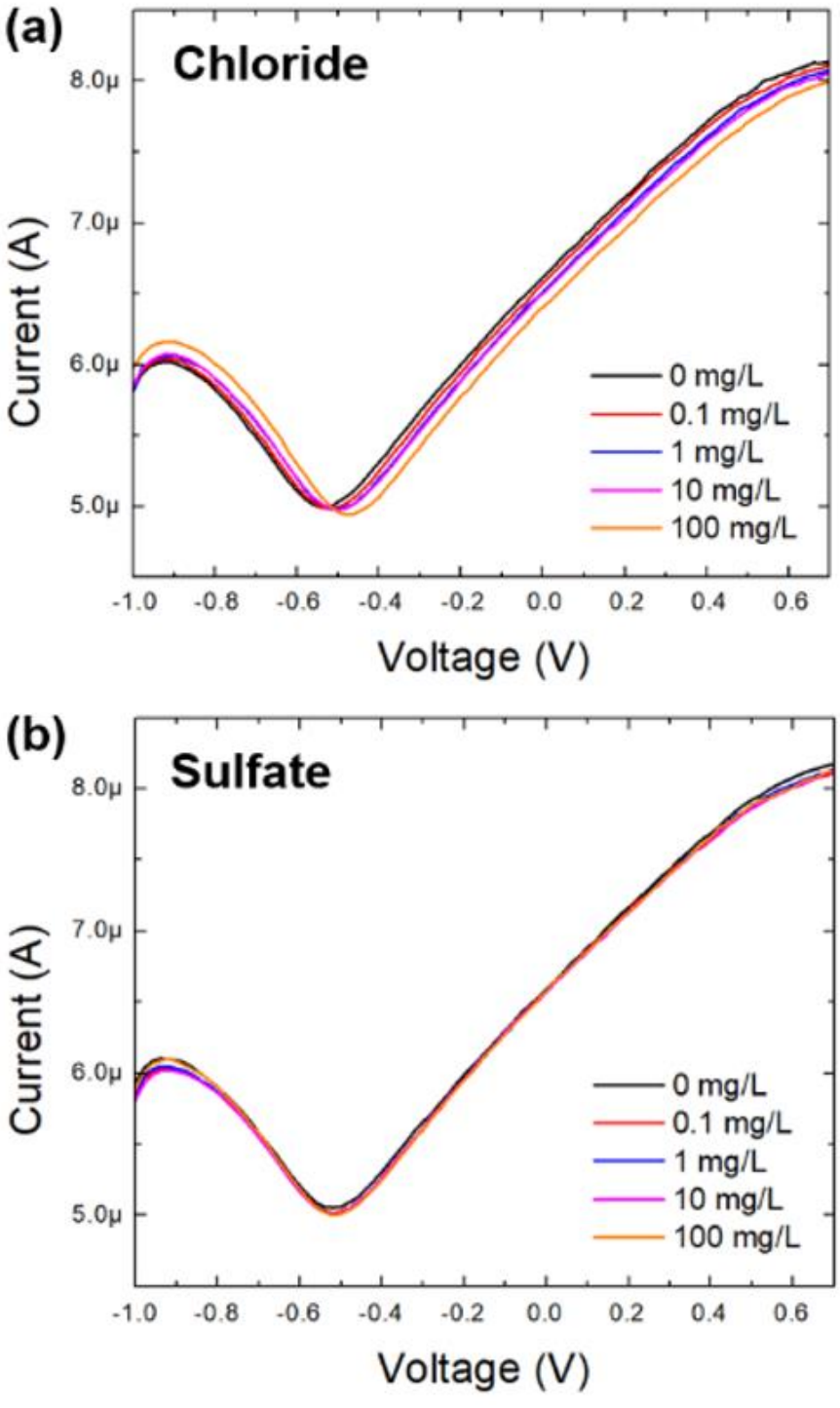
(a)
Chloride
8.0µ
7.0µ
6.0µ
5.0µ
Current (A)
-1.0
-0.8
-0.6
-0.4
-0.2
0.0
0.2
0.4
0.6
Voltage (V)
0 mg/L
0.1 mg/L
1 mg/L
10 mg/L
100 mg/L
(b)
Sulfate
8.0µ
7.0µ
6.0µ
5.0µ
Current (A)
-1.0
-0.8
-0.6
-0.4
-0.2
0.0
0.2
0.4
0.6
Voltage (V)
0 mg/L
0.1 mg/L
1 mg/L
10 mg/L
100 mg/L

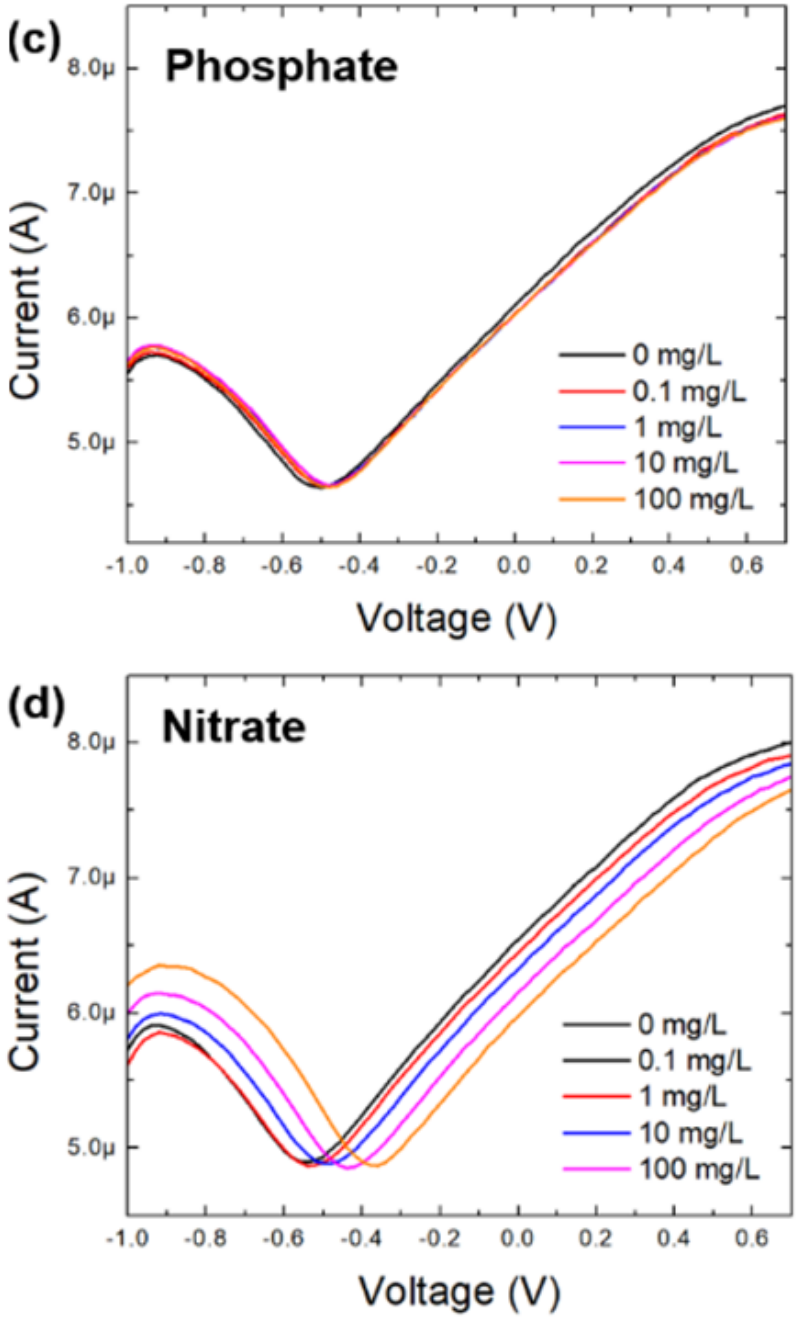

Figure 3.5 Transfer curves of graphene IS-FET with the nitrate selective membrane. Four different solutions were applied to the sensor. Sensor responses with (a) Chloride, (b) Sulfate, (c) Phosphate and (d) Nitrate solutions.

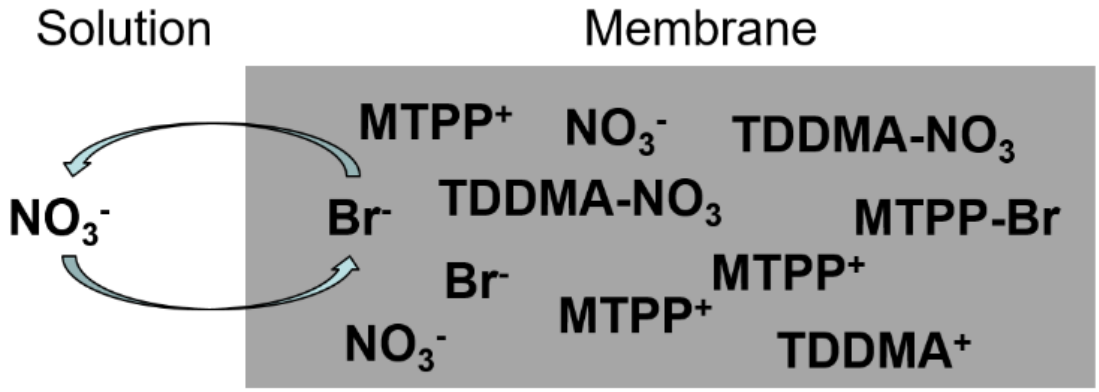

Figure 3.6 Schematic diagram for the working mechanism of the nitrate selective membrane.

Figure 3.6 shows the working mechanism of the nitrate selective membrane. The membrane consists of Methyltriphenylphosphonium (MTPP)-bromide and Tridodecylmethylammonium (TDDMA)-nitrate as an ion exchanger and ionophore, respectively. When the membrane encounters the water, the bromide and nitrate ions dissolve in the solution for the equilibrium [73]. Since the membrane has a positive charge after losing ions, Dirac point is shifted to the left side in the graph, as shown in figure 3.4. As increasing the concentration of nitrate in water, the nitrate can be attracted by TDDMA which has a selectivity for the nitrate. The overall charge of the membrane can be balanced by exchanging the bromide in MTTP-Br with the nitrate. Therefore, the membrane can keep absorbing the nitrate maintain the charge balance. Dirac point is shifted to the right side as increasing the concentration of nitrate in the solution because the selective membrane loses its positive charge [74].

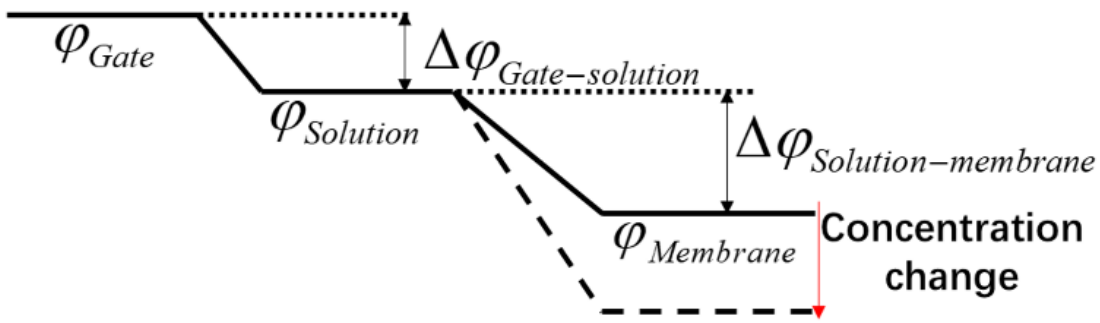

Figure 3.7 Illustration of the potential change between the gate and the membrane.

The sensing mechanism can be explained by the ion concentration induced solution-membrane interface potential change. Figure 3.7 indicates that the potential drop from the gate electrode to the membrane interface is dominated by the interface potential between the sample solution and the membrane. The potential drop between the gate electrode and the sample solution is usually fixed by design [75]. Therefore, the relation between the solution-membrane interface potential and the target ion concentration can be given by the Nernstian Equation [76].

$$\Delta\phi_{Solution-membrane} = \phi_{Solution} - \phi_{Membrane} = E_{const} + \frac{RT}{F}\ln\frac{a_{Ion}(sol)}{a_{Ion}(mem)}$$

Where E_{const}, R, T, F are the target ion species related to constant, gas constant, temperature, Faraday constant, respectively. $a_{Ion}(sol)$ and $a_{Ion}(mem)$ are the ion activities in the solution and in the membrane, which can be decided by the ion concentrations. Since the ion concentration in the ion selective membrane is a fixed value, the interface potential is determined only by the ion concentration in the solution. Therefore, the ion concentration causes the change of the charge carrier density in graphene.

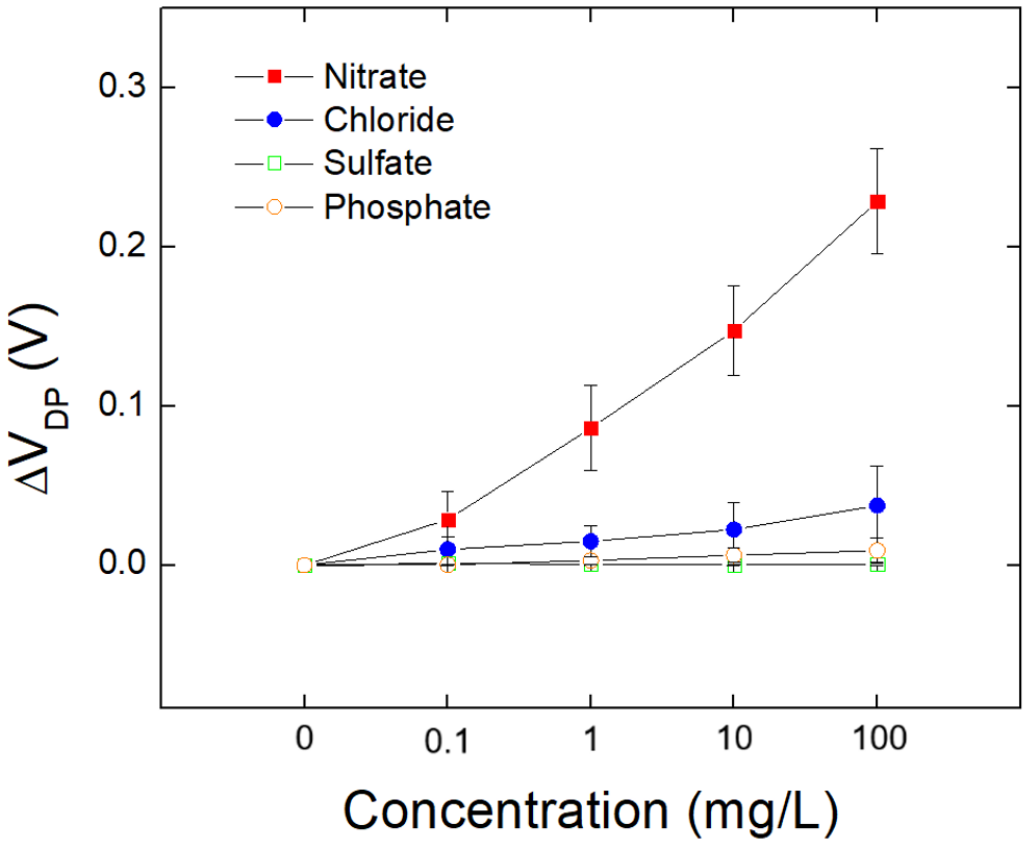

Figure 3.8 Selectivity of the nitrate selective membrane.

The prepared solutions are applied to the sensors to check the selectivity of the IS-FETs, the shifts of Dirac point and measured. The measurement is conducted under the same condition. V_{DS} is fixed to 0.05 V, and the gate voltage is swept from -1 V to 1 V. Figure 3.8 demonstrates the gate voltage shifts of the sensor depending on the concentrations. The origin of Dirac point is about -0.55 V, and the amount of shift (ΔV_{DP}) varies depending on the solutions. For the nitrate solution, ΔV_{DP} is increased up to 0.25 V as increasing the concentration. However, the ΔV_{DP} does not change with other solutions. In other words, the nitrate solution only gives the doping effect on graphene. Although the sensor shows a small response to the highly concentrated chloride solution, it is acceptable for drinking water due to the higher EPA standard for chloride of 250 mg/L. The calculated detection limit is 0.82 mg/L which is lower than the EPA standard (10 mg/L). The selectivity test is conducted with several sensors and the results are presented by the error bar. As a result, the selectivity of the IS-FETs is proved by these measurements. In this work, we successfully show the graphene based IS-FET can be a promising candidate as the nitrate sensor.

3.1.6 Conclusions

The nitrate selective membrane solution was prepared by mixing nitrate ionophore, PVC, plasticizer in the solvent. For the hybrid film, the synthesized solution was directly coated on the graphene surface. The sensor performance was demonstrated by measuring the shift of the Dirac point of graphene with different ion solutions. Dirac point of

graphene was located at -0.55 V after coating the selective membrane, and it was shifted about 0.25 V to the right from the original location as increasing concentration of the nitrate solution. The selectivity of the sensors is also confirmed with four different ionic solutions. The experimental result of the Dirac point shift can be explained by the potential change mechanism. Finally, we successfully show that the ion sensitive FETs with the hybrid film is a promising method to estimate the quantity of nitrate ions for drinking water.

3.2 Phosphate Detection

This paper reports ion sensitive field effect transistor with graphene/ionophore hybrid membrane for phosphate detection. CVD graphene is used as a sensing material because the electrical property of graphene can be easily changed by a surrounding condition. In the experiment, a shift of Dirac point is measured to check the concentration of the ions in the water. Since graphene does not have selectivity for the specific ions, phosphate selective membrane is used for the selectivity. The membrane is synthesized by a molecular imprinted polymer. To check the selectivity of the graphene sensor coated with the selective membrane, the IS-FET is tested with several solutions, which have different ions and concentrations. The sensor response is measured by a semiconductor analyzer. Four different ion solutions are used for the measurement (phosphate, sulfate, chloride, and nitrate). Each solution has four different concentrations (0, 0.1, 1 and 10 mg/L). The

Dirac point shift from -0.4 V to -0.2 V as increasing the concentration. The detection limit and response time are 0.26 mg/L and 10s, respectively.

3.2.1 Introduction

Phosphorus is one of the essential elements for the growth of plants. However, an excessive quantity of phosphorus in water can make eutrophication and decrease water quality. Phosphorus is very toxic and can be accumulated in a living organism. Since phosphate (PO_4^{3-}) is the derivative of phosphorus, the detection of phosphate is necessary for the quality of water. The maximum allowable concentration of phosphate to avoid accelerated eutrophication is about 0.35 mg/L [77]. Many researchers have studied the fabrication of the phosphate ion sensitive sensor to detect the phosphate ion in the water. The commercialized current phosphate detection method is a standard colorimetric method. However, this method still has some disadvantages [78]. It needs complicate processes such as filtration, calibration and several chemical reaction steps with many reagents before the measurement. Although the current standard methods have a detection limit below the level of the regulation limit, it still needs to be further developed to avoid the time consuming process. Therefore, the investigation of new devices is highly desirable to simplify the measurement.

After the discovery of graphene, various techniques related to graphene families such as graphene oxide and reduced graphene were also studied by many research groups because of the low price [79-81]. However, further technical investigation and applications of graphene have been intensively studied and enhanced with different

growth methods, transfer and cleaning processes [82-84]. The advancement in graphene technology makes it possible to apply in sophisticated devices including solar cells, organic lighting emitting diode and sensors [85-88]. Especially, many researchers who study sensors have focused on graphene due to the superior electrical or mechanical properties of graphene [89]. Graphene-based sensors usually use the conductivity of graphene or Dirac point of graphene [90,91]. The conductivity and Dirac point of graphene can be shifted by the amount of ions in the solution. An ion sensitive field effect transistor (IS-FET) is one of the graphene sensors. Therefore, graphene can be used as the sensing material to substitute the traditional colorimetric standard method because it has several merits such as low price, high sensitivity and selectivity.

To compete with the current standard colorimetric method as a good alternative, the minimum detection limit needs to be close to the current method. Also, the sensor should have good selectivity which means the sensor can detect phosphate in the water without interference from other ions. First of all, the phosphate selective membrane solution is synthesized and applied to the sensing area to detect phosphate in the water without interference from other ions. The polymer based phosphate selective membrane was synthesized by molecular imprinted technique [92]. The molecular imprinted polymer has cavities in the polymer matrix which have an affinity to a specifically chosen template ion [93]. In other words, the MIP, phosphate selective membrane, can only grab phosphate ions in the water. This means other ions such as nitrate, chloride and sulfate cannot penetrate the membrane and cannot give an effect on the graphene. To evaluate

the sensor performance, the semiconductor analyzer is used with several solutions that have different concentrations and different ions in the measurement. The selective membrane is as important as the sensor fabrication to successfully detect phosphate ions in the water. Therefore, we focus on the fabrication process of the sensor using the MEMs technique and the synthesis process of the phosphate selective membrane using molecular imprinting. Finally, we successfully show the ion selectivity and sensitivity of the IS-FET devices. The device fabrication process and the MIP solution synthesis process are well described in the experimental section. The device performance is also characterized in the results and discussion section.

3.2.2 Preparation of graphene based sensor

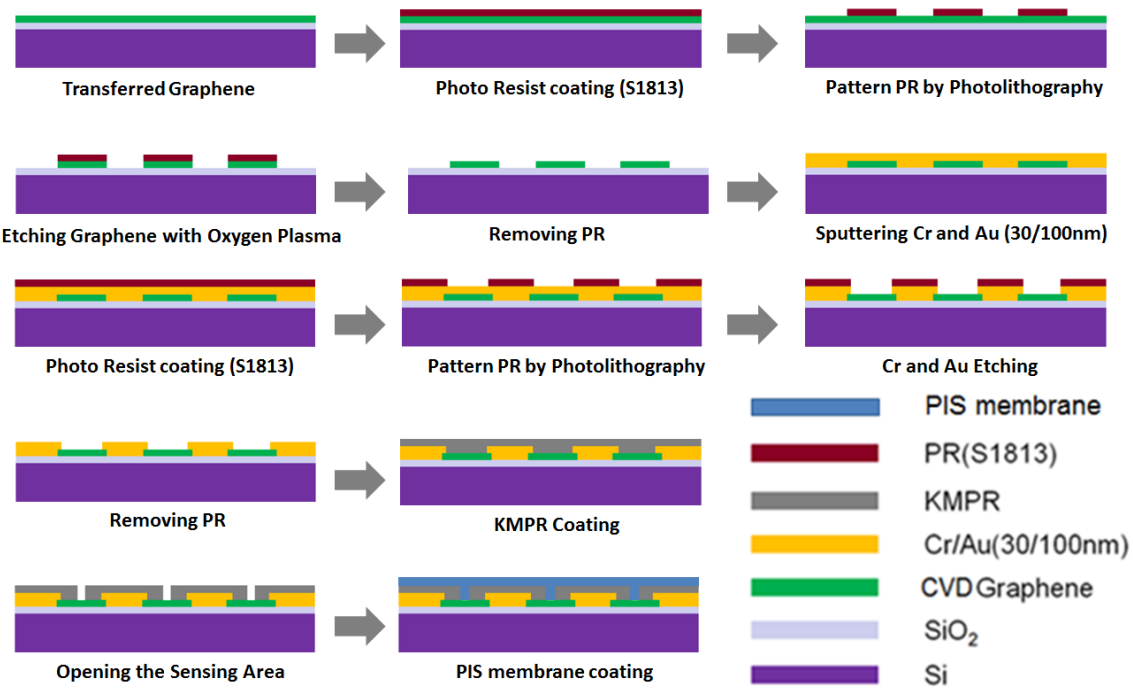

Figure 3.9. Fabrication flow chart of the graphene based phosphate sensor.

Figure 3.9 shows the flow chart for sensor fabrication. The first step is graphene growth. Graphene was synthesized by chemical vapor deposition (CVD) method. The synthesized graphene needs to be transferred to a target substrate with a thermal release tape method [94]. Traditionally, PMMA has been used in the transfer process, followed by acetone clearing because PMMA can support large size graphene and obtain continuous graphene coverage [95]. However, many research groups reported the disadvantage of PMMA [96]. Although the continuous graphene sheet can be obtained by using PMMA, it is difficult to remove the polymer residue and transfer the graphene to the target location in the sensing area. The sequence is as follows, first remove the protective film from the tape, and then put the adhesive part of the tape on the graphene sheet. The copper, catalyst substrate, is etched by a warm copper etchant (55~65 °C). The etching process takes 25 minutes for 25 μm. After etching the copper substrate, the film washes out several times with DI water to remove the chemicals. The adhesion between the target substrate and graphene is a critical factor in successful graphene transfer. The target substrate, SiO_2, was treated with oxygen plasma for 15 minutes to enhance the adhesion [97]. After the process, the tape on the substrate should be pressed softly to the substrate. To detach graphene from the tape, the substrate needs to be heated to about 100 °C. Although it is hard to obtain continuous graphene film with the thermal release tape method, this method can give fewer residues on the graphene sheet. After transferring graphene, the photoresist (S1813) was coated by a spin-coater. Next, the coated photoresist was patterned with UV photolithography. The graphene was etched by using

oxygen plasma etching on opened parts of the photoresist. After removing the remaining photoresist with acetone, Cr (30 nm) and Au (100 nm) were deposited by e-beam evaporation on the substrate to make Au electrodes. The deposited Au and Cr films were also patterned by the wet etching method, followed by coating and patterning photoresist. During the wet etching process, the etching time is very important to prevent over-etching. For the next layer, KMPR, a negative photoresist, was coated in the substrate, and then KMPR was patterned using photolithography. The last layer is the phosphate selective membrane. The synthesized membrane was coated by a spin-coater (2000 rpm for 1 min), and the O-ring was attached to define the sensing area.

3.2.3 Preparation of selective membrane

Figure 3.10 (a) shows the process of how to prepare the sensor with the phosphate selective membrane. The selective membrane is synthesized by a molecular imprinting technique, which makes cavities in the polymer like a stamping method [98,99]. Since the polymerization of monomers was involved with templates in the process, the monomer will have the affinity for original molecules after removing the templates. Therefore, the MIP membrane can be used for the selective membrane. The solution for the membrane was synthesized with cross-linking monomers (ethyleneglycoldimethacrylate (EGDMA) and polyurethane acylate (PUA)). The ratio of cross-linkers was 85:15 to provide increased mechanical stability and flexibility.

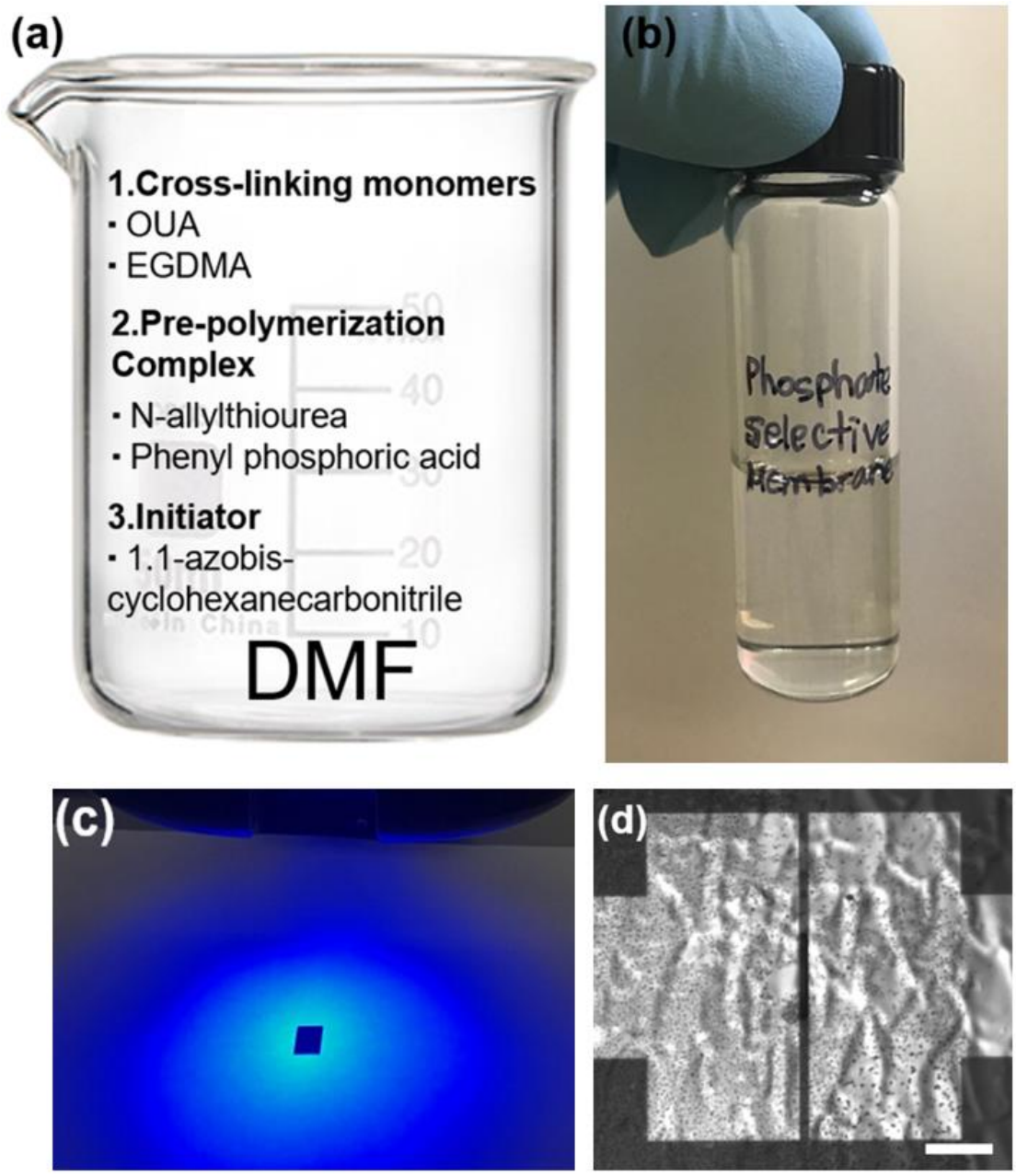

Figure 3.10 (a) Synthesize process of the selective membrane solution, (b) Synthesized selective membrane solution, (c) Polymerization process with UV light, and (d) Optical image for the sensing area after coating the solution. Scale bar is 10 μm.

Thiourea was used for the monomer, and the template was phenylphosphonic acid. Cross-linkers (EGDMA (4.0 g) and PUA (0.71 g)), thiourea (0.59 g) and phenylphosphonic acid (0.40 g) were mixed with DMF solvent (2.44 g). Next, the initiator 1,1-azobis-cyclohexanecarbonitrile (0.07 g) was added in the mixture. Figure 3.10 (b) shows the synthesized phosphate selective membrane solution that is transparent. The solution needs to be flushed with nitrogen gas to remove oxygen in the solution because the oxygen easily reacts with the free radicals and makes the solution polymerized. The synthesized solution was applied on the surface of the sensing area, and then the coated area was exposed to UV light (20 min) to polymerize the solution, as shown in figure 3.10 (c). Then, the polymerized membrane was rinsed with methanol to remove the phenylphosphonic acid templates from the thiourea monomer. After washing the device, the surface of the sensing area is characterized by an optical microscope. Figure 3.10 (d) is the optical image of the sensing area. The plasticized the solution shows the wrinkles on the surface. The membrane coated devices are tested with different ion solutions, and the results are demonstrated in the measurement section.

3.2.4 Sensing mechanism

The KMPR layer can prevent leakage current. The patterned KMPR has windows for graphene, which can make graphene expose to the solutions. Through this window, the graphene can communicate with the solutions.

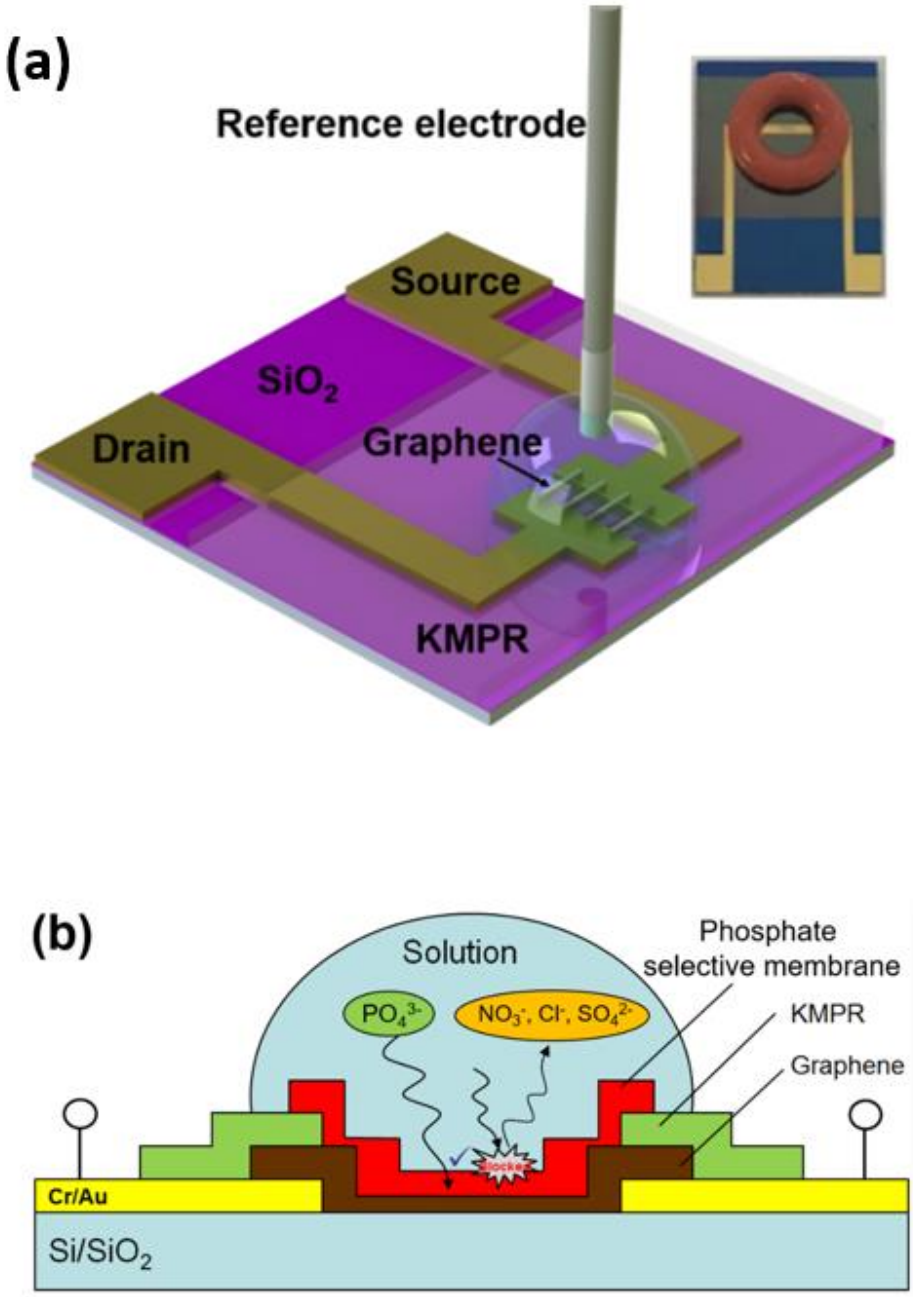

Figure 3.11 (a) Schematic diagram for the structure of IS-FET, (b) Schematic diagram for the mechanism of phosphate selective membrane.

For the last layer, the selective membrane was coated on the graphene. In the inset image in figure 3.11 (a), the final device has O-rings which can confine the ionic solutions. Figure 3.11 (b) shows the mechanism of phosphate selective membrane. The selective membrane blocks other ions such as nitrate, chloride and sulfate in the solution, but only phosphate ions can penetrate the phosphate selective membrane, as shown in figure 3.11 (b) [101]. In other words, the phosphate ion can only give the doping effect on graphene. Therefore, IS-FET can get the selectivity by coating the selective membrane. In this experiment, the ion solutions with different ions were applied to the sensor to verify whether IS-FET shows the selectivity or not. In the measurement, the fixed voltage (0.05 V) was applied between the source and drain electrodes (V_{DS}), while the reference voltage was swept from -1 V to 1 V. The transfer curve was obtained when the reference voltage was swept. The transfer curves were demonstrated in the next section.

3.2.5 Measurement of the devices with the phosphate selective membrane

Figure 3.12 (a) is the image of the fabricated sensor with 44 sensors on the Si/SiO_2 wafer. The KMPR was coated and patterned for the electrodes area and sensing area. The magnified inset image shows the sensing area. There is the KMPR window between the Au electrodes through which graphene can interact with the solution. The 10 graphene bridges are connecting two electrodes. The little dark parts in the bridges are the sensing areas that are the KMPR windows. The graphene can be exposed to the solution through these windows.

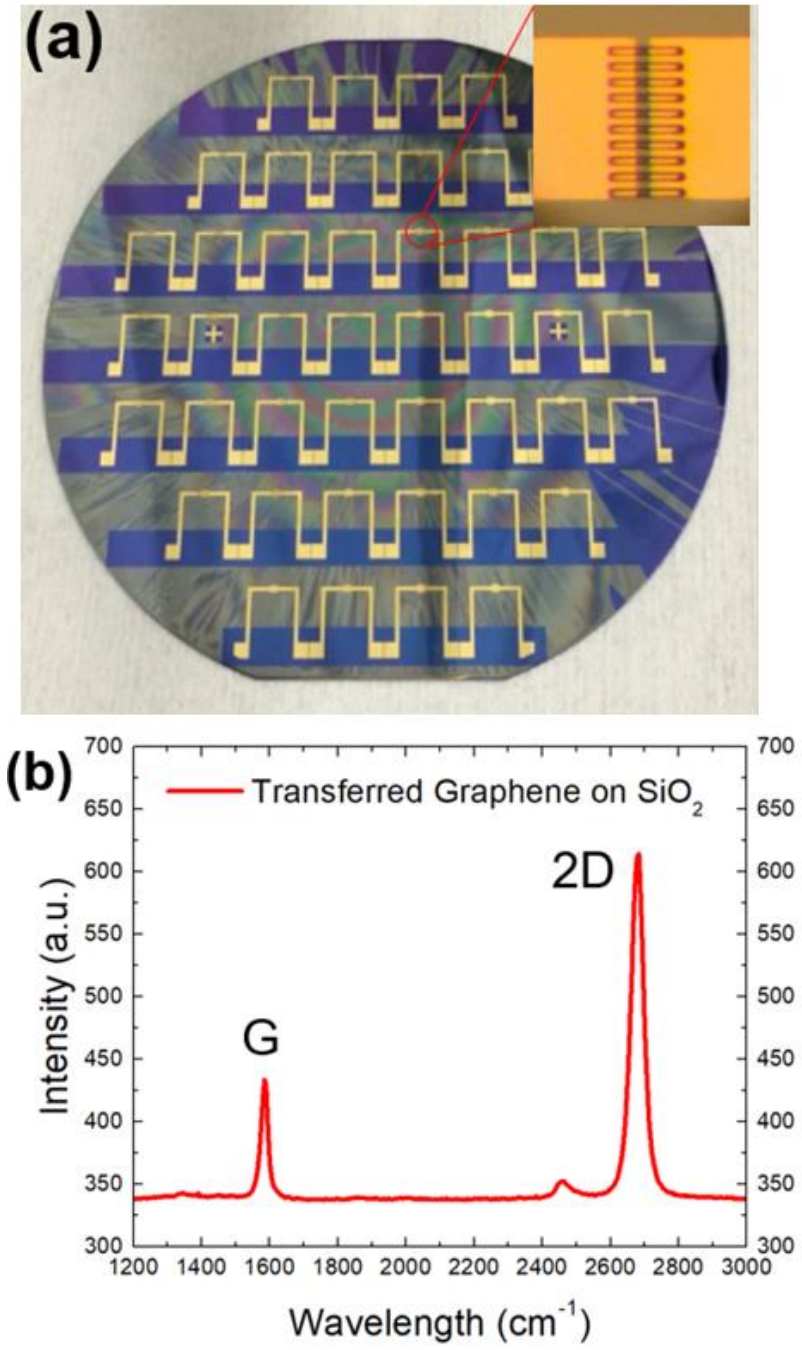

Figure 3.12 (a) Wafer image after finishing the KMPR patterning process, (b) Raman spectroscopy of graphene in the sensing region. Inset image shows the optical image of the sensing region.

Raman spectroscopy was used to confirm the graphene layers. Figure 3.12 (b) shows Raman spectroscopy of the transferred graphene on the Si/SiO_2 substrate. The Raman laser (532 nm) was focused on the graphene. The Raman spectroscopy shows the graphene bands (G band and 2D band) as well known in the previous study [102]. G band and 2D band are located in the 1530 cm^{-1} and 2700 cm^{-1}, respectively. The result demonstrates that the graphene sheet does not get damaged during the several photolithography processes. After finishing the fabrication process, the selective membrane is coated on the graphene to cover the sensing area.

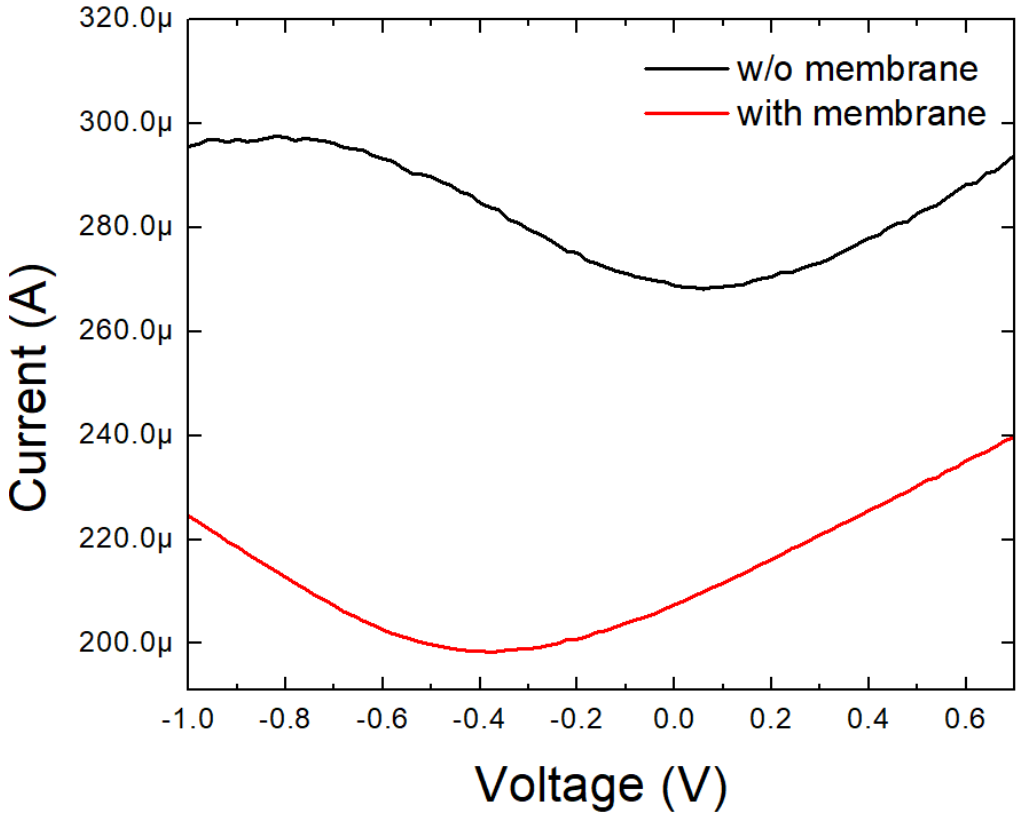

Figure 3.13 Transfer curve of IS-FET with membrane and without membrane.

The IS-FET sensors were characterized by a semiconductor analyzer because the doping type of graphene can be confirmed with the transfer curve [103]. First, IS-FETs are tested without the membrane to check the effect of the selective membrane. The sensor shows a P-type property before coating the membrane. The graphene sheet got some damages and polymer residues during the transfer process [104]. These damages make graphene P-type. In other words, holes are the main carriers in the graphene after finishing the fabrication process. Therefore, Dirac point of the graphene is located on the positive side. However, the property is changed to N-type after coating the membrane. After coating the membrane, the main carrier is changed from holes to electrons in the graphene surface. The electrons are affected by the ions in the solution. The reason why the main carriers change is the presence of a charged ion in the polymer matrix that can attract the electrons in the graphene [105]. Figure 3.13 depicts the transfer characteristic of the sensor with a selective membrane and without the membrane. In this figure, we confirm that the doping effects of graphene that come from the residue and the selective membrane. Dirac point is located on the positive side (0.1 V) before coating the membrane. However, it is shifted on the negative side (-0.4 V). And the overall current level is decreased due to the polymer membrane.

The membrane solution is coated by a spin-coater (3000 rpm for 30 s). After coating the membrane, the sensor is tested with phosphate solutions that have different concentrations. Also, the other solutions (chloride, nitrate and sulfate) are applied to the sensor to confirm the selectivity of the sensors.

The main carrier of graphene, electrons, will be decreased as increasing the phosphate ions in water. Because the phosphate ions make the electrons in graphene repel from the surface. This phenomenon causes the doping effect of graphene, making Dirac point shift to left or right. Therefore, the measurement of the Dirac point can be a great measurement method for detecting the amount of ions in water.

We applied the phosphate, chloride, nitrate, and sulfate solutions which have different concentrations (0, 0.1, 1 and 10 mg/L), and measure the responses of the FET devices to verify the function of the membrane. As increasing the concentration, the transfer curve shifts to the right side in both graphs. Without the selective membrane, the phosphate ions attract the holes in the graphene surface. After coating the membrane, the penetrated phosphate ions repel the electrons in the graphene surface. As a result, both transfer curves are shifted to the right side. The calculated detection limit is 0.26 mg/L, and the response time is about 10 seconds. Each ion solution has four different concentrations (0 ~ 10 mg/L). Figure 3.14 (a) shows the sensor response with chloride ion solution. As increasing the concentration, the Dirac point very slightly moves to left. However, the movement can be neglected. In figure 3.14 (b), the nitrate solutions were applied to the sensor. The nitrate solution could not make the Dirac point move as well. As shown in Figure 3.14 (c), we can also confirm that sulfate ion cannot affect the sensor. Figure 3.14 (d) shows the response sensor with phosphate ion solutions. In contrast with other solutions, the Dirac point was shifted from left to right, as increasing the concentration.

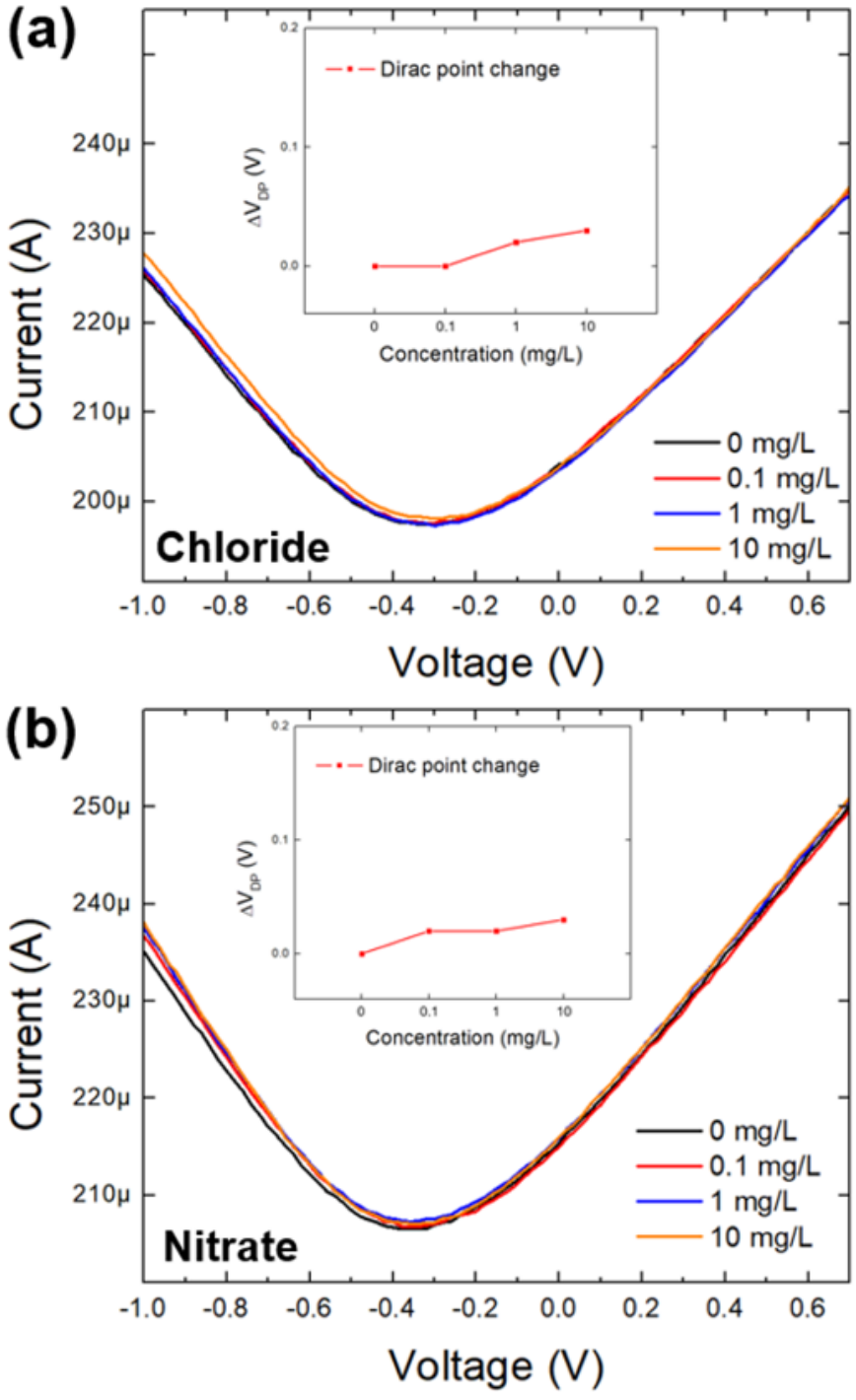
(a)
Current (A)
240µ
230µ
220µ
210µ
200µ
Chloride
0 mg/L
0.1 mg/L
1 mg/L
10 mg/L
-1.0 -0.8 -0.6 -0.4 -0.2 0.0 0.2 0.4 0.6
Voltage (V)
Dirac point change
ΔV_DP (V)
0.2
0.1
0.0
0 0.1 1 10
Concentration (mg/L)
(b)
Current (A)
250µ
240µ
230µ
220µ
210µ
Nitrate
0 mg/L
0.1 mg/L
1 mg/L
10 mg/L
-1.0 -0.8 -0.6 -0.4 -0.2 0.0 0.2 0.4 0.6
Voltage (V)
Dirac point change
ΔV_DP (V)
0.2
0.1
0.0
0 0.1 1 10
Concentration (mg/L)

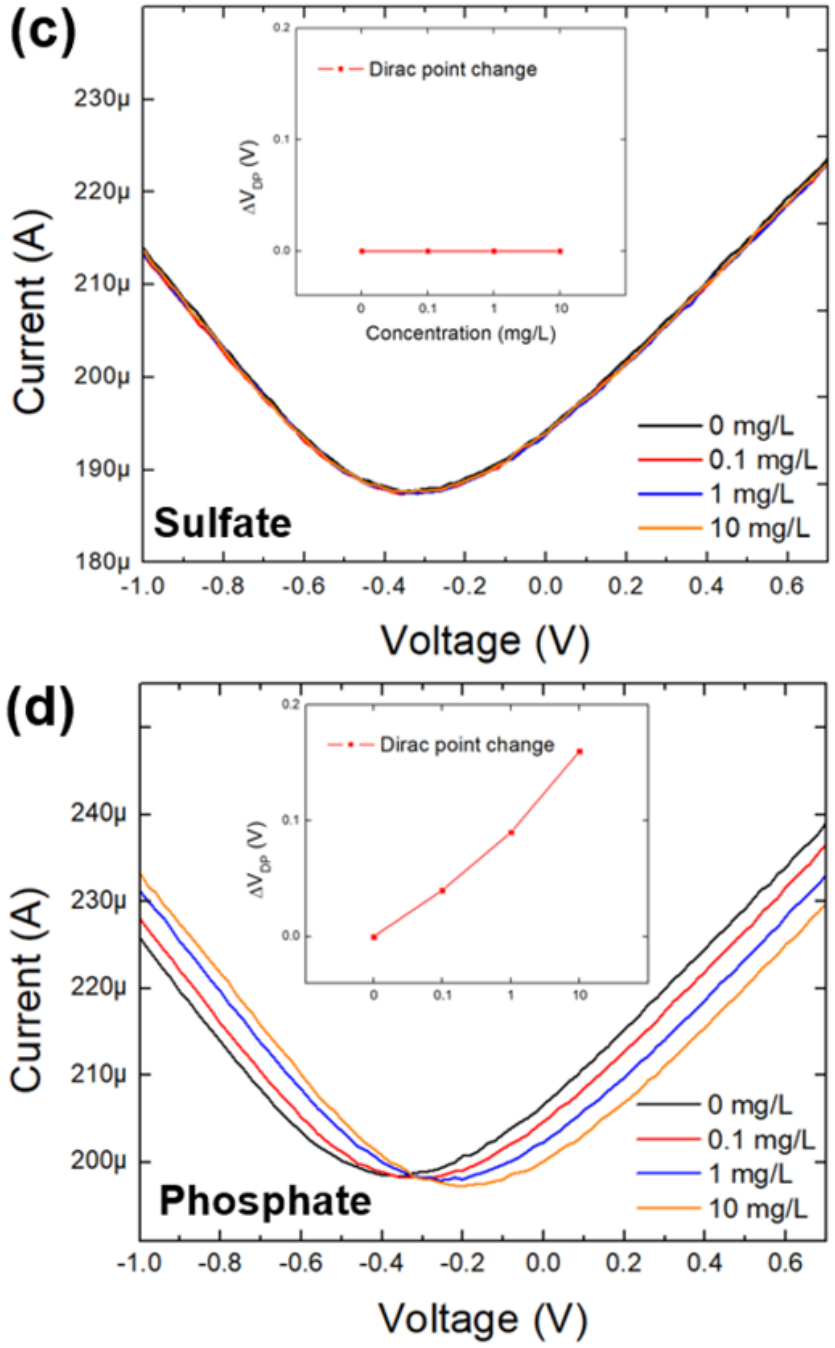

Figure 3.14 Transfer curves of graphene IS-FET with phosphate selective membrane. Four different solutions were applied to the sensor. Each graph shows the sensor response with (a) Chloride, (b) Nitrate, (c) Sulfate, and (d) Phosphate solutions.

Selectivity is the key factor in sensor performance. Although the graphene sensor has high sensitivity with various ions in the solution, it does not have selectivity by itself. The synthesized phosphate selective membrane was applied to the sensor to give the sensor the selectivity. In other words, the devices can detect the phosphate without interference with other ions in the water, when the selective membrane is coated on graphene.

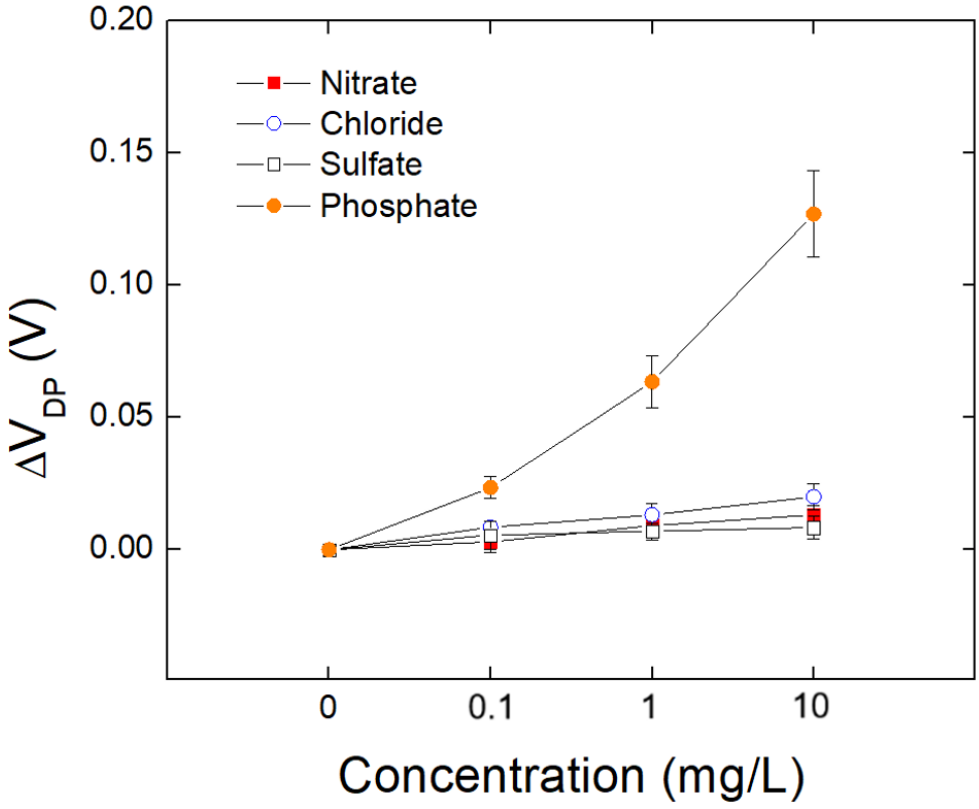

Figure 3.15 Selectivity of the phosphate selective membrane.

The sensor deposited with the selective membrane was characterized to check the interference. In figure 3.15, the responses of the sensor were compared after applying various solutions with different ions and concentrations. The reference voltage at Dirac point was measured as increasing the concentration. The result shows that the sensor only responded with phosphate solutions. The Dirac points are shifted from -0.4 V to -0.2 V with phosphate solutions. However, the sensor does not show a response with other solutions such as chloride, sulfate, and nitrate. As a result, we successfully confirm that the FET sensor has selectivity for phosphate solutions with the synthesized selective membrane. The results show that IS-FET can be a promising candidate to substitute the current colorimetric method.

3.2.6 Conclusion

The synthesized phosphate selective membrane was coated on the sensing area, and the sensors were characterized by the semiconductor analyzer. Since Dirac point of graphene shifts to the left or right side when it is affected by the doping effect, the sensor performance with the selective membrane was confirmed by measuring the shift of Dirac point of graphene with different ion solutions. We successfully synthesized the phosphate selective membrane and deposited the selective membrane to the sensor. Finally, the performance and selectivity of the IS-FET devices were successfully demonstrated. The Dirac point shifts from -0.4 V to -0.2 V without the interference of other ions.

3.3 Chloride Detection

The objective of this research is developing graphene based chloride sensitive field effect transistor (IS-FET) including chloride selective membrane. This report includes the preparation method of polyvinyl chloride based the selective membrane. Also, we tested the sensitivity and the selectivity of the sensors with several ionic solutions that have different concentrations. The sensor response is characterized by the semiconductor analyzer and the sensitivity was defined by the Dirac point shift. The sensors are exposed to four ionic solutions including nitrate, phosphate, sulfate and chloride for the selectivity test. The results show that the sensor can be applied to the water monitoring system.

3.3.1 Introduction

In the human body, the body fluid contains a lot of chloride ions that contribute to the metabolism of the cells. So maintaining the balance of chloride is very important for health. When we drink water that has chloride, most of the chloride is absorbed in our body. If a person daily consumes 2 liters of water that has 10 mg/L of chloride, the person would be exposed to 20 mg per day. A normal adult has about 81.7 g chloride in their body and usually lose 530 mg chloride per day. Therefore, it is recommended to take 9mg per kg of body weight. However, an excessive amount of chloride can cause health problems in the human body. The increased chloride level in the body causes dehydration and results in hyperchloremia [106]. Therefore, it is necessary to monitor the amount of chloride in drinking water.

The traditional detection methods of chloride use silver nitrate for the titration. As a result, the white silver chloride is precipitated under the solution. The concentration of chloride can be assumed by the precipitated silver chloride. The titration method is a time consuming process and it is difficult to know the endpoint of the reaction. Another approach is a chloride selective electrode that has tridodecylmethylammonium chloride ion-exchanger in poly(n-butyl acrylate)membrane. Although the selective electrode method uses a small amount of plasticizer that can contaminate the samples, it also has the interference with other ions or pH [107].

To solve the problems, we suggest the graphene based IS-FET with the chloride selective membrane. The proposed structure consists of graphene that can enhance the sensitivity of the sensors and polymer based selective membrane that makes the sensor selective [108]. Since Dirac point of graphene can be sensitively shifted by surrounding charges, chemical vapor deposition (CVD) graphene is selected for the sensing material and chloride ionophore is added to the membrane for the selectivity. The sensor test with four different concentrations (0.1, 1, 10, 100 mg/L) and with four different solutions (nitrate, phosphate, sulfate and chloride). Finally, we successfully demonstrate the sensor responses about sensitivity and selectivity.

3.3.2 Synthesis of selective membrane and coating the membrane on the sensor

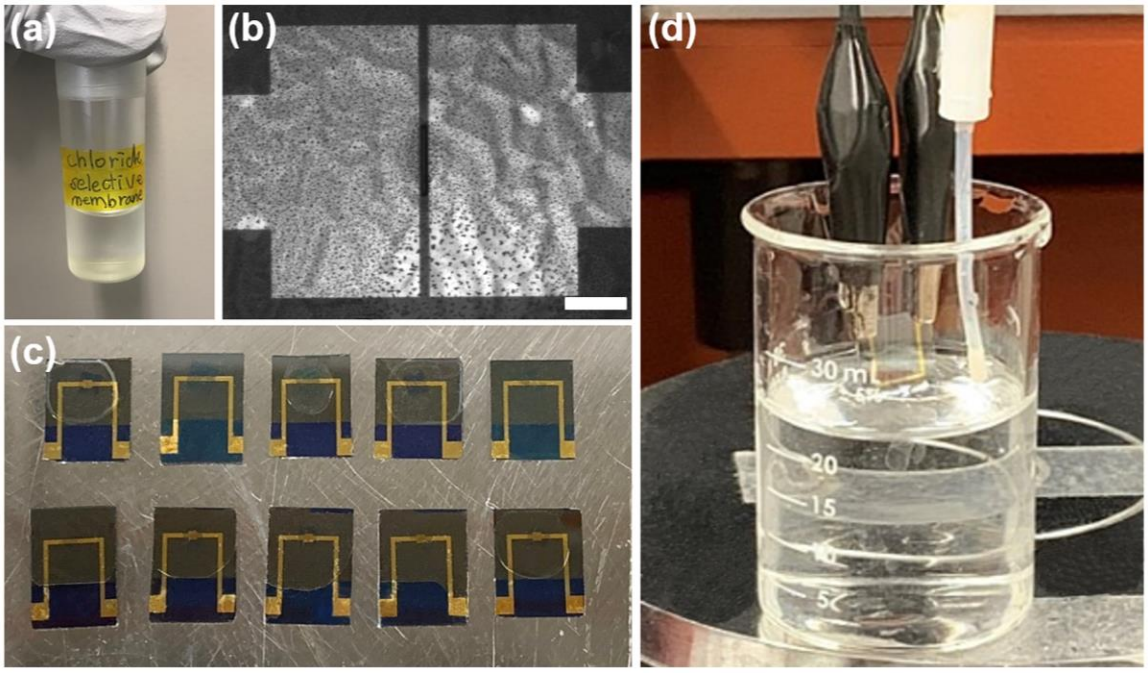

Figure 3.16 (a) Synthesized solution for the chloride selective membrane (b) Optical image of the sensing area after coating the solution (scale bar = 10 μm) (c) Prepared chloride sensors (d) Dirac point measurement system.

Figure 3.16 (a) shows the synthesized chloride selective membrane solution. For the chloride selective membrane, the first solution was prepared by dissolving the chloride ionophore (0.05 g) in dibutyl phthalate (0.15 g). An amount of about 0.002 g of 1-(2-Nitrophenoxy)octane (NPOE) as a plasticizer was added to the prepared solution. As another part of a synthesis, the PVC solution was obtained by dissolving the PVC (0.15 g) into tetrahydrofuran (6 ml). Finally, two prepared solutions need to be gently mixed.

The obtained solution coated on the graphene based devices using spin-coater to form the chloride selective membrane. Figure 3.16 (b) is the optical image after applying the solution to the sensing area. Since the solvent in the solution was evaporated during the coating process, the coated film has the wave structure. Figure 3.16 (c) shows the sensors after the coating process. The solution covers most of the sensing part and Au electrodes. Figure 3.16 (d) depicts the measurement system. Two clamps are connected to each of the Au electrodes (source and drain) and the Ag/AgCl electrode (gate) is immersed in the solution. The V_{DS} is fixed as 0.05 V and the V_G is swept from -1 V to 1 V.

3.3.3 Sensor response with the chloride selective membranes

The chloride sensors were characterized by using a semiconductor analyzer. The sensors need time for the stabilization of the signal. The current level of the device was shifted, but it was stabilized after 15 minutes. Figure 3.17 (a) shows the sensor performance with several solutions that have different concentrations. The black curve shows the response with DI water and the other curves demonstrate the response with other solutions. As increasing the concentration, Dirac points of the curves were shifted to the right side. In other words, the graphene shows p-doping property due to the chloride ions in water. To make it clear, the percentage of Dirac point change was calculated and was shown in figure 3.17 (b). The percentage of Dirac point change was about 25 % in the 100 mg/L chloride solution. The overall results show that Dirac point linearly shifts to the right side when the concentration of solutions logarithmically increases.

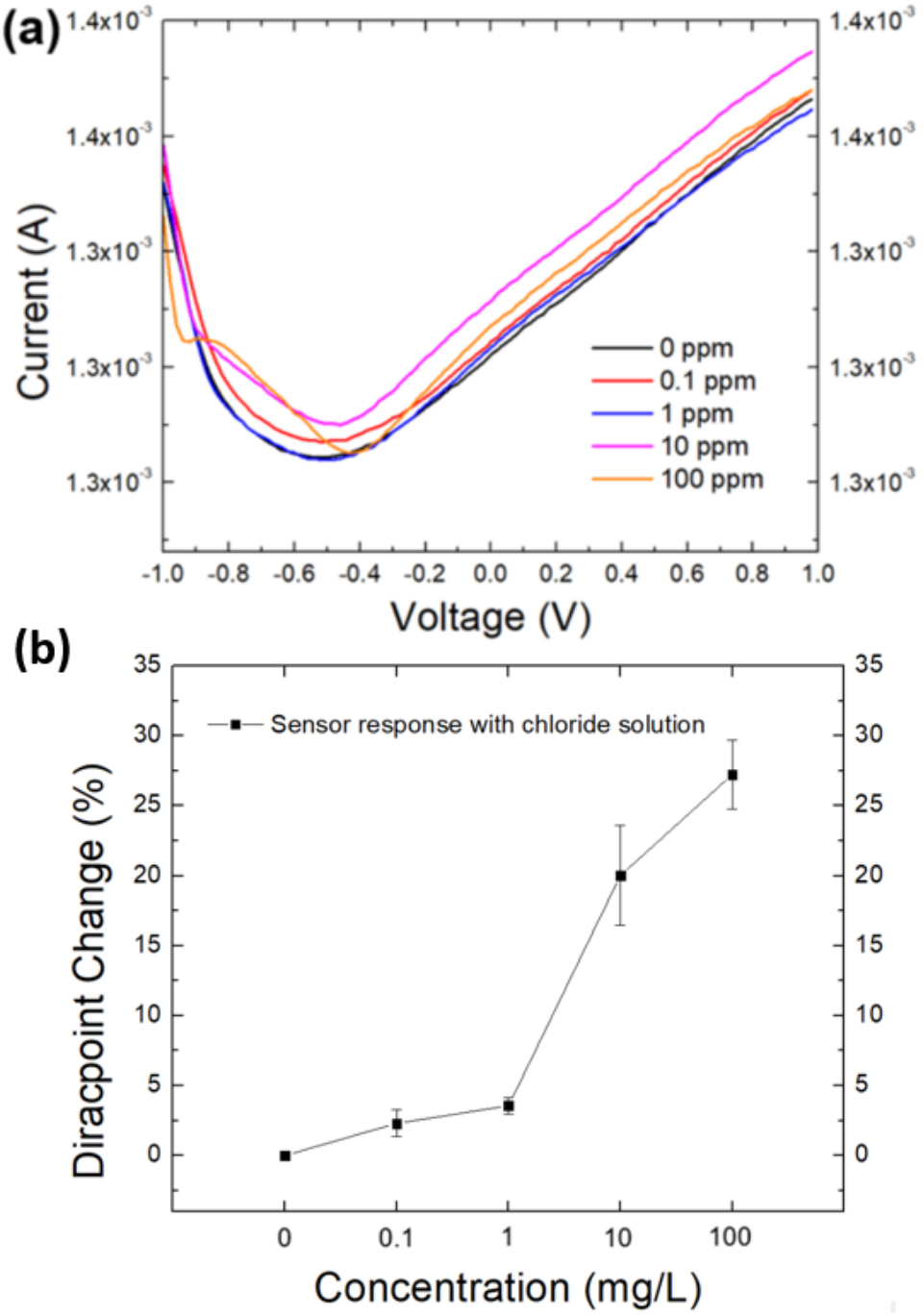

Figure 3.17 (a) Transfer curves of IS-FET with chloride solutions that have different concentrations. (b) Dirac point change curve depending on the concentration of chloride solution.

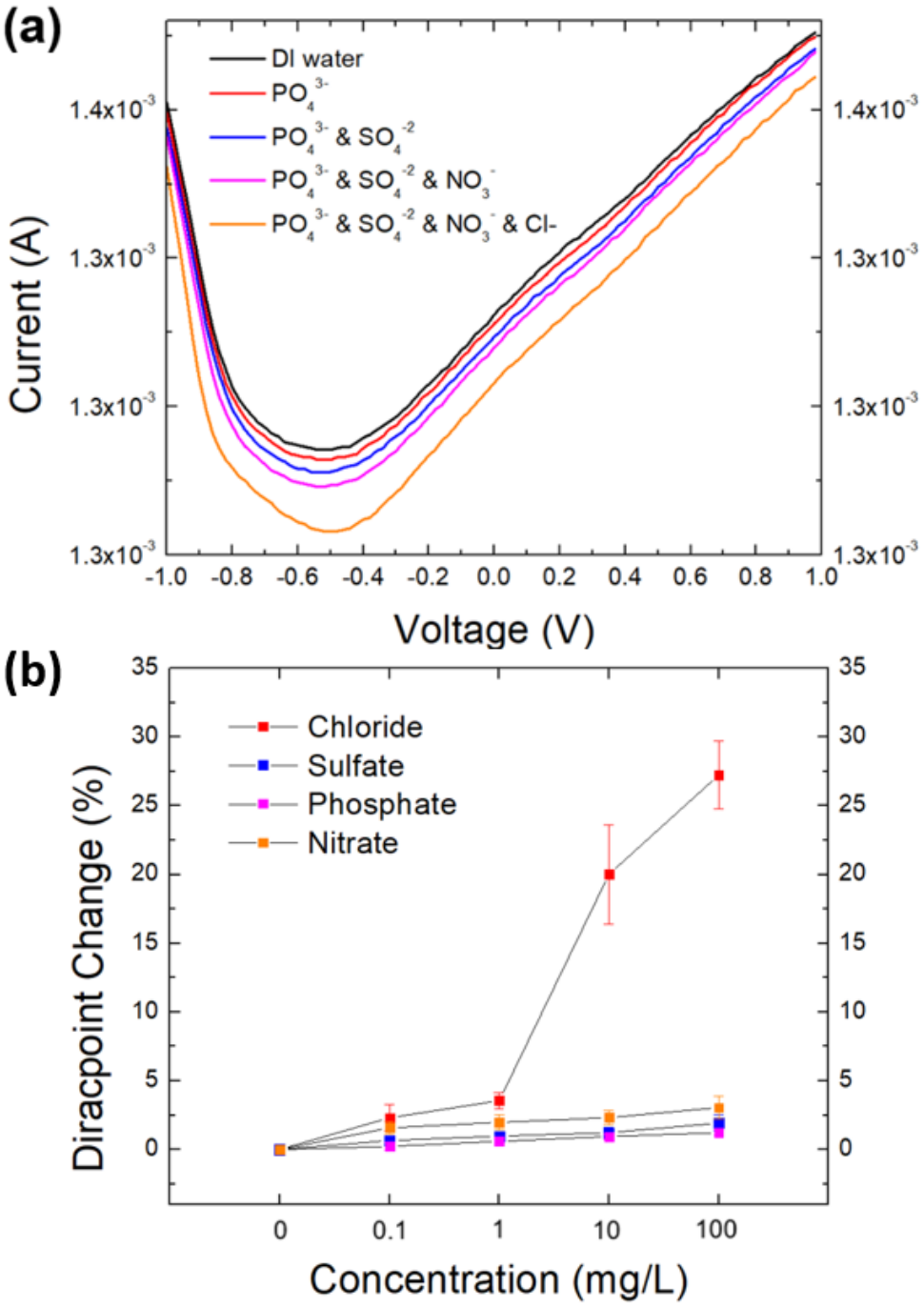

Figure 3.18 (a) Selectivity test of chloride sensitive IS-FET with different ion solutions (b) Dirac point change curves of the chloride sensor depending on the solutions.

The low detection limit of the sensor is 10 mg/L and the selectivity performance is tested with four different solutions (nitrate, phosphate, sulfate and chloride). Each solution has different concentrations (0.1, 1, 10, 10 mg/L). Figure 3.18 (a) shows the sensor response with different solutions. First of all, the black curve is the response with DI water and the red curve shows the response with phosphate (0.1 mg/L) in DI water. Sulfate (0.1 mg/L) was added to the phosphate solution. Dirac point shift is detected when chloride is added to the solution that already has other ions. This means that the graphene based IS-FET only responds to a chloride solution. Figure 3.18 (b) is the Dirac point change curve depending on the concentration. In other words, this graph shows the amount of Dirac point change. The error bars were from the overall data that shows the change of Dirac point. When the sensors were exposed to the nitrate, phosphate and sulfate solution, Dirac point was shifted only a few percentages. However, the sensor clearly shows the shift of Dirac point with chloride solution. The maximum shift is about 25 % with 100 mg/L. The calculated detection limit is 0.87 mg/L.

3.3.4 Conclusion

The synthesized chloride selective membrane was applied to IS-FET for chloride detection. The selective membrane solution coated on the sensing area using spin-coater. We also prepared several solutions (nitrate, phosphate, sulfate and chloride) that have different ions and concentrations to demonstrate the sensitivity and selectivity of the sensors. In terms of the selectivity test, Dirac point was linearly shifted depending on the

concentration that is logarithmically changed. The selectivity of the sensors is also characterized by different ionic solutions. The sensor shows only a small response (about 2~5 %) with nitrate, phosphate and sulfate. However, the amount of change of Dirac point is about 25 % when 100 mg/L chloride solution was applied to the sensor.

3.4 Mercury Detection

This research aims to develop graphene based mercury sensitive field effect transistor (IS-FET). In the report, we explain the process of the fabrication of IS-FET and how to synthesize polyvinyl chloride (PVC) based on the mercury selective membrane. The sensor performance is measured by a semiconductor analyzer and the sensitivity is shown by the Dirac point shift. The detailed mechanism is also covered in the discussion part. The results show that the sensor can be a great candidate for the water monitoring system.

3.4.1 Introduction

Mercury is an extremely toxic material and can cause several problems for humans and the environment. The reason for the problem is that mercury can be accumulated in the ecosystem [109]. In the food chain, the higher positioned consumers have more mercury ion in their bodies because of the accumulation. Hence, mercury ion can cause health problems in the human body such as DNA, liver, kidney, lung, immune system and neurological system [110]. Finally, it can even lead to death. Therefore, it is very important to measure the quantity of mercury ion in drinking water.

Until now, many research groups have reported the method of how to detect the toxic ion in water including chromatography, fluorescence spectrometry, thermal decomposition and inductively coupled plasma methods [111-114]. Although that equipment can detect the low level of mercury ions in water, it needs a time consuming and complex process for the sampling and bulky equipment for the measurement. For these reasons, it is not a proper method for the online water monitoring system.

Here, we suggest the graphene based IS-FET for the mercury ion detection in drinking water. Since graphene sensitively responds to the surroundings, it is used for the sensing material. The Mercury selective membrane is applied to the graphene for the selectivity. In this work, we report the synthesis method of the selective membrane and sensor performance.

3.4.2 Synthesis of selective membrane and coating the membrane on the sensor

Figure 3.19 (a) demonstrates the fabricated devices on a SiO_2/Si substrate. The Au electrodes are patterned by the photolithography process and the synthesized graphene is transferred to the sensing area. KMPR is covered and patterned by photolithography to make a window that graphene can communicate through. The mercury selective membrane consists of mercury ionophore, polyvinyl chloride (PVC), 1-(2-Nitrophenoxy)octane in tetrahydrofuran. Figure 3.19 (b) shows the chemicals for the selective membrane. First, the PVC powder (0.15 g) is dissolved in THF (6 ml). Then the ionophore (0.05 g) is added to the prepared PVC solution.

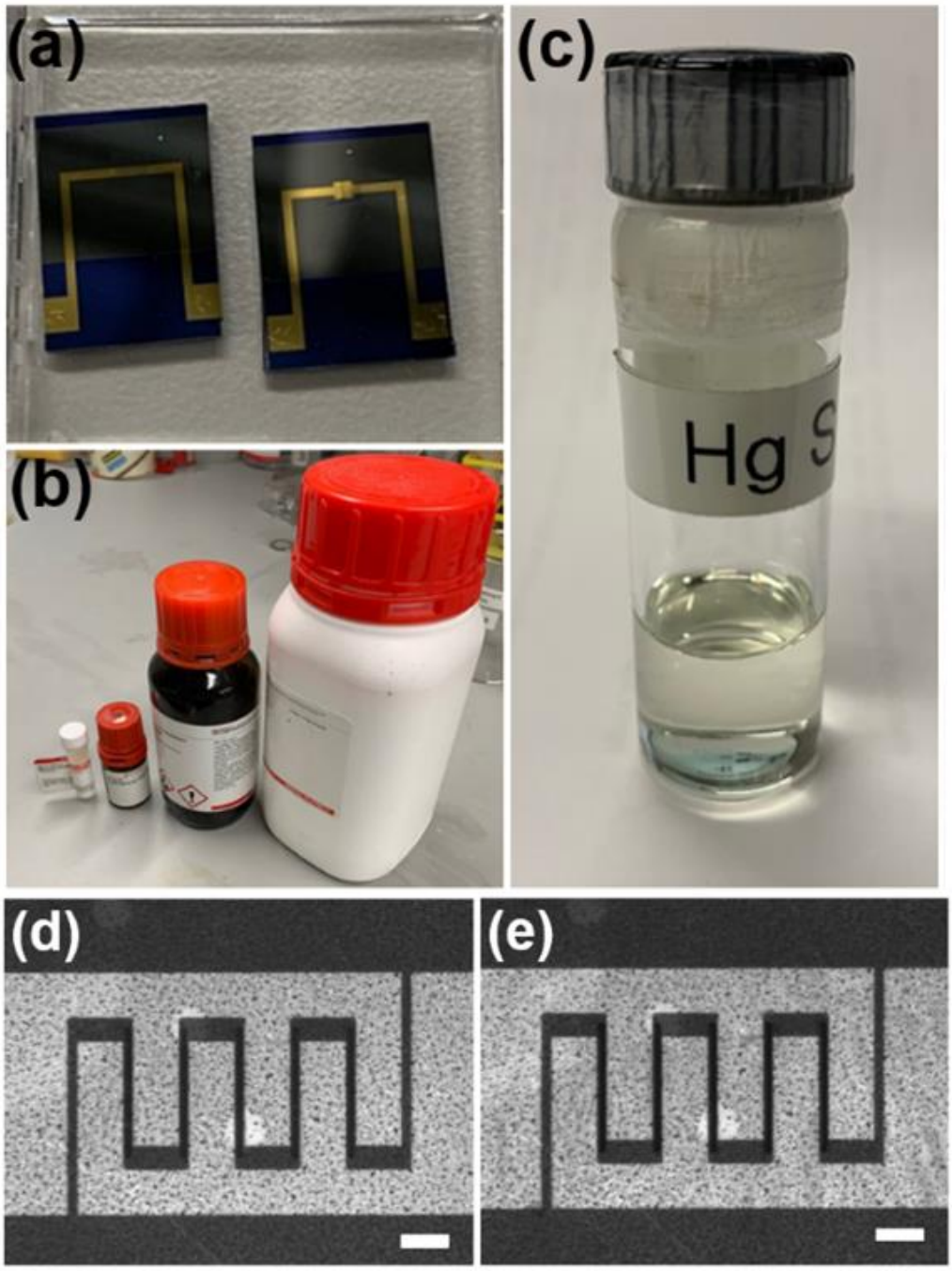

Figure 3.19 (a) Prepared devices (b) Materials for mercury selective membrane (c) Synthesized mercury selective membrane solution. Optical image of the sensing area (d) before and (e) after coating the solution (scale bar = 10 μm).

The final solution can be obtained by adding NPOE (0.002 g) which is a plasticizer in the solution. Figure 3.19 (c) is the prepared solution for the mercury selective membrane. The next step is the deposition of the solution to the substrate. For the deposition, we used a spin-coater (6000 rpm for 1 min). Figure 3.19 (d) and (e) are the optical images of the sensing areas before and after coating the mercury selective membrane, respectively. The scale bar is 10 μm. For the measurement, two electrodes are wired to the semiconductor analyzer and the sensing area is dipped into the solution. Ag/AgCl reference electrode also connects to the equipment and the tip part of the electrode is also exposed to the solution. The voltage between drain and source (V_{DS}) is fixed (0.05 V) and we swipe the reference voltage (V_G) from -1 V to 1 V.

3.4.3 Sensor response with the mercury selective membranes

The property of the device is characterized before coating the selective membrane and after coating the selective membrane. In figure 3.20 (a), Dirac point of graphene is observed on the right side of the origin of the graph, before applying the membrane. This means the graphene is p doped before coating the membrane. However, Dirac point is shifted to the left side from the origin of the graph. It is shown in figure 3.20 (b). This shows the graphene is now n doped by the selective membrane. Here we can expect the mechanism of the device with those phenomena. First, the doping type of graphene is changed by the selective membrane. This shows that the membrane includes the negatively charged components which can trap the main carriers of graphene.

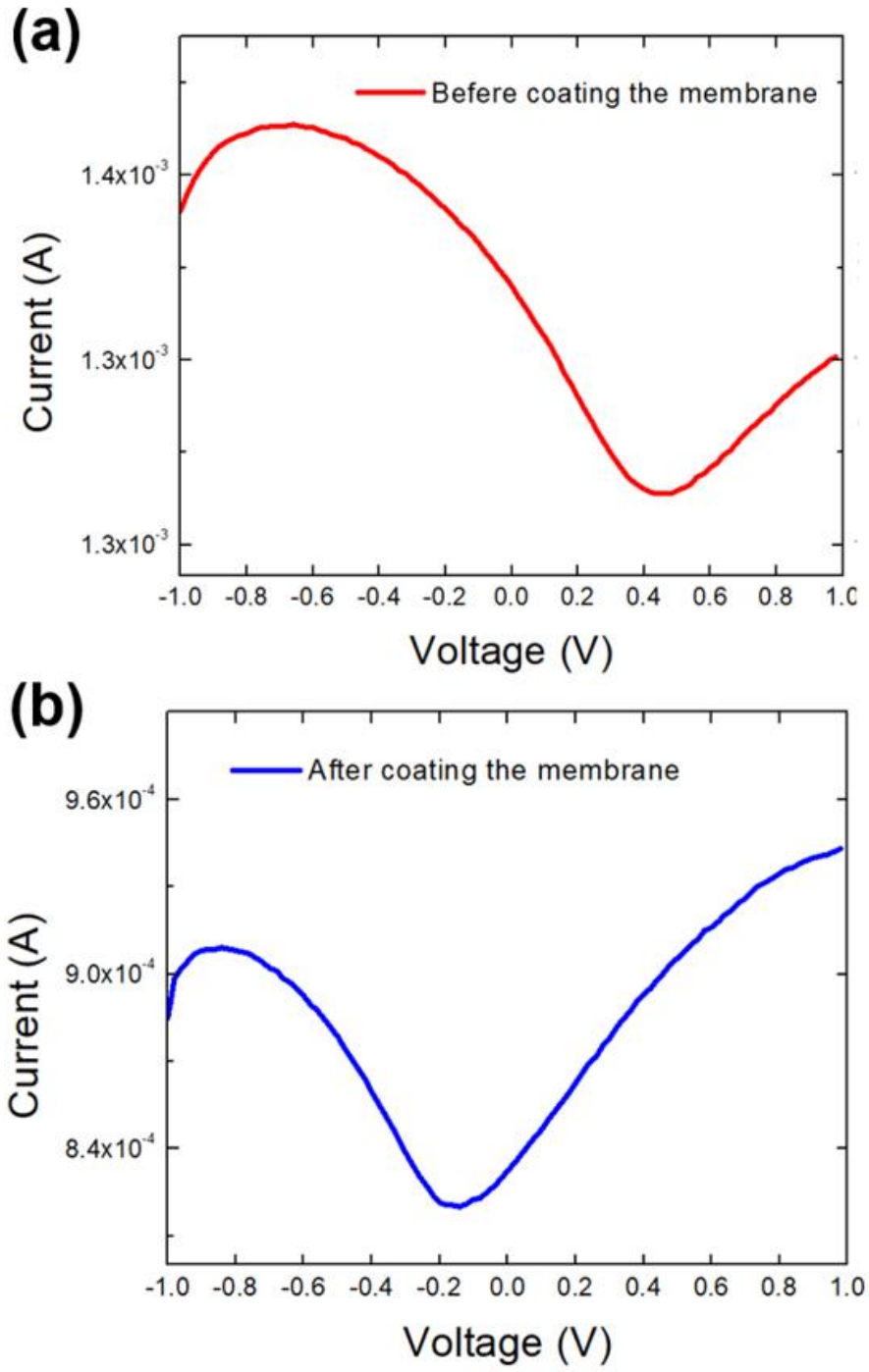

Figure 3.20 Transfer curves of IS-FET (a) before and (b) after coating mercury selective membrane. Dirac point is shifted to the left side after coating the membrane.

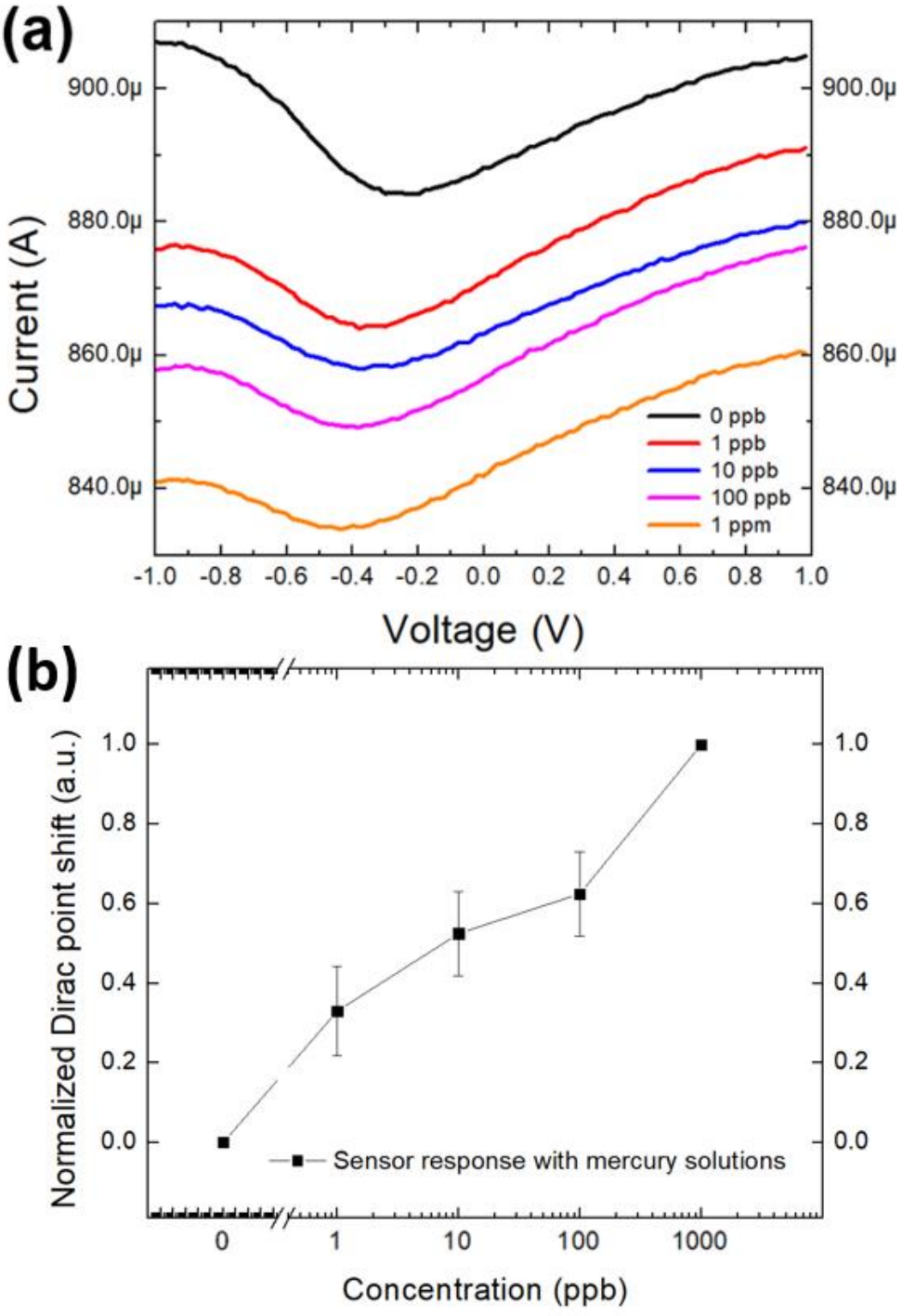

Figure 3.21 (a) Transfer curves of IS-FET depending on the concentration of mercury solution (b) Dirac point movements as increasing the concentration.

This gives an effect on the doping of graphene and shifts Dirac point of graphene. The detailed working principle can also be explained by using the phenomena.

The shift of Dirac point is demonstrated with the solutions which have a different concentration (1, 10, 100, 1000 ppb). Figure 3.21 (a) shows the transfer curves of IS-FET depending on the mercury concentration. The black curve is the response to DI water. The location of Dirac point is almost the same as the curve in figure 3.21 (b). As increasing the concentration of mercury, Dirac point of graphene shifts to the left side from the black curve. It shows that graphene is n doped by the mercury ion in the solution. When the mercury ion in water is attracted by ionophore in the membrane, the selective membrane shows the positive charge which can dispel the hole carriers in graphene. As a result, graphene shows the n doped effect. Figure 3.21 (b) depicts the Dirac point movement depending on the concentration. In the graph, Dirac point is linearly changed to the left side as increasing the mercury concentration that is logarithmically changed. The movement of Dirac point is normalized to make it easy to compare the results.

3.4.4 Conclusion

The synthesized mercury selective membrane was coated on the sensing area of IS-FET using spin-coater. For the performance test of the sensor, we measure the Dirac point shift by semiconductor analyzer. Dirac point was linearly shifted to the left side as

increasing the concentration that is logarithmically changed. The device shows the response in the low concentrated mercury solution (1.125 ppb) in a minute.

CHAPTER 4

GRAPHENE BASED SENSORS USING ANODIC ALUMINUM OXIDE

4.1 Graphene Based Ion Sensitive-FET Sensor with Porous Anodic Aluminum Oxide Substrate for Nitrate Detection

In this paper, we report an ion sensitive field effect transistor sensor on anodic aluminum oxide (AAO) substrate, which can directly detect nitrate in water without a buffer solution. The free-standing AAO substrate has a highly ordered porous structure, which supports graphene and Au electrodes. The AAO substrate increases the exposed area of graphene in water. We describe the surface structure of the AAO substrate with scanning electron microscopy in each fabrication process. The device structure and mechanism are also explained in the paper. Graphene is used for the sensing material for its sensitivity in response to the surroundings. The nitrate selective membrane is synthesized and applied to the surface of graphene. The performance of the IS-FET sensors is characterized by a semiconductor analyzer. In the results, the performance of the device is significantly enhanced due to the porous structures of AAO. We successfully demonstrate the superior sensitivity and selectivity of the sensors. The detection limit is 0.32 ppm, and the response time is less than 3 seconds.

4.1.1 Introduction

Ammonium nitrate is one of the major components in fertilizer [115]. Nitrate can be used to improve the nitrogen content in the soil. Since excessive nitrate can dissolve into the surface water, an increment of the amount of nitrate in the soil causes water pollution. Cattle urine is another nitrate source [116]. Subsequently, the amount of nitrate in water is extremely high near livestock farms and plantations. Near those places, humans and other forms of life can be exposed to water that has highly concentrated nitrate. When people are exposed to an excessive amount of nitrate, it can cause health problems such as blue baby syndrome. The name of this disease comes from the color of the baby due to the lack of oxygen in the body as a result of nitrate poisoning [117]. Excessive nitrate can also cause eutrophication in water which can prevent oxygen absorption from the surface of the water. As a result, high rates of fish mortalities are observed in bodies of water polluted with nitrate [118]. Therefore, measurement of the nitrate level in water is the first step to protect our environment.

Colorimetric detection is one of the common techniques for water quality analysis, which determines the concentration of a target chemical element [119]. The detection range of nitrate is from 1 to 15 ppm with a sensitivity of 1 ppm. Although it is useful where rough estimation is acceptable and direct monitoring is not necessary, it requires several time-consuming steps to prepare the samples. Another current approach for water quality analysis uses an ion selective electrode (ISE), which can convert the ion activity in the water into electrical signals [120]. The ISE requires multiple types of membranes for

different target ions. The type of membranes includes a compound electrode, solid state, liquid based and glass. Although the ISE is more selective than the colorimetric method, the sensor probe is very fragile and difficult to handle. For this reason, the ISE requires high maintenance costs.

To solve the problems in current technologies, our group has been working on developing graphene-based devices which have a detection limit of 0.82 mg/L. Although this device has a relatively low detection limit, it still needs to be improved. Here, we propose to use anodic aluminum oxide (AAO) as a substrate to enhance the performance of the device. Porous AAO structure is fabricated by a well-known process called electrochemical oxidation of aluminum. The AAO fabrication technique has been studied by a lot of research groups and companies because of its well-ordered nanoporous structure and low-cost production. In the research, the relationship between AAO and experimental parameters has focused on the production of high quality porous nanostructures. In particular, the nanostructure is closely related to the electrolyte and the applied voltage. After two step anodizing method was invented, this method is still widely used [121]. This kind of small patterned structure can be widely applied to various applications such as filters, sensors, photonic and electronic devices [122-125]. Another application that uses the AAO nanostructure as a substrate in the IS-FET to enhance performance. Although several research groups have studied the topic, no one has used the hybrid film of graphene and nitrate selective membrane to the IS-FET for nitrate detection yet. Regarding the hybrid membrane, each layer has a different function. Graphene is used as

the sensing material, and the nitrate selective membrane includes a nitrate ionophore that is used for the selectivity of the sensor. Furthermore, we use the AAO substrate to enhance the sensor performance in this work. Dirac point change shows the change of the charge carrier density in graphene, and the concentration of solution changes the charge carrier density of graphene. Therefore, the Dirac point shift indicates that the charge carrier density is changed by ions in the solution. For these reasons, the concentration of the target ions can be detected by measuring the Dirac point shift. Besides, the porous structure of the AAO substrate can enhance the sensing performance by increasing the exposed area of graphene to nitrate and decreasing the noise level of the device.

4.1.2 Experimental method

Al plates (Zhong Nuo, YJ13G04) used for the anodization has 5N (99.999 %) purity and thickness (0.3 mm). We cut the Al plate (3cm x 4 cm) and clean surface impurities with three solutions. The first solution is Trichloroethylene (TCE) which can remove the organic materials on the surface. The second and third solutions are acetone and methanol, respectively. In each step, sonification (for 15 min) helps the cleaning process. After the cleaning process, the Al substrates were polished electrically to make the surface smooth. For the electropolishing process, we applied 20 V to the Al plate in the anode and graphite in the cathode for 4 min. A mixed solution of ethanol and perchloric acid (3:1) is used for the polishing process which is very important for the next anodizing process.

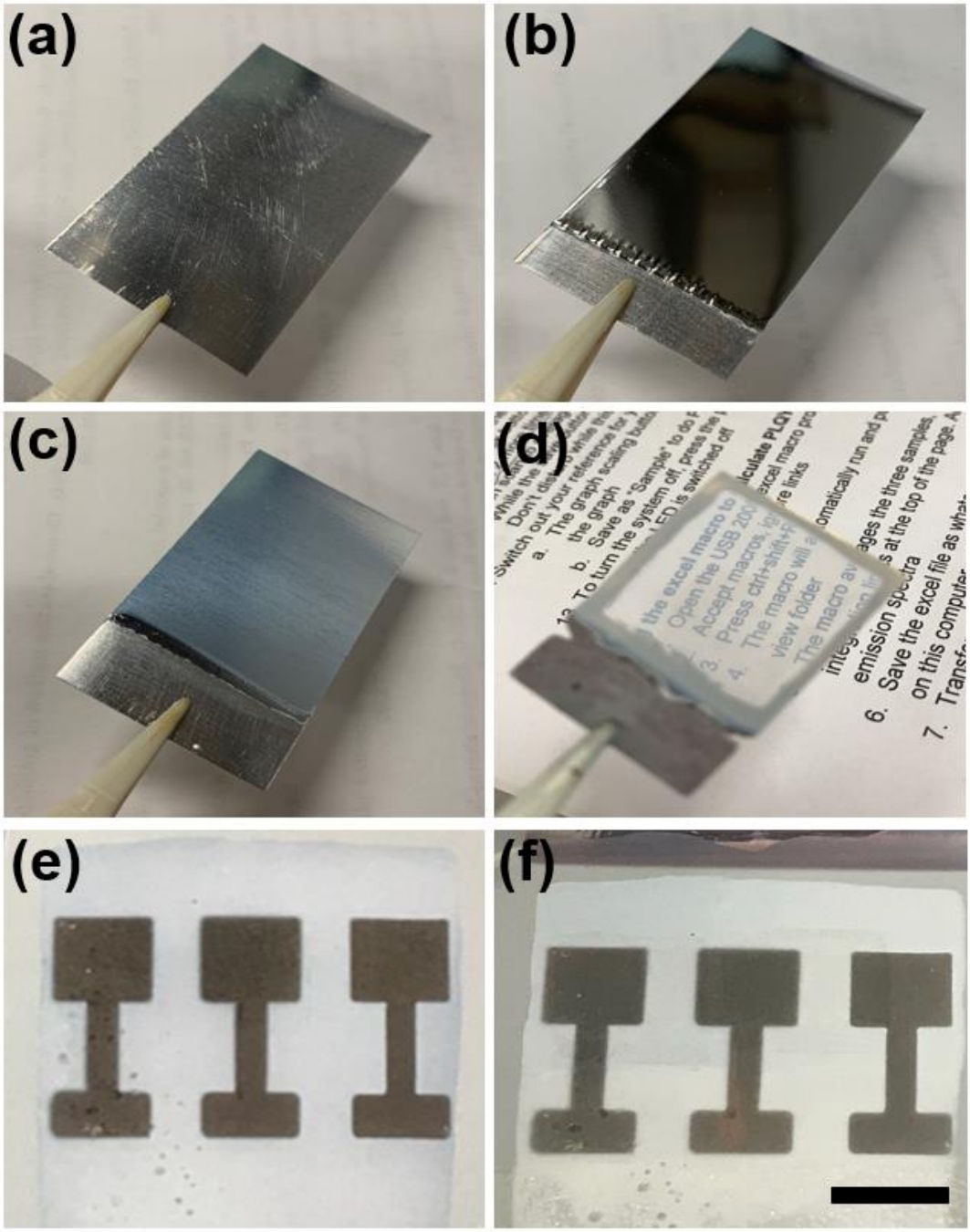

Figure 4.1 Fabrication flow chart for the device. (a) Al plate, after (b) Electropolishing, (c) Anodization, (d) Etching Al and barrier layer, (e) Au electrode deposition, and (f) Graphene transfer. (scale bar = 5 mm).

Figure 4.1 (a) and (b) show the images of the Al plates before and after electropolishing process, respectively. The polished surface shows a much smoother and more reflective surface like a mirror. Figure 4.2 (a) and (b) are the SEM images for the surface of Al and the electropolished Al, respectively. We can also observe the surface roughness change by the SEM images. Here, a two-step anodizing method was used for the highly ordered porous structure. The polished Al plates were anodized in the oxalic acid solution (0.3 M) with 40 V for 15 h. The bath temperature was maintained at 1 °C during the anodizing process. The first step of the anodization targets the porous structures on the surface. However, the porous oxide layer is not a highly ordered structure because the highly ordered structure needs a pre-structure which is a seed for the second oxide layer. This means that the first anodizing process helps the second anodization. After the first anodization, the oxide layer was removed by the mixture of phosphoric acid and chromic acid to achieve an ordered pre-structure on the surface. In the second anodization, we can get a much more ordered oxide structure because the chemical reaction starts from the pre-structure. The second anodizing process was carried out under the same condition as the first anodization. The only difference is the processing time. Since the thickness of the oxide film depends on the anodizing time, the Al plate needs to be anodized for at least 10 h to be the free-standing substrate. Before the second anodizing step, the backside of the Al substrate needs to be covered by a polymer to shield the Al from the oxidation reaction. The polymer used is poly(methyl methacrylate) (Sigma-Aldrich, 182265, PMMA). Figure 4.1 (c) shows the anodized sample after the 10 h process. The

white oxide layer is observed by the naked eye. Figure 4.2 (c) demonstrates the surface structure after finishing the second anodizing process. The highly ordered porous structure is detected in the SEM image. In the next step, the free-standing Al oxide film can be obtained by etching the Al which is on the backside of the sample. The Al can be etched by a solution consisting of $CuCl_2$ (3.4 g), HCl (38 %, 100 ml) and H_2O (100 ml). After finishing the etch process, we can obtain the free-standing aluminum oxide layer which has a highly ordered structure. Figure 4.1 (d) is the image of the free standing AAO substrate which is transparent because of the thin and porous structure. The backside of the free-standing film needs to be floated on the KOH (0.1 M) solution to remove the barrier layer from the bottom. The oxide layer is completely perforated after this process. The highly ordered and perforated holes are observed in figure 4.2 (d). The porous structure is more obvious when compared with the previous SEM image in figure 4.2 (c). Figure 4.2 (e) is the side view of the AAO structure. We can confirm the perforated holes by the SEM image.

For the device fabrication, Au (150 nm) was deposited onto the AAO substrate by an e-beam evaporator. During the deposition process, the substrate is covered with the shadow mask for the electrode structure. Figure 4.1 (e) is the image of the Au electrode on the substrate. The next step is the graphene transfer process. The graphene was synthesized on copper foil by the CVD method and transferred using the PMMA method. To achieve this, PMMA needs to be coated on the synthesized CVD graphene.

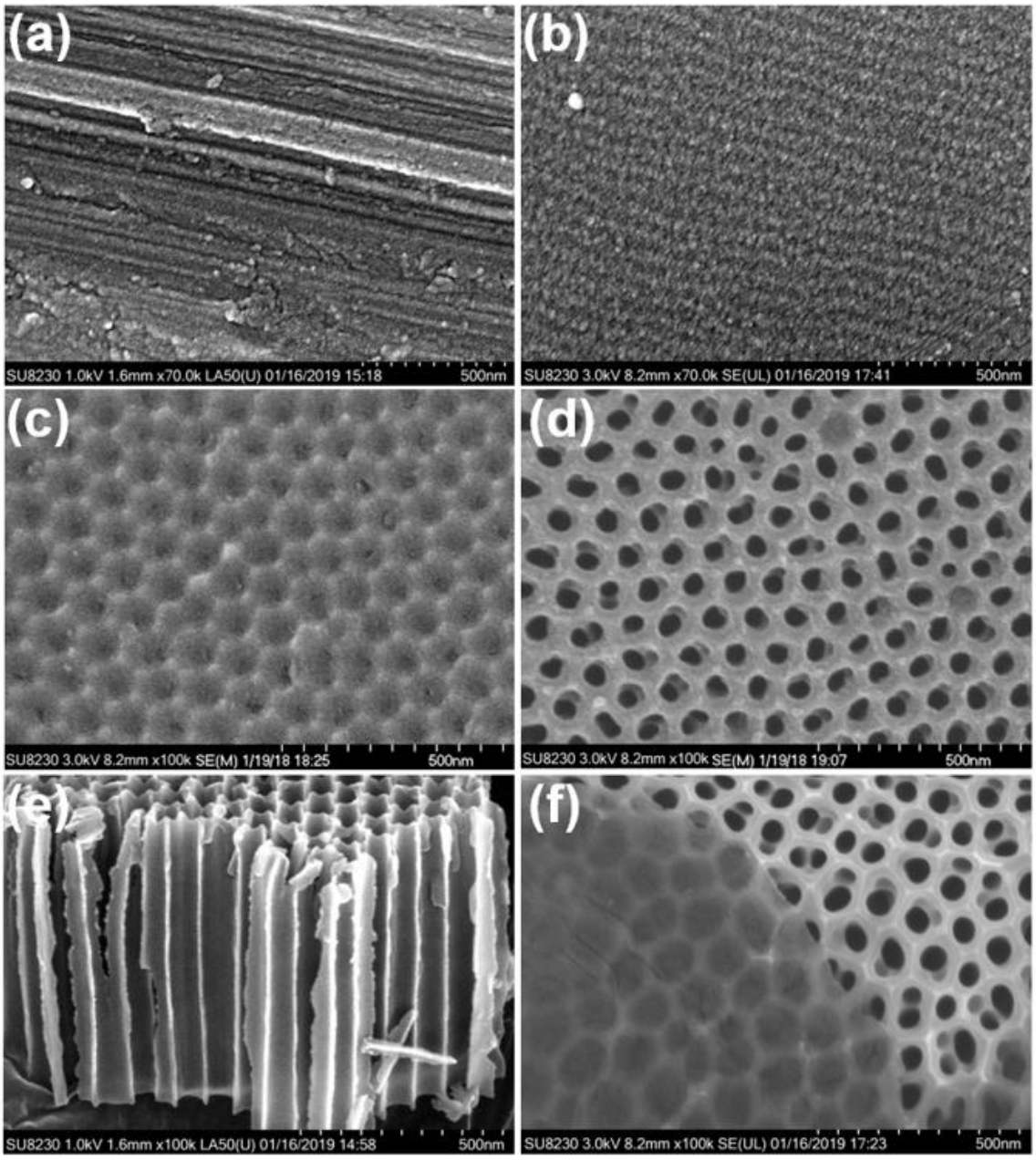

Figure 4.2 SEM images of the Al and AAO substrates (a) before and (b) after electropolishing, (c) after anodization, (d) after etching the barrier layer, (e) side view of AAO substrate, and (f) after transferring graphene on AAO substrate.

After etching the copper foil, the PMMA/graphene film was transferred to the AAO substrate. The PMMA can then be removed by acetone. The detailed transfer process can be found in previous research [126]. Figure 4.1 (f) shows the device after the graphene transfer process. The thin graphene layers are located between the Au electrodes. We tried to show the transferred graphene through SEM and successfully demonstrate the graphene layer on the AAO substrate.

As shown in figure 4.2 (f), the graphene layer is suspended on the AAO substrate. Since graphene should be exposed to the solution during the measurement, the other parts need to be covered by the PMMA layer. Next, the graphene layer is treated by the selective membrane solution for nitrate detection. Following similar previous research, the nitrate selective membrane solution was prepared with polyvinyl chloride (PVC), plasticizer and nitrate ionophore [127]. Here, the plasticizer is 1-(2-Nitrophenoxy)octane (NPOE) which has been widely used as a highly lipophilic plasticizer for the membrane fabrication. First, PVC powder (90 mg) is dissolved in tetrahydrofuran (2 mL). Then nitrate ionophore (30 mg) is added to the PVC mixture, followed by adding the NPOE to the solution. The synthesized solution is then coated on the graphene by a drop-casting method. Now, the devices are ready to be tested.

4.1.3 Results and discussion

In these measurements, there are three electrodes including the drain, source and reference, as shown in Figure 4.3 (a). We applied 0.05 V between the drain and the

source electrodes and swiped the voltage (-1 ~ 1 V) to the reference electrode which is also called the gate voltage. The measurement system is the same as the traditional IS-FET measurement system. The graphene based IS-FET shows the U-shaped curve in the transfer curve which shows the Dirac point of graphene. The transfer curves are measured by a semiconductor analyzer and DI water was used for the test.

Figure 4.3 (b) demonstrate the side view of the device structure. The working principle of the selectivity can be explained by this figure. The nitrate selective membrane is directly applied to both sides of graphene. The nitrate selective membrane can recognize nitrate ions in water and absorbs the ion inside of the membrane because of the properties of the components in the membrane.

To understand the principle of this mechanism, we need to know the components of the selective membrane. Methyltriphenylphosphonium (MTPP)-bromide and Tridodecylmethylammonium (TDDMA)-nitrate are the main components of the selective membrane. MTPP-bromide is the ion exchanger and TDDMA-nitrate is the ionophore. Since the bromide and nitrate ions in the membrane dissolve into the applied solution, the membrane is left with a positive charge which causes the shift to the left side. When the membrane meets nitrate ions in the solution, the membrane loses the positive charge. This phenomenon affects the current density of graphene. Finally, it makes a Dirac point shift in graphene. For these reasons, we can only detect nitrate without the interference of other ions.

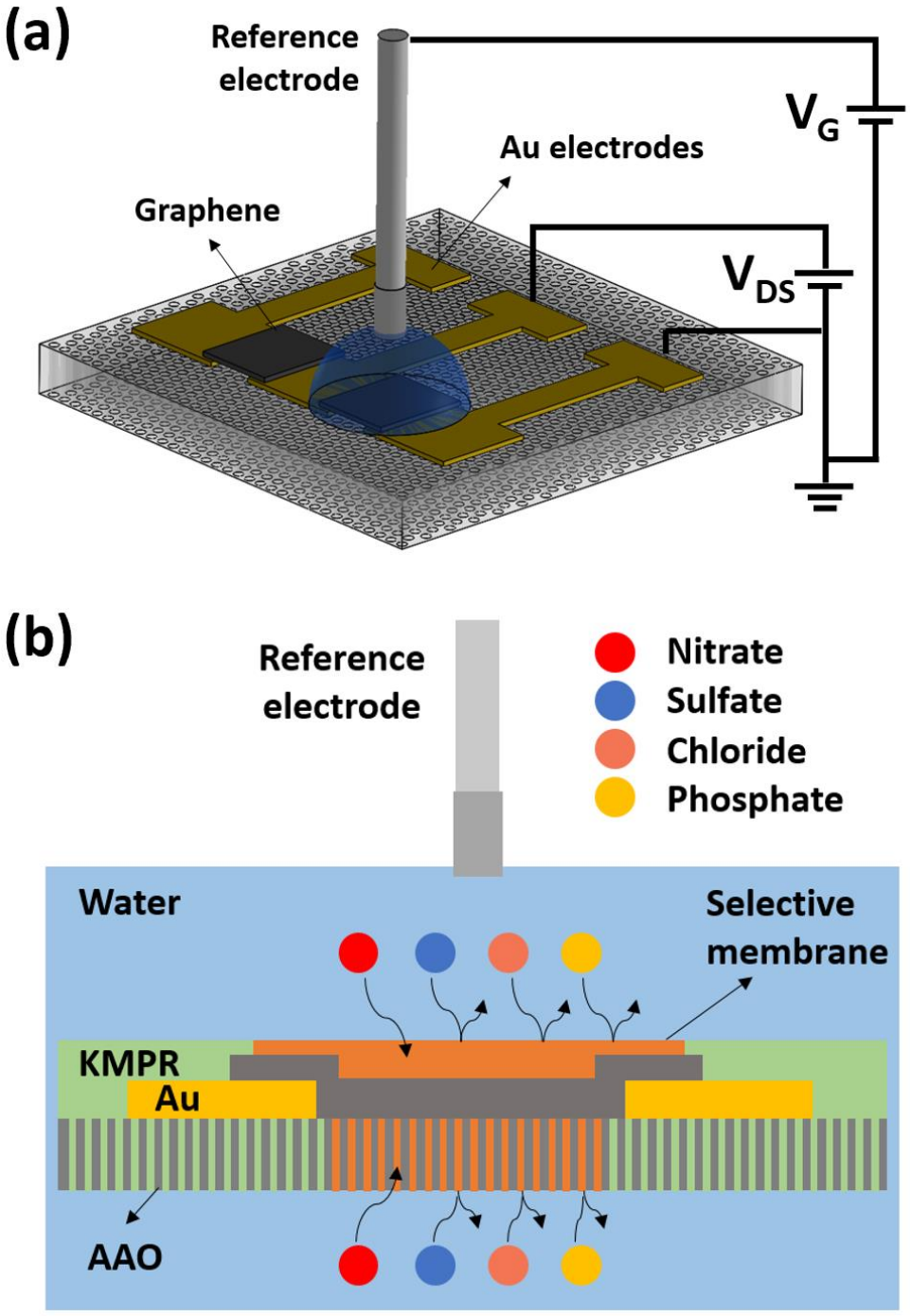

Figure 4.3 (a) Schematic diagram of the measurement system for graphene IS-FET (b) Schematic diagram for the mechanism of nitrate selective membrane.

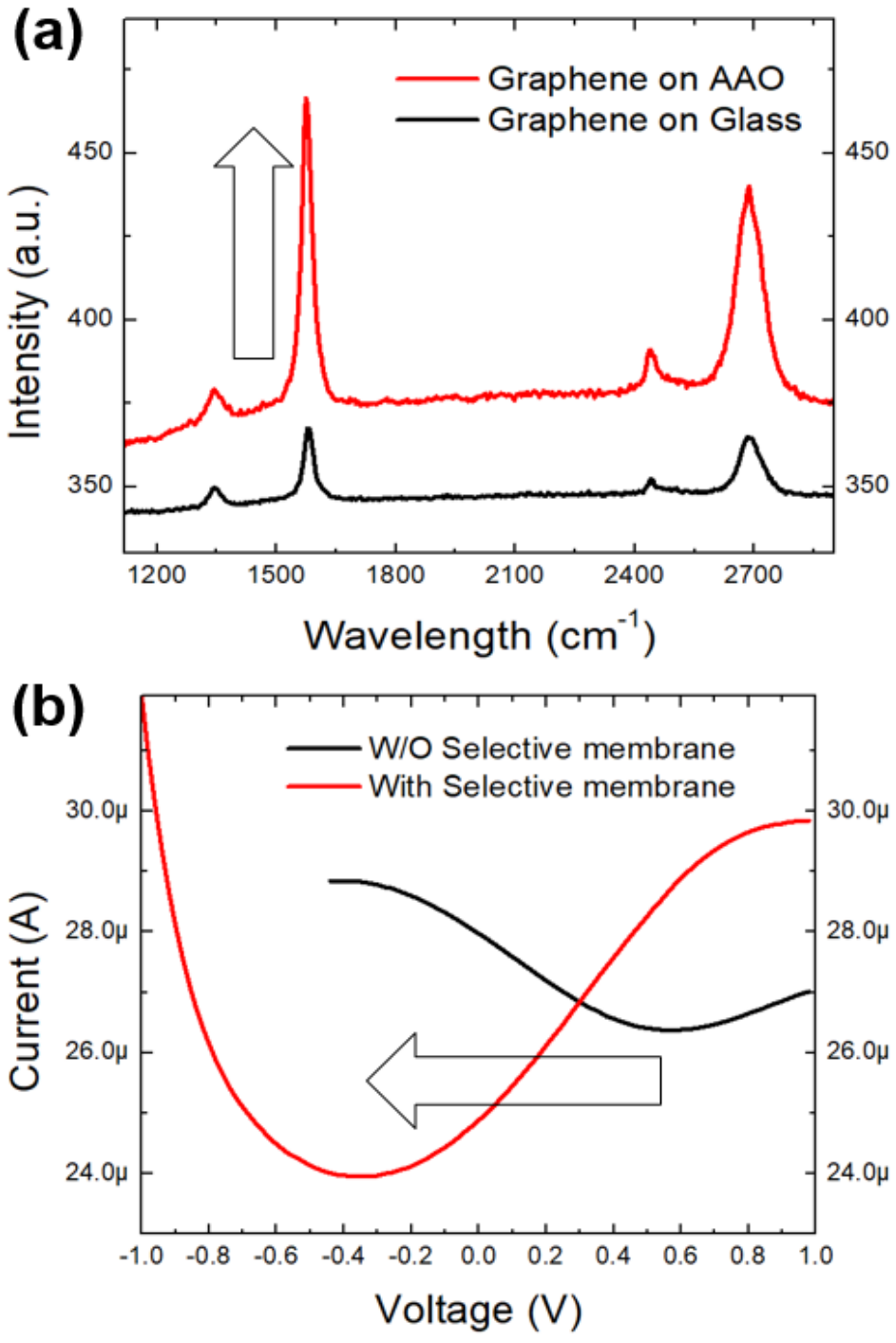

Figure 4.4 (a) Raman spectroscopy of graphene on glass and AAO substrate. (b) Transfer curve of graphene FET before and after coating the nitrate selective membrane.

This mechanism can be solved by the ion concentration induced solution-membrane interface potential change [128]. As shown in figure 4.3 (b), KMPR was coated on both sides of the Au electrodes to prevent the leakage current of the device.

The quality of the transferred graphene is tested by Raman spectroscopy. Graphene is transferred to the AAO substrate and glass substrate for measurement. In figure 4.4 (a), we obtained the signature peaks for graphene which are the D, G and 2D peaks. Single layer graphene specifically shows higher 2D peak intensity than G peak. Here, the intensity of the 2D peak is lower than G peak. This shows that the synthesized graphene is a few layers thick. Based on the research, the graphene has about 3 layers of thickness. Figure 4.4 (a) also shows an increase in the overall peak intensity on the AAO substrate. This result comes from the surface-enhanced Raman scattering effect [129]. The nanoporous structure of the AAO film enhances the peak intensity. It shows that we had successfully fabricated the device which has suspended graphene layers on the AAO substrate.

Figure 4.4 (b) shows the transfer curves for the device before and after coating the nitrate selective membrane. Before coating the membrane with graphene, the Dirac point was located on the right side of the graph. However, the graph shifted to the left side with the nitrate selective membrane. This means that the Fermi level of graphene is changed by applying the membrane because of the positive charges of the selective membrane [130]. The Dirac point was changed from 0.6 V to -0.4 V with the membrane. This also shows

that the main carrier of graphene is changed from holes to electrons. From these results, we can confirm that graphene sensitively responds to the surrounded environment.

The mechanism of nitrate detection can also be explained by the Dirac point shift. The charge carrier density of graphene can be changed by the concentration of the ionic solution. This phenomenon can be described by the potential difference between the selective membrane and ionic solution. The potential difference is changed by the concentration of the ionic solution. This causes the change of charge carrier density of graphene. Finally, we can detect the concentration change by measuring the Dirac point shift in the graphene based IS-FETs.

We prepared solutions that have different nitrate concentrations from 0 ppm to 10 ppm, including sulfate, chloride and phosphate. Figure 4.5 (a) depicts the response of the sensor depending on the concentration of the nitrate solution. Here, we can see that the Dirac point was shifted to the right side from the starting point. The Dirac point was located to -0.4 V with DI water. However, it starts to shift to the right from the original point. As we increased the concentration of the solution, the Dirac point shifted to -0.3 V. In this graph, we demonstrated that the carrier concentration in graphene is changed by the surrounded ions in water. Figure 4.5 (b) shows the real-time current measurement of the IS-FET sensor which can demonstrate the response time and the reusability. Changing solution causes the sharp peaks and the current levels to be recovered right after changing the solutions. The current level reaches about 90 % of final amplitudes in 3 seconds.

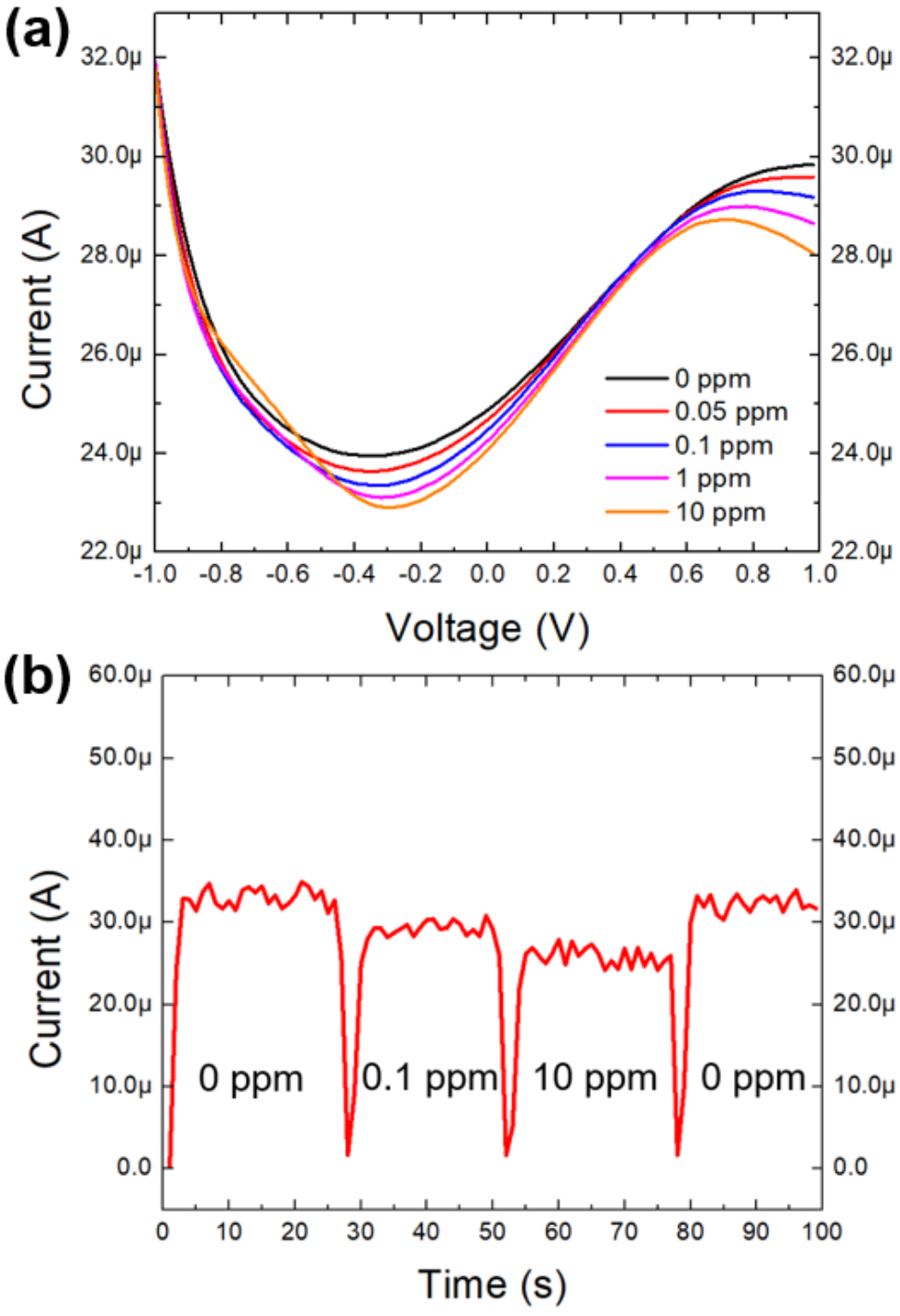

Figure 4.5 (a) Transfer curves of graphene IS-FET with the nitrate selective membrane. (b) Real-time current measurement of the IS-FET sensor when exposed to different concentrations.

The reusability of the sensor is also verified by showing the current level of the previous current in the same solution. Once the nitrate concentration is decreased, the current level is recovered to 30 μA again in DI water. The result confirms that the sensor can be reusable and be used for monitoring the quantity of nitrate in water.

Subsequently, we also characterized the sensors with several ions to check the function of the selective membrane. The different solutions are applied to the same sensor. When each solution is applied to the sensor, the transfer curve was measured. Finally, we collected the data and drew the concentration versus the Dirac point shift graph to analyze the relationship between the two parameters. Figure 4.6 demonstrates the relationship. As described, IS-FET shows the response to nitrate solutions. The Dirac point was shifted up to -0.1 V as the nitrate concentration increased. However, the sensor didn't show a shift of the Dirac point with other solutions including sulfate, chloride and phosphate. Although there were smaller shifts with those solutions, the difference was clear. The error bars include the results from 5 different devices. The performance of the nitrate selective membrane is verified by the results.

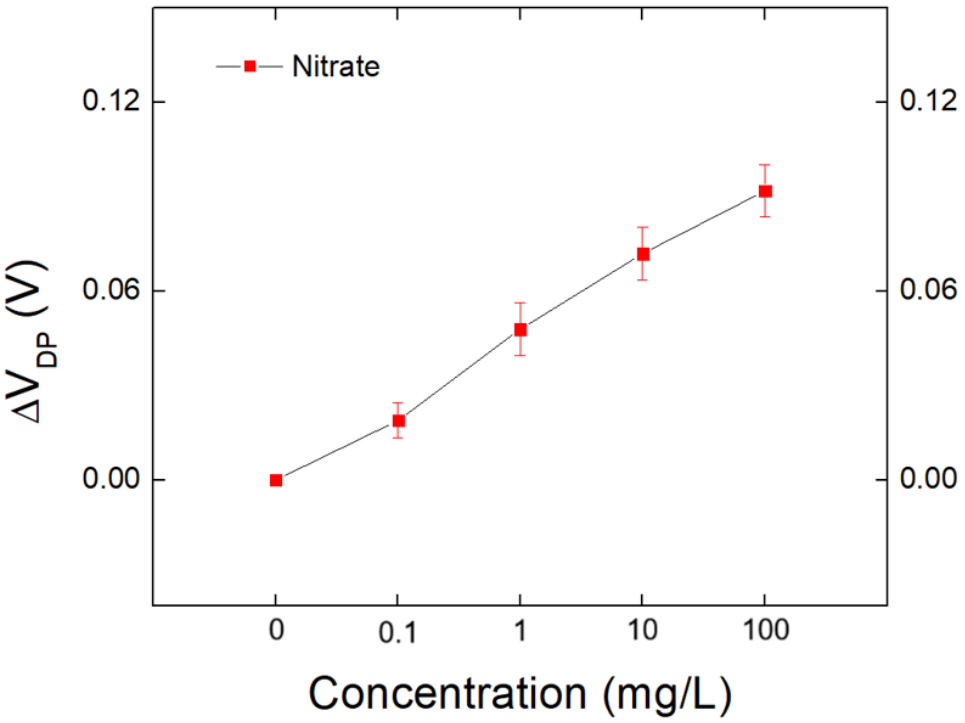

Figure 4.6 Selectivity of the nitrate selective membrane.

In this work, we successfully fabricated and characterized graphene based IS-FET on the AAO substrate. The detection limit and response time are enhanced compared to the device on SiO_2 [131]. In our previous results, the detection limit was 0.82 ppm but is now improved to 0.32 ppm in this work. The devices show a measurable response within 3 s. Based on the above results, we show the IS-FET can be a great candidate for the next generation of ion sensors.

4.1.4 Conclusion

Au electrodes are deposited on the AAO substrates which are prepared by a two-step anodizing process. The nitrate membrane is synthesized by mixing nitrate ionophore, PVC, and plasticizer in the solvent. For the selective membrane, the synthesized solution was directly applied to the graphene surface. The sensor performance was demonstrated by the semiconductor analyzer to measure the shift of the Dirac point of graphene. The Dirac point of graphene was changed from 0.6 V to -0.4 V after coating the selective membrane because of the charge of the membrane. The Dirac point starts to shift towards the right depending on the concentration of nitrate and the sensors are nitrate specific. We successfully demonstrate that the IS-FET can be a promising candidate to quantify nitrate ions in water.

4.2 Graphene Based Temperature Sensors Suspended by Anodic Aluminum Oxide

In the research, we investigate the substrate effect in graphene temperature sensors. Recently, there have been many research studies done on temperature sensors using nanofabrication techniques. However, the sensitivity and response time need to be improved. In this study, we propose a new type of temperature sensor which consists of graphene and Anodic Aluminum Oxide. For this device, graphene and AAO are used for the sensing material and the substrate, respectively. We characterize the sensitivity and the response time using the experimental results and simulation data. The real-time resistance change of graphene is monitored depending on the temperature and the

response time is also analyzed by COMSOL Multiphysics. To confirm the porous substrate effect, we compare the device performance of the AAO substrate to the performance of the glass substrate. In the results, the suspended graphene on the AAO substrate shows about 2 times higher sensitivity and much faster response time than the glass substrate.

4.2.1 Introduction

Temperature is one of the most important physical parameters that are closely related to our lives. Especially body temperature is an important parameter related to our health. Therefore, various temperature sensors have been developed by many research groups and companies. Among temperature sensors, some devices are already commercialized in the market including mercury thermometers and infrared thermometers that use different materials for sensing temperatures such as ceramics, polymers, metal and metal oxide. The sensing materials are different, but most temperature sensors measure a certain change to show a specific value temperature. Although these thermometers have several advantages, they still need to be developed to overcome the following limitations. Daniel Gabriel in 1714 invented the mercury thermometer, which is still widely used in our life due to its accuracy [132]. However, it still has various disadvantages such as slow response, difficulty in reading and the use of a toxic sensing material that can cause the disease called Minamata [133,134]. The infrared thermometer is a compact, light, fast and simple device that can measure temperature from a distance. However, the results

can be easily affected by dust or humidity and it is also quite expensive depending on the accuracy and range of temperature.

To solve these problems, many research groups are researching the resistance change measurement which is a well-known temperature sensing mechanisms because of its accuracy and simplicity [135]. This thermometer uses a carbon-based material that is used as the sensing material with outstanding mechanical and electrical properties [136]. Among carbon-based materials, various graphene derivatives have also been used for various applications such as solar cells, diodes, ion sensors and optical sensors [137-144]. We apply a few layers of graphene due to the high mobility of its charge carriers. At baseline graphene based body temperature sensors have high sensitivity and accuracy and the sensitivity can be enhanced further by changing the substrate which suspends graphene [145]. Here, we investigate how the substrates can affect the sensitivity of the temperature sensor. Anodic aluminum oxide (AAO) substrate is prepared for the porous substrate that can suspend graphene and the glass substrate is also prepared for the flat substrate [146]. To compare the relative performance, graphene is transferred onto the AAO substrate and glass substrate.

Several research groups have reported on the relationship between the resistance change of graphene and temperature change [147]. In the studies, graphene shows a negative value for the temperature coefficient of resistance (TCR) between 35 and 45 °C [148]. The negative TCR comes from the negative coefficient of thermal expansion (CTE) [149]. The CTE of graphene can be changed from negative to positive depending on the

temperature range [150]. To be specific, graphene has negative thermal expansion at relatively low temperatures, but it shows positive thermal expansion at high temperatures. The transition is caused by two competing effects: positive thermal expansion because of in-plane modes and negative expansion because of out-of-plane fluctuation [151]. For this reason, graphene exhibits positive CTE at a relatively high temperature and it shows a negative value at low temperatures [152]. Therefore, a negative TCR can be expected between 35 ~ 45 °C because of the negative CTE value in this temperature range. The TCR values of the graphene in different substrates are derived from experimental results using an equation that includes initial resistance and the slope of the temperature-time graph [153]. Since the high TCR value means that the resistance can sensitively respond with temperature, the comparison of the TCR value is necessary to compare the substrate effect of graphene based temperature sensors.

4.2.2 Materials and methods

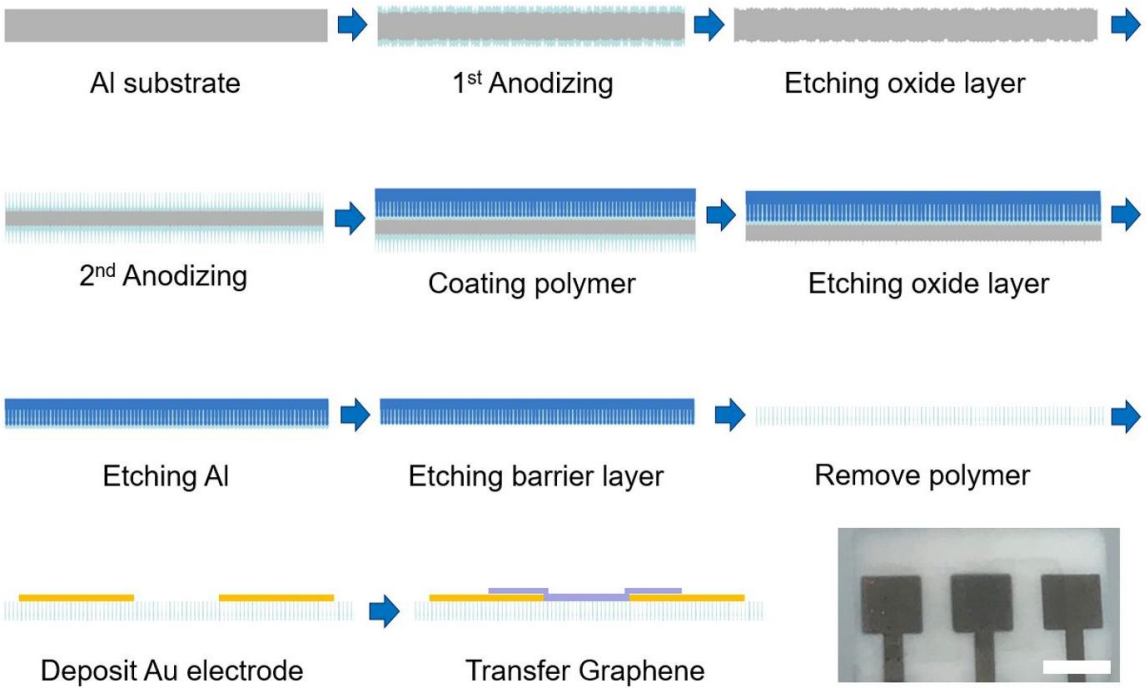

Figure 4.7 Fabrication flow chart for the AAO substrate and the fabricated device. The scale bar is 5 mm.

To compare the effects in different substrates, devices were fabricated on two different substrates including glass and AAO. The Al plates (ZhongNuo, YJ13G04) and the glass (Gold Seal™ Cover Slips) are used for the fabrication of AAO substrate and a glass substrate, respectively. Firstly, the glass (18 mm x 18 mm x 0.15 mm) and the Al plate (20 mm x 30 mm x 0.3 mm) substrates are prepared and cleaned to remove surface impurities by the following process. The substrates are cleaned with Trichloroethylene for 15 min using sonication. The same process is repeated with acetone and methanol to

finish the cleaning process. Before starting the anodization process, the Al plates is polished by electrical method (20 V for 4 min) using a solution of perchloric acid and ethanol (1:3 volume ratio) and running a voltage. The surface of Al plates is smoothed through the polishing process. As a result, the surface can reflect light like a mirror. It is very important to achieve a smooth surface for the fabrication of a uniform porous structure.

Figure 4.7 illustrates the device fabrication process with the AAO substrate. Firstly, the polished Al substrate needs to be anodized twice. This process is called two step anodizing method. The Al substrates are anodized in phosphoric acid (1 wt%) solution with a voltage of 40 V. In the anodizing process, the temperature is also an important parameter to achieve a uniform structure. The temperature needs to be maintained at 1 °C for the anodizing process to occur slowly. Both anodizing processes use the same solution, temperature and voltage. However, for the first anodization, the voltage is applied to the substrate for about 10 h to achieve uniform dents on the surface. Although the porous structure can be formed during the first anodizing process, the surface of the oxide layer is not uniform. Thus, the first anodized oxide layer is to be etched away by Al oxide etchant (70 °C for 3 h) that consists of chromic acid and phosphoric acid. After etching the oxide layer, the Al surface has the uniform dents that can be used to seed the next porous oxide layer. In the second anodizing process, the oxide layer can be formed from the dents to obtain a more uniform porous structure. The second anodizing process uses identical conditions for the temperature, solution and voltage but finishes within a

few minutes. Hence, the entire process to achieve a thick AAO film lasts for 15 hours. The next procedure is the backside AAO etching step. Before the etching step, PMMA is coated on the AAO substrate to protect the oxide layer from the oxide etchant. Once coated, the plate is ready to etch on the Al. For etching Al plate, the AAO/Al substrate is dipped into the Al etchant (3.4 g $CuCl_2$, 100 ml HCl (38%) and 100 ml H_2O) until the reaction is finished. Then the barrier in the remained oxide layer needs to be etched away by KOH solution (0.1 M). The barrier layer etching is a very sensitive process because it is easy to lose the oxide layer in the etching process. The coated polymer can be removed by acetone.

The next step is device fabrication. First, Au (100nm) is deposited on the AAO substrate using sputtering. Graphene is synthesized by the chemical vapor deposition (CVD) method based on the previous research [154]. The synthesized graphene consists of 3 layers of graphene. Graphene needs to be transferred to the target location that is between both Au electrodes on the AAO and glass substrates. To protect graphene during the next processes, PMMA is coated on graphene and the below copper foil is etched by the copper etchant (50 ℃ for 1 h). After the etching process, the PMMA/graphene film floats in the etchant. The film is rinsed by DI water and transfers to the target location. Acetone is used to remove the PMMA layer on graphene. The last image in figure 4.7 shows the graphene on the device after the transfer process. The transferred graphene is patterned by oxygen plasma to define the current path using a shadow mask. The size of the graphene sheet is 3 mm x 4 mm [155].

4.2.3 Results and discussion

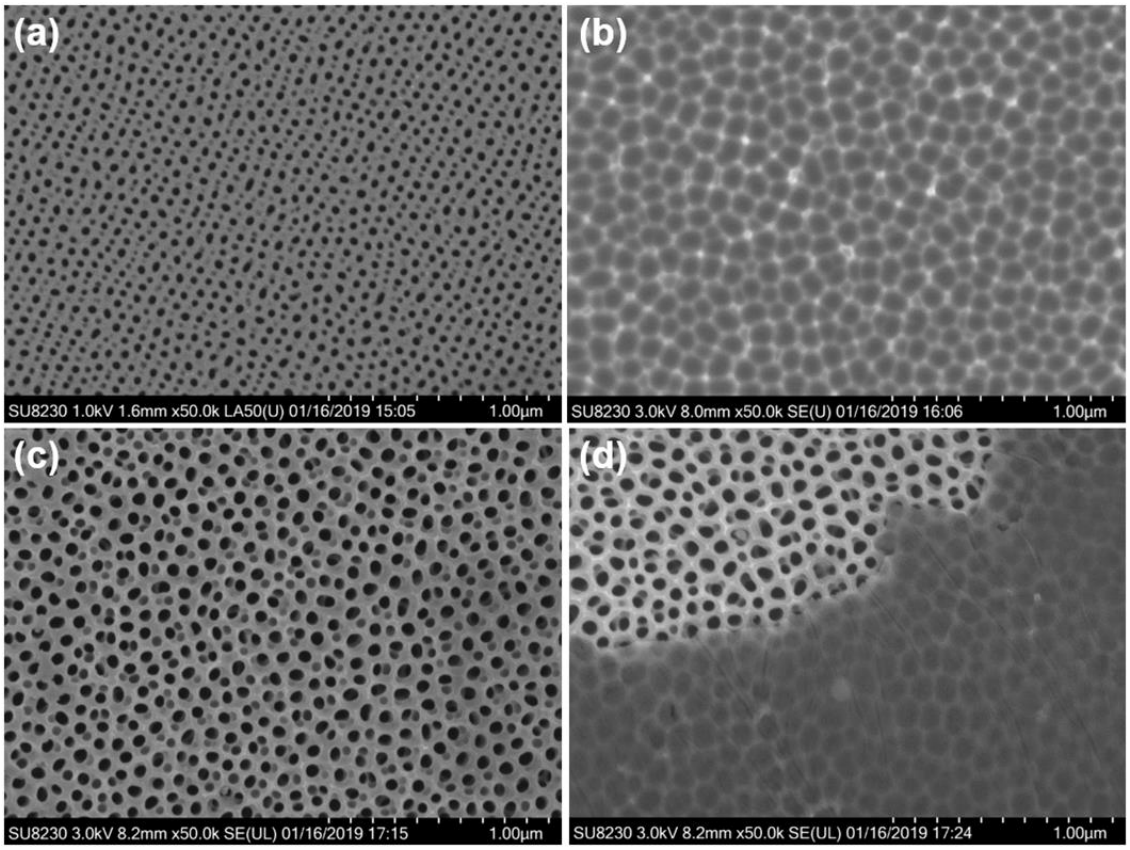

Figure 4.8 SEM images of the AAO substrates (a) after first anodization, (b) after etching the oxide layer, (c) after second anodization and (d) after transferring graphene on AAO substrate.

Figure 4.8 shows the SEM images of the surfaces after each step. First, figure 4.8 depicts the AAO surface structure after the first anodizing process. In this image, the uniformity and size of the pores can be observed. Each pore size is about 50 nm. The first anodized film is then etched before the second anodizing process. After etching the porous oxide

layer, the surface shape is characterized by SEM. Figure 4.8 (b) demonstrates the morphology of the surface after etching. We can observe the bottom of the oxide layer from this image. The smooth Al surface has specially shaped dents after the oxidation process of the Al surface by the applied voltage in the solution. Each dent has a hexagon shape. Since the second anodizing starts from these dents, we hope to obtain a more uniform porous structure. More uniform dents lead to a more uniform porous structure. Therefore, the first anodizing process is the key step for structure uniformity.

For the second anodizing process, the same solution and voltage are applied a second time to the Al plate with dents. And then the backside of the AAO layer and Al part are etched by their respective etchant. The detailed processes can be found in our previous research [156]. Figure 4.8 (c) shows the surface structure of the AAO layer after removing the barrier layer from the backside. The AAO is fully formed through the structure. In the figure, the porous structure is observed. After Au deposition using sputtering, CVD graphene is transferred on to the AAO substrate. Figure 4.8 (d) depicts the transferred graphene layers on the porous structure. The graphene film is seen covering a portion of the AAO substrate, and the porous structure can be observed through the thin graphene film. The wrinkle of the graphene sheet can also be founded in the image. The next step is confirmation of the graphene.

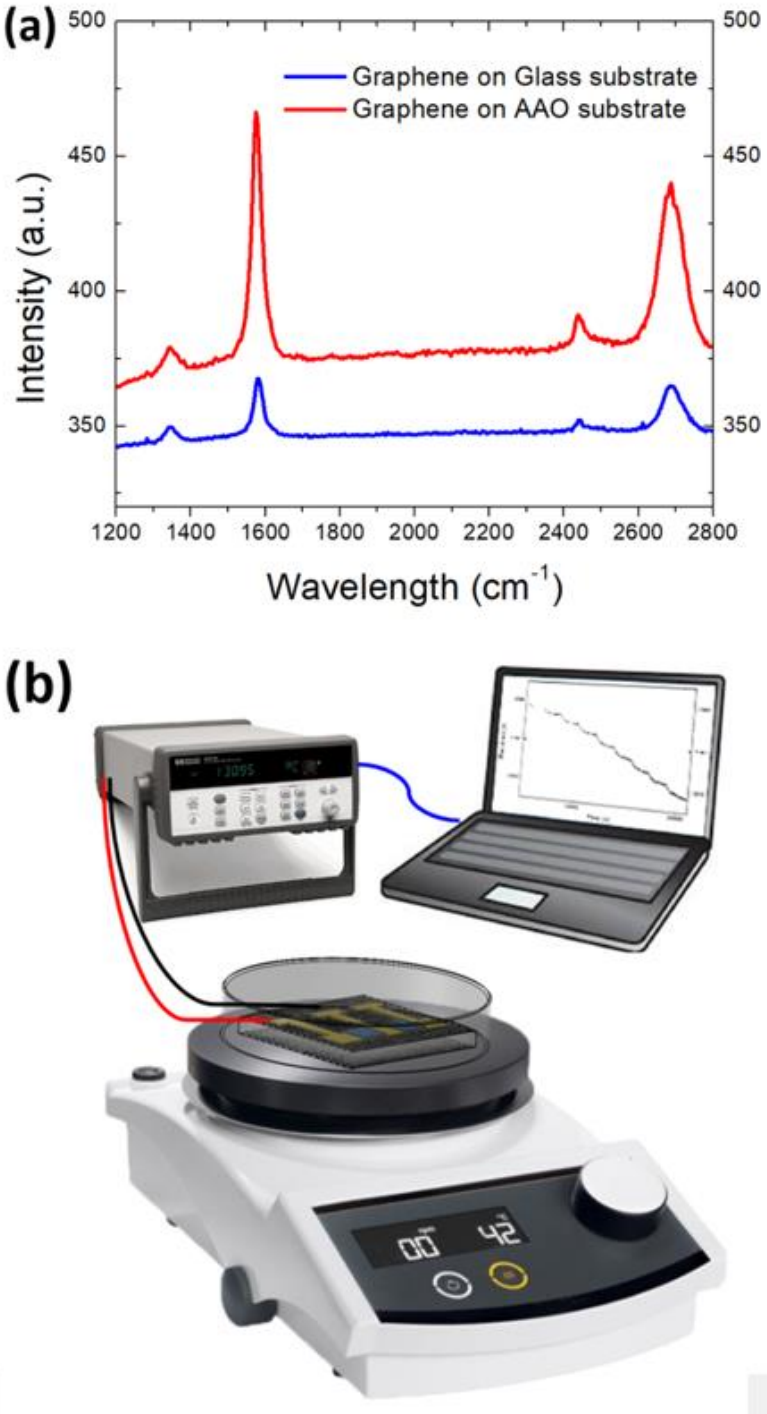

Figure 4.9 (a) Raman spectroscopy of graphene on glass and AAO substrate (b) Schematic diagram of the measurement system.

Graphene is transferred to both substrates including glass and AAO substrate. The transferred graphene films are characterized by Raman spectroscopy. Figure 4.9 (a) shows the Raman spectroscopy of graphene on AAO and glass substrate. The graphene on an AAO substrate displays higher intensity in the graph than the graphene on a glass substrate. Both curves have the main peaks of graphene such as D, G and 2D peaks represented at 1350, 1590 and 2700 cm^{-1}, respectively. In both substrates, the peak locations are exactly the same. However, there is a noticeable difference in the intensity of the peaks.

The high intensity in the AAO substrate can be explained by the following reason. Since nanostructures cause a phenomenon called the Raman scattering boost which leads to the surface-enhanced Raman scattering, the intensity of the peaks is increased by the nanostructure of the AAO substrate [157]. The thickness of graphene can be determined by comparing the intensity of G and 2D peaks. When graphene is a single layer, the intensity of the 2D peak is almost double the G peak intensity. However, the peak ratio is changed to the opposite as increasing the thickness of graphene. This means that the intensity of the G peak can be higher than the intensity of the 2D peak. In this experiment, we synthesize 3~4 layers of graphene and transfer it to the substrates. As a result, the Raman graph shows a reasonable peak ratio for 3~4 layers. The transferred graphene is appropriately characterized by Raman spectroscopy.

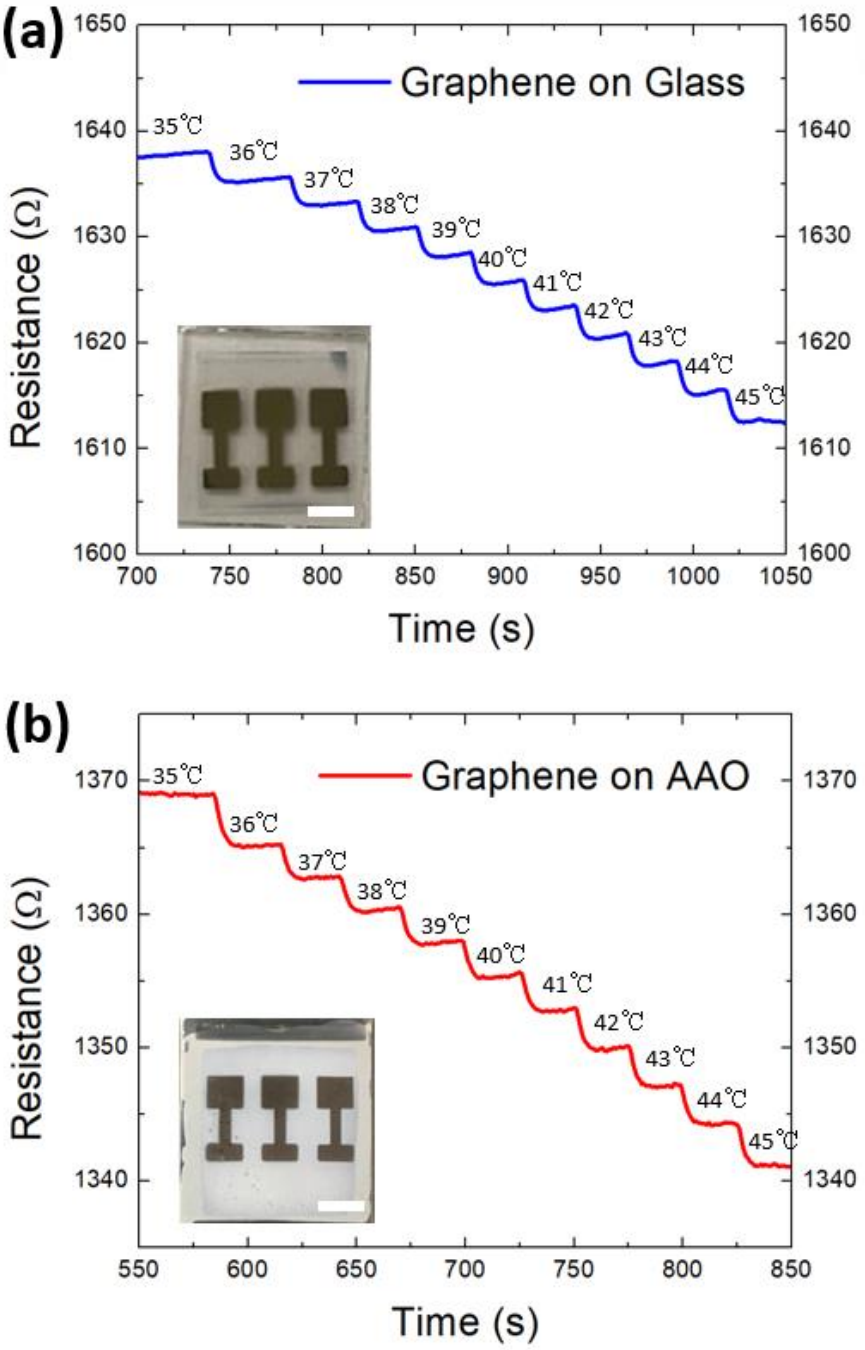

Figure 4.10 Comparison of the resistance change in the different substrate (a) Glass substrate and (b) AAO substrate. Inset images show the fabricated devices on different substrates. The scale bar is 5 mm.

Figure 4.9 (b) demonstrates the measurement system that consists of a hot plate, Agilent data logger and computer. The fabricated sensors are characterized by data acquisition equipment (Agilent, 34970A) which collects the resistance change of graphene as the resistance of graphene responds to the change in temperature. To measure the resistance of graphene, the wires are connected to the Au electrodes in the device. Then, the temperature of the device is controlled by the hot plate while the device is covered by the glass to reduce the effect of the heat dissipation from the device to air. The real-time resistance of the graphene is then collected by the data acquisition equipment and finally displayed in software on the computer.

Figure 4.10 shows the resistance change as the temperature is increased in the two different substrates. The temperature is increased from 35 °C to 45 °C to simulate the target objective of the human body. We measure the resistance changes for every 1 °C. Figure 4.10 (a) represents the resistance change of graphene on the glass. The fabricated device is shown in the inset image. The resistance is changed from 1638 Ω to 1612 Ω (Δ26 Ω) as the temperature increases to 45 °C. The temperature is changed after the resistance is stabilized. The resistance slightly increases after reaching the peak point because the equipment takes time to reach the set temperature. The measurement takes a total of about 350 s. Figure 4.10 (b) shows the response of the resistance of graphene on the AAO substrate. The resistance is changed from 1369 Ω to 1341 Ω (Δ28 Ω) as the temperature increases. The resistance is measured for a total of 300 s. Since there are a lot of factors that affect the initial resistance of graphene including the size of transferred

graphene, substrate and the quality of graphene film, the initial resistance is different for each sensor. Therefore, calculating TCR value is necessary for comparing the sensor performances.

The TCR values (α) can be obtained by:

$$\alpha = \left(\frac{1}{R_0}\right) \mathrm{X} \left(\frac{dR}{dT}\right). \qquad (1)$$

Where, (dR/dT) and R_0 is the change in resistance over time and the initial resistance, respectively [158]. Using equation (1), we obtain the TCR values for both devices. The TCR value of the sensor based on the AAO substrate is -20.45×10^{-4} °C $^{-1}$, and the TCR for the device based on the glass substrate is -15.87×10^{-4} °C $^{-1}$. In these results, we get a greater absolute TCR value in the AAO substrate and a negative TCR value. The negative value of CTE leads to a negative TCR value. This means that the resistance of graphene decreases with an increase in temperature. The higher the TCR value means that the most sensitive the sensor is in response to the temperature.

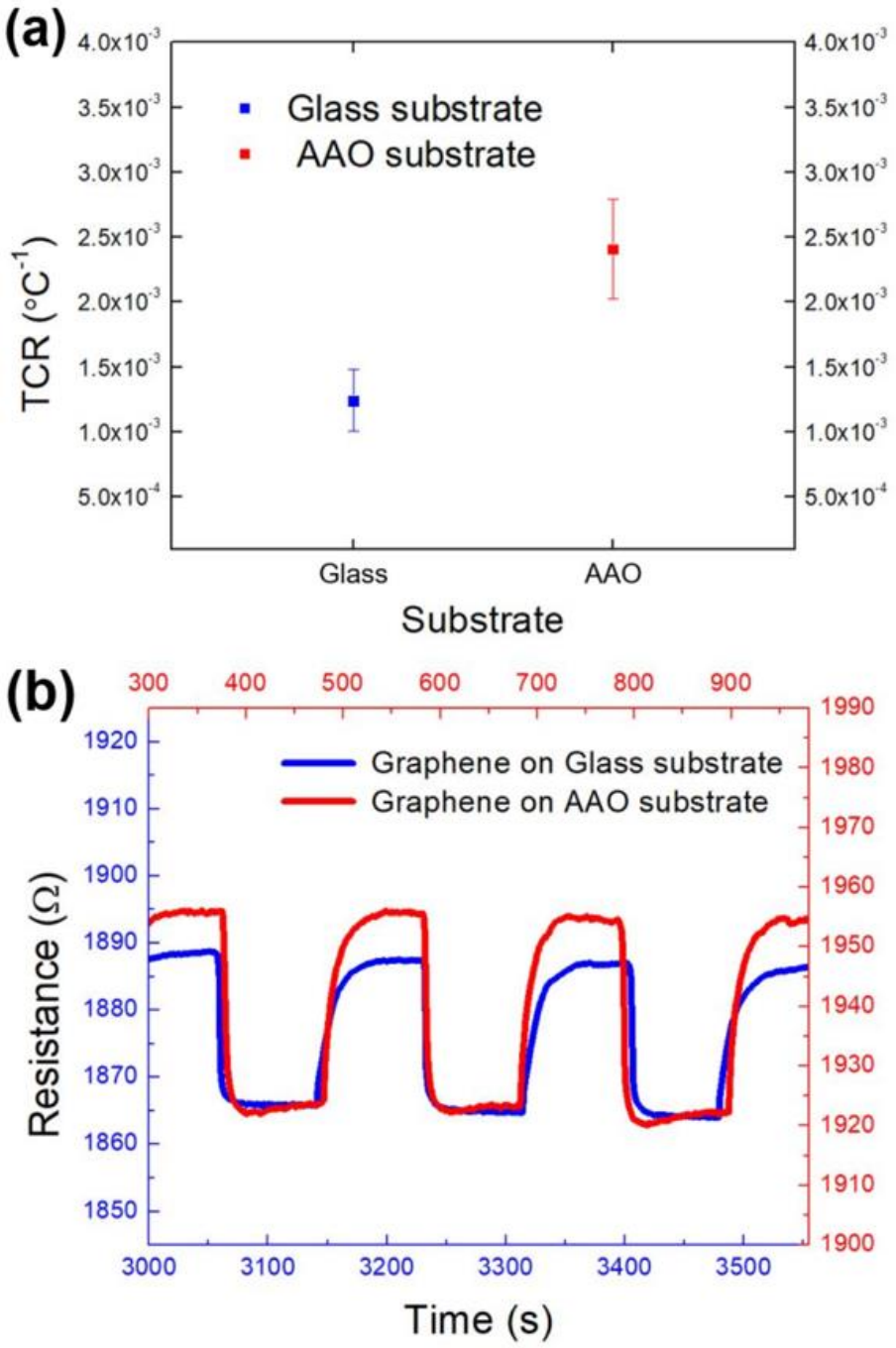

Figure 4.10 (a) TCR values in the glass and AAO substrate. Error bar comes from 5 different samples for each substrate. (b) Real-time resistance measurement of graphene-based temperature sensor when exposed to the different temperatures.

We prepared 5 devices and characterized the device performances to verify the TCR values. Figure 4.10 (a) represents the TCR values of the different substrates. TCR values are calculated using the equation (1), and the error bars indicate the range of performance for the 5 different devices. The average TCR values are $-12.4 \times 10^{-4}\ °C^{-1}$ and $-24.1 \times 10^{-4}\ °C^{-1}$ for the Glass and AAO substrate, respectively. Based on these results, we successfully verify that the graphene device fabricated on the AAO substrate has about twice the sensitivity compared to the device on the glass substrate.

Figure 4.10 (b) demonstrates a real-time resistance change of the sensors which were fabricated on the glass and AAO substrates. The sensors were exposed to two different temperatures which are room temperature (20 ℃) and 40 ℃. In the graph, the resistance level is decreased when the temperature is at 40 ℃. The resistance level is fully recovered at room temperature. It means that the graphene-based sensors can be reusable without any degradation caused by thermal oxidation. The graph also shows that the response time of the sensor on the AAO substrate is shorter than the sensor on the glass substrate.

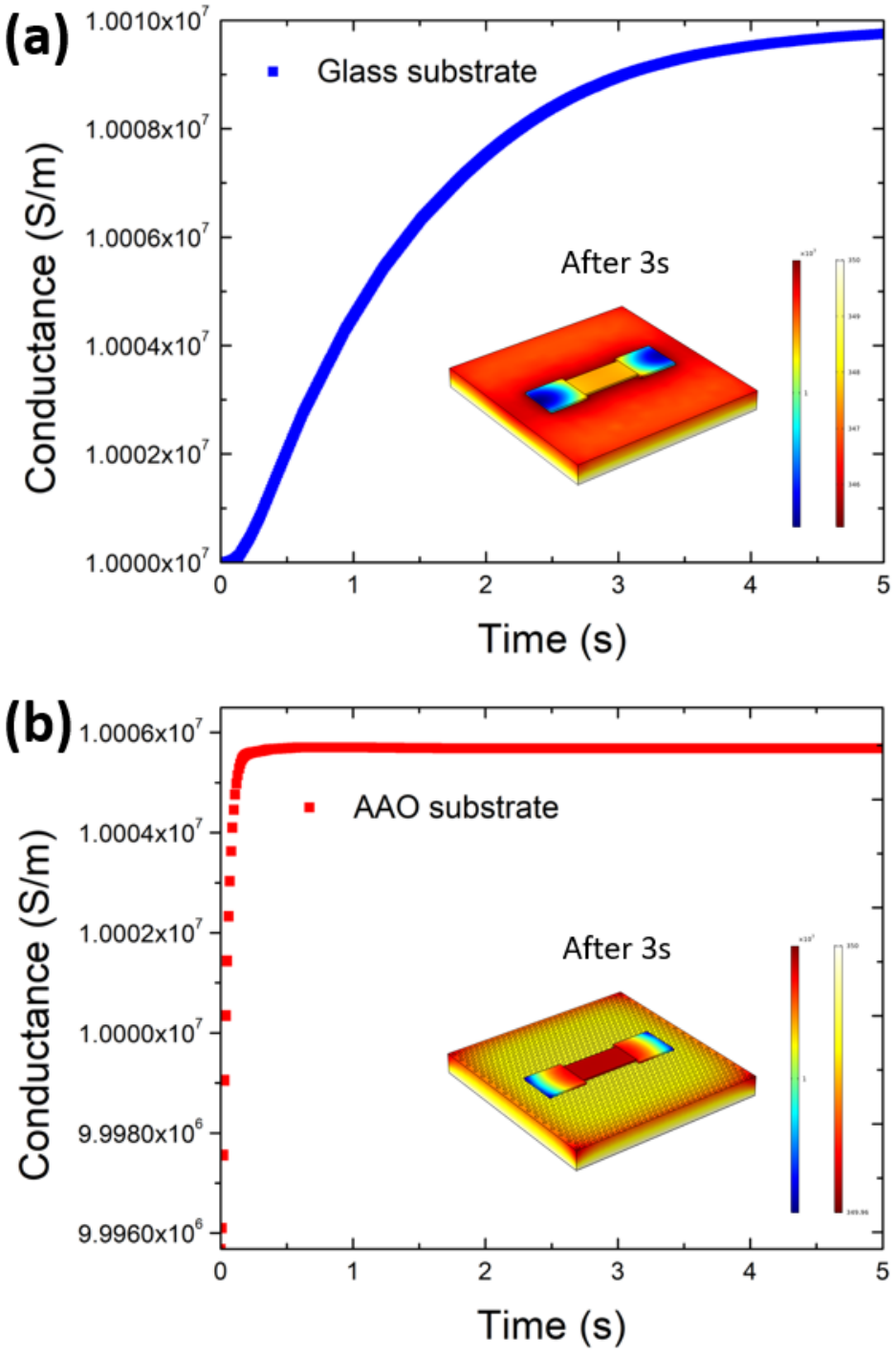

Figure 4.11 Comsol simulation results of the graphene's conductivity in different substrate (a) Glass and (b) AAO substrate.

COMSOL simulation software is used to estimate the response time of the graphene based temperature sensor. In the simulation, the conductance of graphene is calculated for 5 s after setting the new temperature. Figure 4.11 shows the conductance difference between (a) glass and (b) AAO substrates. Graphene is located between Au electrodes, and the heat source is at the bottom of the substrates. As shown in 3D figures in the graphs, two different devices are depicted in the simulation. The substrate size is assigned to 10 x 10 mm which includes the Au electrode and graphene. For the AAO substrate, Al_2O_3 is assigned as the material and the holes in the substrate are filled with air. Although we could not use the actual hole size in AAO because of the unit limitation, the coverage of holes in the AAO substrate is very close with the real value. There are over 1000 holes in the substrate which has 0.1 mm radius. The parameters are entered for materials including substrates, air and graphene based on the previous research which suggests the thermal conductivity, electrical conductivity and density [159]. Although we don't expect the exact same results with the experimental data because of the limitation of the simulation tool, the results can be used for estimating the relationship between the heat transfer in the different substrates and conductance change in graphene. The current temperature of the substrate is set to 310 K and the new bottom temperature is set to 320 K. Then, we observe the heat transfer in the substrates along with the conductance change of graphene for 5 s. In the 3D figures, we can notice that the AAO substrate has a brighter color than the glass substrate after 3 s. This is due to the better heat transfer performance of the AAO substrate than the glass substrate. Since graphene rapidly reacts with the

surface temperature of the substrate, the color of graphene also changes to red that shows a higher conductance level than the blue shown in the glass substrate. The results support that the AAO substrate can enhance the response time of the graphene based temperature sensor. In the experimental results, the device fabricated on the AAO substrate shows a faster response than the glass substrate. Therefore, the total experiment time is shorter with the AAO substrate. Finally, the device performances are successfully characterized by the experimental and simulation data.

4.2.4 Conclusion

In these experiments, we clarify the substrate effects in the graphene based temperature sensor. The devices are fabricated on glass and AAO substrates for comparison. The AAO substrates are prepared by a two-step anodizing method, and graphene is transferred between the Au electrodes on both substrates. The sensor performance is then demonstrated by measuring the resistance change of graphene depending on temperature. Based on the collected experimental data, TCR values are calculated by the equation to get the sensitivity of the sensors. The response time of the sensor is calculated by COMSOL simulation. The data shows that the AAO substrate is twice as sensitive and boasts a much faster response time than the glass substrate. In this work, we successfully demonstrate the substrate effect in the graphene based temperature sensor using both experimental and simulation results.

CHAPTER 5

PSC POWER SOURCE FOR SENSORS

5.1 Flexible Solar cells

The objective of this research is to develop high-efficiency flexible perovskite solar cells using roll-to-roll manufacturing. This report includes the preparation of the materials and fabrication of flexible perovskite solar cells. Also, we characterize the surface morphology of the perovskite to check the grain size by atomic force microscopy (AFM) and scanning electron microscopy (SEM). The efficiency of solar cells is measured by the solar simulator. The relationship between efficiency and grain size is also included in the report. The flexible solar cells show the power conversion efficiency (7.6 %) under the AM 1.5 G.

5.1.1 Introduction

Solar energy is one of the crucial renewable energy resources. Since it is clean and independent, it can be applied to several applications such as solar cell and solar thermal energy. Solar cells can directly produce electricity from photon and it does not cause any problem to our environment as well. As big companies recently start to commercialize foldable devices, the flexible solar cell is also attracted by researchers. Especially, several research groups have been focused on perovskite solar cells because of low-cost fabrication, low fabrication temperature and high efficiency. Perovskite can also be

synthesized on the flexible substrate. Therefore, growing perovskite on a flexible substrate is an important research topic.

Traditionally, the perovskite solar cells have a planar structure that consists of an electron transport layer (ETL), perovskite and hole transport layer (HTL) for the higher efficiency. However, it is not easy to apply the planar structure with traditional materials for flexible solar cells. Since high-temperature processes cannot apply to the flexible substrate, the materials need to be exchanged. For instance, conventional ETL (TiO_2) needs 550 °C temperature for the sintering process [160]. Therefore it is not appropriate material for flexible substrate. Another reason is the transmittance of the material. Spiro is used as HTL in the planar structure but does not have high transmittance. For this reason, spiro cannot be used below the perovskite layer [161].

To fabricate the flexible solar cells, we chose the inverted planar structure which has HTL/perovskite/ETL structure [162]. Poly(3,4-ethylenedioxythiophene) polystyrene sulfonate (PEDOT:PSS) can be used as an hole transport layer for hole extraction in perovskite solar cells because of its high transmittance and conductivity. Phenyl-C61-butyric acid methyl ester (PCBM) is substituted with TiO_2 for ETL. As a result, the maximum fabrication temperature is decreased to 115 °C which is much lower than the traditional fabrication temperature (550 °C). This report includes how to prepare the materials, how to fabricate the device, the analysis of the synthesized material and the efficiency of the devices.

5.1.2 Device structure and the fabrication procedures

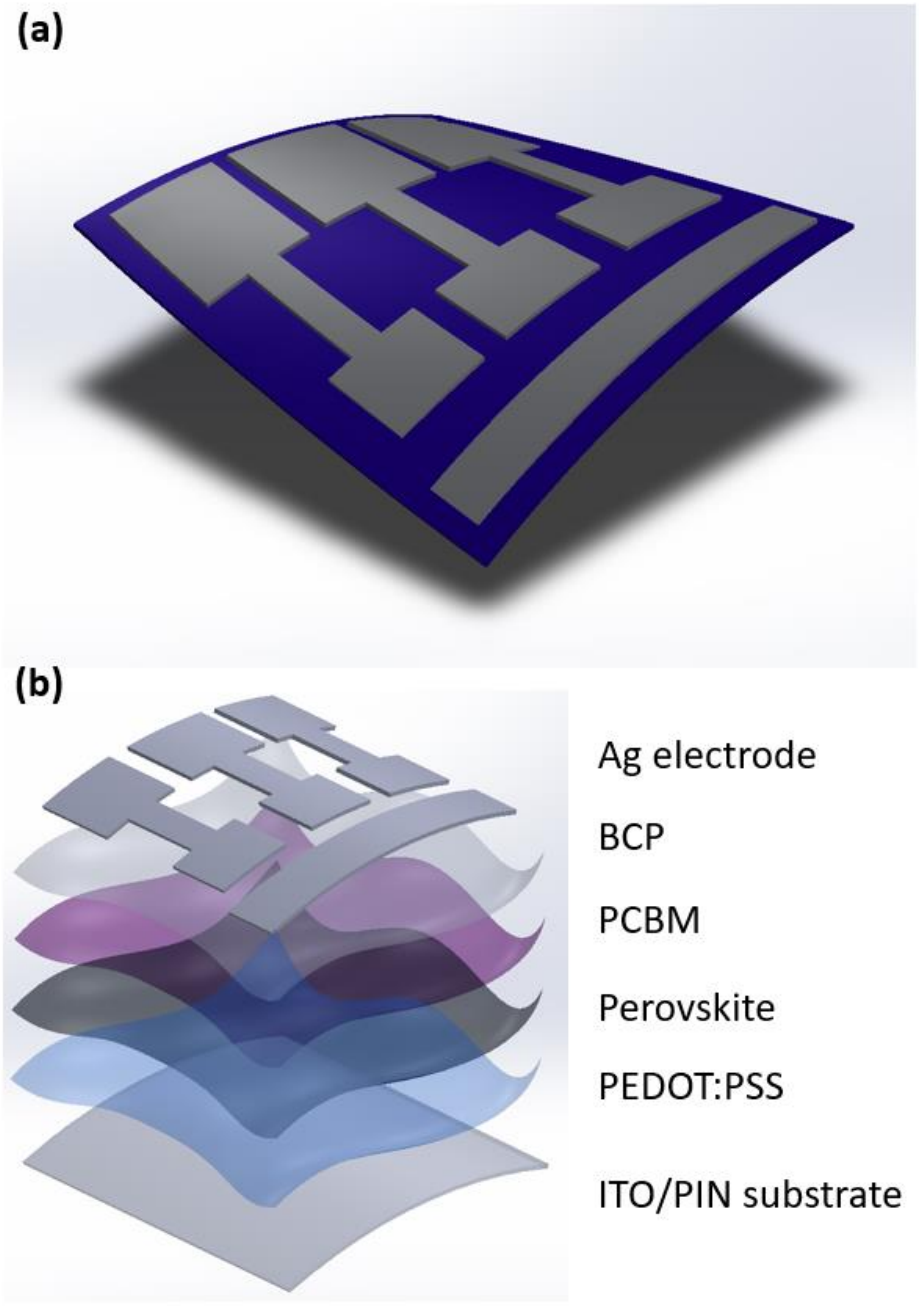

Figure 5.1 (a) Fabricated flexible perovskite solar cells (b) Device structure of the solar cells.

Figure 5.1 (a) shows the fabricated flexible solar cells. Each device has three test areas (3 x 3 mm^2). The device is fabricated on the flexible substrate. The ITO is deposited on the PEN substrate for the transparent electrode. Since the ITO/PEN film has high transparency, low moisture permeability, high thermo-stability and high chemical stability, we chose these materials as a substrate. The sheet resistance of ITO/PEN is less than 15 ohm/sq which is similar to ITO glass. The ITO needs to be patterned by a wet etching method. Zinc powder spreads on the area that needs to be etched and ITO can be etched by dropping hydrogen chloride solution on the powder.

Figure 5.1 (b) describes the structure of the devices. The device consists of several layers between the top and bottom electrodes including PEDOT:PSS, Perovskite, PCBM and BCP.

PEDOT:PSS is a transparent conductive polymer which consists of the ionomers poly(3,4-ethylenedioxythiophene) and polystyrene sulfonate. Due to its distinctive combination of conductivity and transparency, PEDOT:PSS can be used as a layer in organic electronic devices such as organic light-emitting diode (OLED) and organic solar cell (OSC). Before coating PEDOT:PSS solution, the ITO/PEN substrate needs to be treated by oxygen plasma to enhance the surface energy. Then PEDOT:PSS is coated on the patterned ITO/PEN substrate using spin-coater (8000 rpm for 40 s). The substrate needs to be post-annealed with 120 °C for 20 min. For the perovskite film, the PbI_2 solution is first coated on the PEDOT:PSS/ITO/PEN substrate. Then the PbI_2 film changed to perovskite through the CVD process. PbI_2 solution is prepared by dissolving

the PbI_2 powder into the (DMF:DMSO=95:5) solvent and coats on the substrate (2500 rpm for 60 s). During the CVD process, the samples are located on the quartz boat with mixed powder which the formanidinium iodide (0.95 g) and Methylammonium Bromide (0.05 g). The temperature is increased from room temperature to 115 °C for 1 h and maintained at 115 °C for 7 h. The CVD process time increase to 10 h which includes 2 h ramping time to get a larger grain size. PCBM is a well-known electron acceptor material because of its exceptional conductivity and electron accept capability. The PCBM solution is prepared by dissolving the PCBM powder (23 mg) into chlorobenzene (1 ml). The coating condition is 2500 rpm for 40 s. For the next layer, BCP powder (0.5 mg) disperses into IPA (1 ml). Then the BCP solution coated on the PCBM layer (4000 rpm for 20 s). This BCP layer can change the Schottky contact to the ohmic contact between PCBM and Ag. It can reduce the recombination rate by improving the quality of interfacial contact. As the last layer, Ag (120 nm) is deposited for the top electrode by the thermal evaporator.

5.1.3 Surface structure of the perovskite film

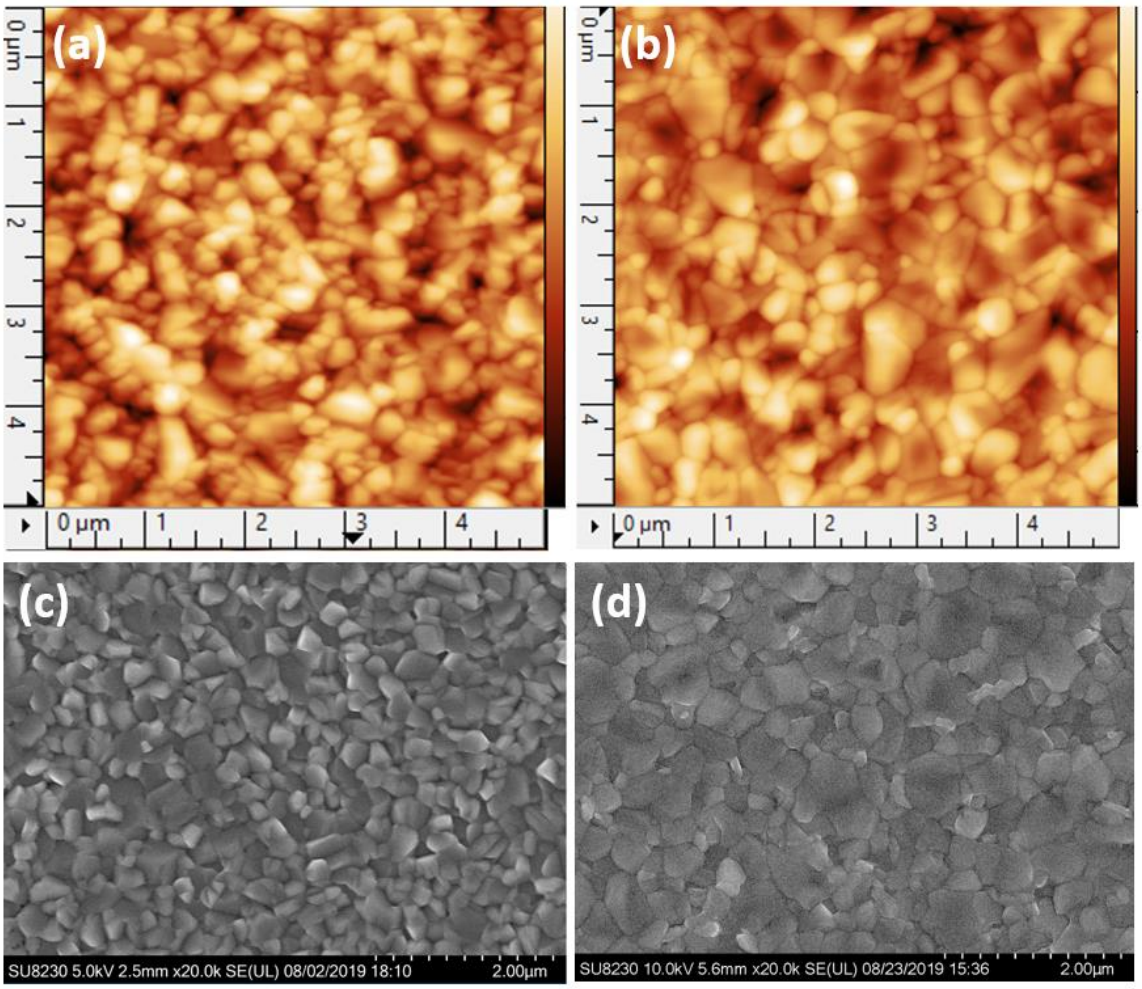

Figure 5.2 (a) AFM image of perovskite film after CVD process for 8 h (b) AFM image for 10 h CVD (c) SEM image of perovskite film for 8 h (d) SEM image for 10 h CVD.

As a part of the research, the duration time is controlled during the CVD process. The duration includes the ramping time. This means that the 10 h fabrication process takes a longer time to reach the target temperature (115 °C). We got a different perovskite film depending on the ramp of the temperature. The surface morphology is characterized by

AFM (Asylum Research) and SEM (Hitachi S4700). Figure 5.2 (a) depicts the surface morphology of perovskite film after the CVD process for 8 h. The grains are clearly shown in the image. The grain size is about 200~300 nm and the roughness of the surface (R_q) is 23.62 nm. Figure 5.2 (c) is the SEM image of the perovskite film. We confirm the surface shape by comparing both AFM and SEM images. Both images show a similar morphology. Figure 5.2 (b) and (d) demonstrate the morphology of the perovskite after the 10 h CVD process. In this case, while the grain size varies from 0.1 to 1 μm, we got a much larger grain size than the 8 h process. The roughness of the surface (R_q) is 28.51 nm, and the overall film quality is uniform. The grains are also shown in figure 5.2 (d). In this experiment, it is shown that the grain size is related to the ramping time. The relationship needs to be studied more in the next research period to optimize the growing condition.

5.1.4 Performance of the perovskite solar cells

Figure 5.3 (a) represents the energy band diagram of a perovskite solar cell including the work function of the electrodes and HOMO/LUMO of the semiconductors. PEDOT:PSS and PCBM are used as HTL and ETL, respectively. These layers help to enhance the performance of the device by increasing open circuit voltage and short circuit current. PEDOT:PSS has a HOMO energy level at -5.2 eV, which can help the hole's flow from perovskite to ITO. However, the large bandgap of PEDOT:PSS can effectively block the electrons from perovskite. The PCBM layer also has a similar function.

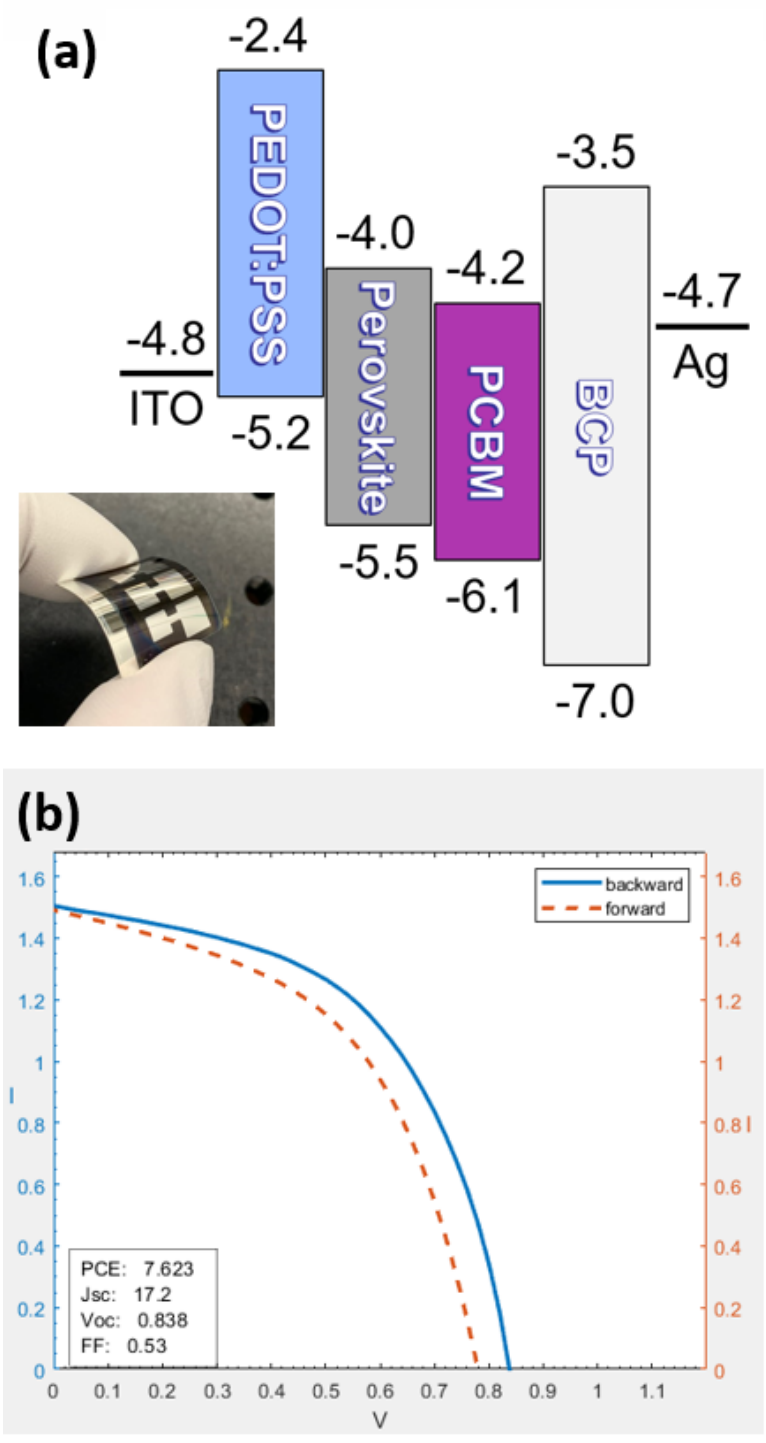

Figure 5.3 (a) Energy band diagram of the solar cell and the real device picture (b) IV curve of the flexible perovskite solar cell.

It accepts electrons but blocks holes. As shown in the energy band diagram, BCP has a wide bandgap and an electron affinity. This buffer layer also acts as a hole blocking barrier but an electron transporting layer. Since the BCP layer can also remove the Schottky barrier between PCBM and Ag, it is widely used for one of the layers in organic electronics such as an OLED and OSC including perovskite solar cells. The inset image shows the fabricated flexible perovskite solar cell.

Figure 5.3 (b) shows the IV curve of the solar cell. The power conversion efficiency (PCE) is 7.6 % under AM 1.5 G. In the next phase of the project, the current and voltage could be increased by optimizing the layers in the device so that we get the best performance of the devices. The fill factor (FF) also can be increased up to 0.8. In this report, we successfully demonstrate the feasibility of the solution based fabrication as the first step for roll-to-roll manufacturing system.

5.1.5 Conclusion

The flexible perovskite solar cells are fabricated on the PEN substrate. The perovskite films grew by the CVD process for 8 h and 10 h. The grown perovskite film is characterized by AFM and SEM. The larger gains grew for the longer ramping time because of the growing speed of the perovskite seed. We successfully fabricated the perovskite solar cells with all solution-based fabrication and confirmed that these materials could be applied to the roll-to-roll manufacturing process. The highest PCE that we have gotten is 7.6 % with those materials. Since the efficiency could be enhanced by

the quality of the perovskite, it is necessary to clarify the relationship between the performance and the quality of perovskite. The optimization should be carried out for the roll-to-roll process.

5.2 Hole Transport Layer

The objective of this research is to optimize the process for high-efficiency flexible perovskite solar cells. In this report, we have studied the materials to introduce better hole transport layers (HTL) for the device. PTAA is used as HTL and the results are compared with the device which has PEDOT:PSS as HTL. The report includes the preparation of the materials and fabrication of perovskite solar cells. The surface morphologies of the perovskite were characterized by atomic force microscopy (AFM). The efficiency of solar cells is measured by the solar simulator.

5.2.1 Introduction

Traditionally, the perovskite solar cells consist of an electron transport layer (ETL), perovskite, hole transport layer (HTL) and electrode. Especially, the poly(3,4-ethylenedioxythiophene)poly-(styrenesulfonate) PEDOT:PSS (AI4083) was used as HTL for flexible perovskite solar cells because of its transparency, work function and bandgap [163]. However, AI4083 has a highly acidic nature that can degrade the electrical property of indium tin oxide (ITO) and can be easily oxidized by water vapor and oxygen present in the air [164]. Therefore, it is necessary to substitute AI4083 with stable

material. One of the candidates is Poly[bis(4-phenyl)(2,4,6-trimethylphenyl)amine] (PTAA) because of its hydrophobicity and stability.

When we compare the contact angle of PTAA with AI4083, the contact angle on PTAA was larger than that on AI 4083, indicating the hydrophobicity of PTAA. Previous studies verified that hydrophobic bottom layers helped the crystal growth of perovskite by isolating perovskite nuclei from each other [165]. Since the grain boundary growth rate of the perovskite on PTAA is higher than on AI 4083, we can expect the larger grain size on PTAA. Thus, using PTAA is more helpful for increasing the upper perovskite grains than using AI 4083. The XRD results show increased peaks for perovskite, indicating the enhanced crystallinity of the perovskite on PTAA compared to that on AI 4083, which is consistent with previous studies. Large grain sizes benefit the transfer of excitons in the perovskite film, thus reducing the probability of exciton quenching at grain boundaries and thereby improving photovoltaic performance. The branched-chain of PTAA can also fill the vacancy of the methylammonium ion formed in the annealing process which improved the stability of the perovskite and suppressed charge recombination at the interfaces.

5.2.2 Device structure and the fabrication procedures

Figure 5.4 shows the structure of solar cells and the energy band diagram of solar cells with (a) AI4083 and (b) PTAA. AI4083 and PTAA are used for HTL for the devices.

Both layers help to enhance the performance of the device by helping the holes flow between the perovskite and ITO and by blocking the electrons from perovskite.

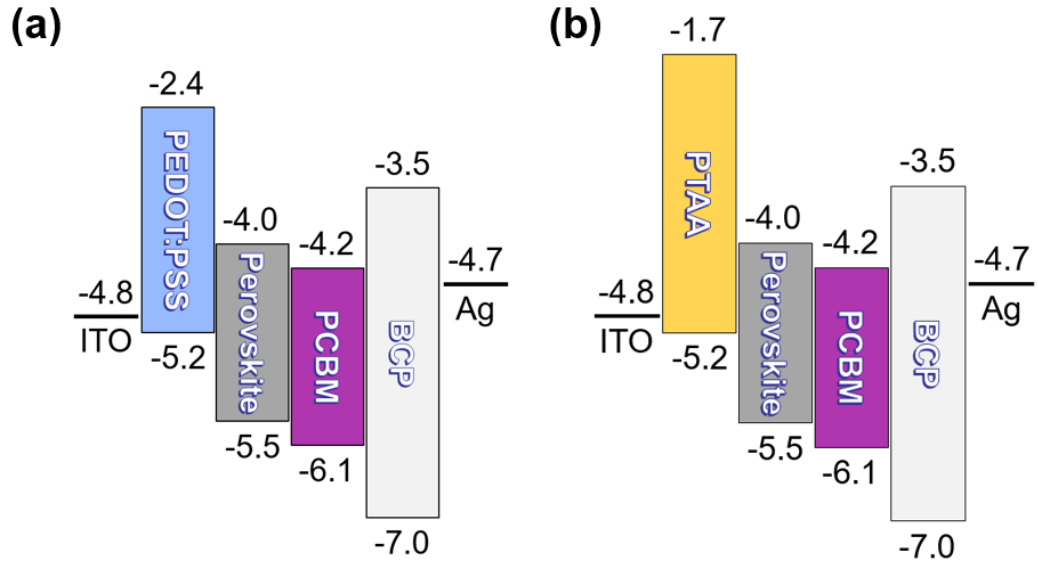

Figure 5.4 Energy band diagram of the solar cell with (a) AI4083 and (b) PTAA.

AI4083 and PTAA have the same HOMO energy level at -5.2 eV which can help the hole's flow from perovskite to ITO. However, the larger bandgap of PTAA can more effectively block the electrons than AI4083.

The PTAA solution was prepared by dissolving the PTAA powder into the toluene (10 mg/ml). After the prepared solution was coated on ITO/PEN substrate by spin-coating (4000 rpm for 40 s), the substrates need to be dried on a hot plate 100 ℃ for 10 min. Next, the PbI_2 solution was coated on the AI4083/ITO/PEN and PTAA/ITO/PEN substrates. Then the PbI_2 film changed to perovskite through the CVD process with MABr and FAI mixed powder. The ratio is 95:5 or 95 % FAI by weight and 5% MABr

by weight. The temperature is increased from room temperature to 115 ℃ for 1 h and maintained at 115 ℃ for 7 h. The CVD process time was increased to 10 h which includes 2 h ramping time to get a larger grain size. The PCBM solution is prepared by dissolving the PCBM powder (23 mg) into chlorobenzene (1 ml). The coating condition is 2500 rpm for 40 s. For the next layer, BCP powder (0.5 mg) disperses into IPA (1 ml). Then the BCP solution coated on the PCBM layer (4000 rpm for 20 s). As the last layer, Ag (120 nm) is deposited for the top electrode by the thermal evaporator.

5.2.3 Grain size of the perovskite film

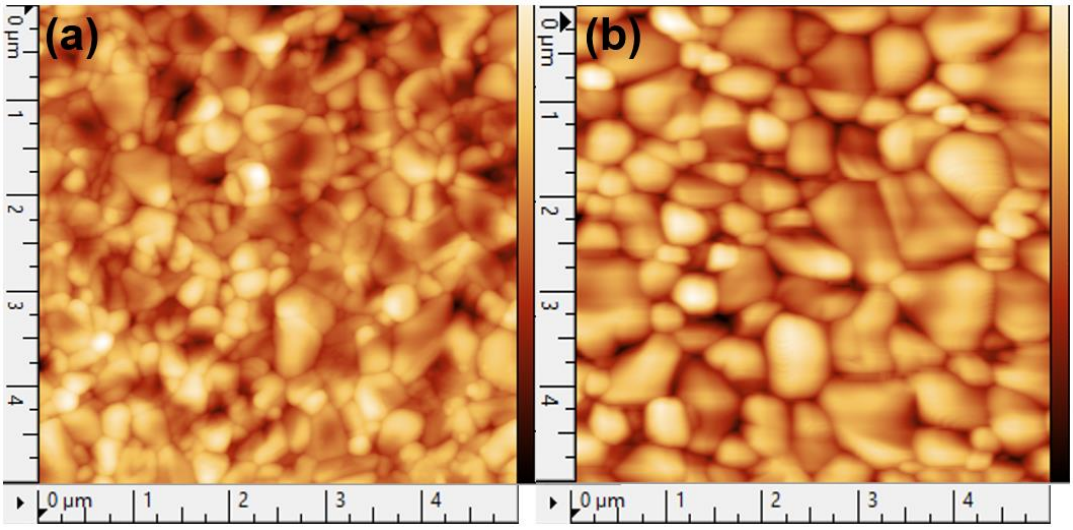

Figure 5.5 AFM image of perovskite film on (a) AI4083 and on (b) PTAA.

Figure 5.5 shows the surface morphology of the perovskite film. Both perovskite films were synthesized by the same CVD process. The only difference is the HTL below the PbI_2. The results demonstrate that the perovskite on PTAA has a much larger grain size

than the perovskite on AI4083 because the perovskite nuclei are isolated by the hydrophobic PTAA film. The larger grain size of perovskite causes less recombination and efficient hole transfer. As a result, we can expect better device performance with the PTAA layer.

5.2.3 Performance of the perovskite solar cells

Figure 5.6 shows the IV curve of the solar cell with (a) AI4083 and (b) PTAA. The power conversion efficiency (PCE) is 7.6 % with AI4083. The PCE of the device with PTAA is 6.4 %. Although the device did not show the enhanced PCE with PTAA, the open-circuit voltage is increased because of the large grains. As decreasing the recombination with the large grains, we can expect the larger V_{oc}. In the research, we confirm that the grain of perovskite can be increased by the PTAA layer and PTAA can be a great candidate for HTL in perovskite solar cells.

5.2.4 Conclusion

The perovskite solar cells are fabricated with different HTL materials such as AI4083 and PTAA. The perovskite films grew by the CVD process for 10 h on different HTL films and the grown perovskite film is characterized by AFM. We have confirmed that the hydrophobic surface of PTAA makes the larger grain size of perovskite by isolating PbI_2 nuclei from each other and expected better device performance with larger grain size. However, the device with AI4083 shows better PEC than the device with PTAA in the research. We believe that it is not because of the perovskite layer and the device will show better results by optimizing the process.

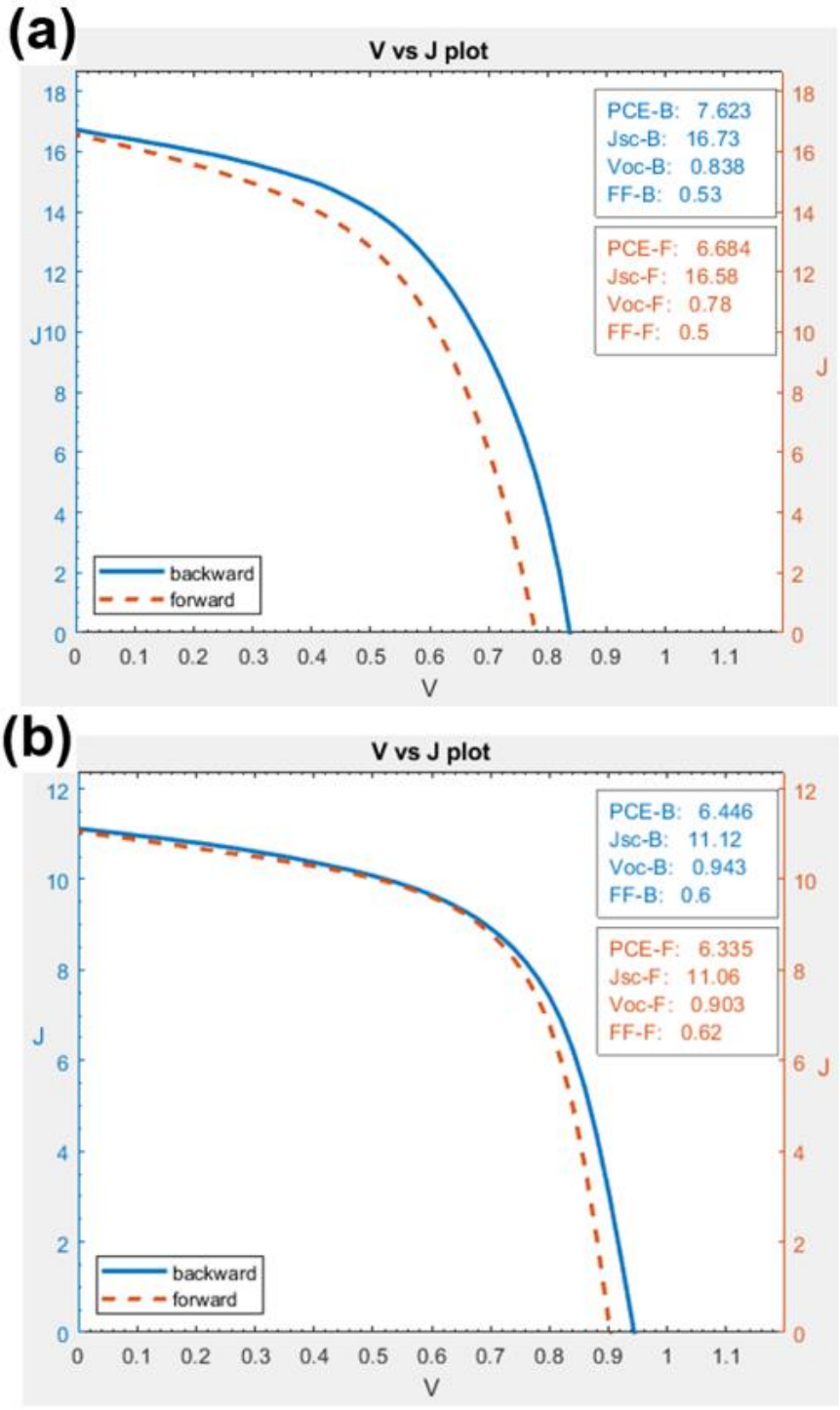

Figure 5.6 IV curve of the perovskite solar cell with (a) AI4083 and (b) PTAA.

CHAPTER 6

CONCLUSIONS

6.1 Summaries

The research aims to develop a graphene based sensors which can detect the ions in water, and to fabricate the perovskite solar cells as a power source of the sensors. For sensing the ions in water, current equipment is expensive and large. It also needs complex and time-consuming processes for the measurement. To solve the problems, the graphene based IS-FET was suggested in the research. The devices were designed and fabricated using MEMS technology. The fabricated sensors are much smaller, cheaper, and simpler than current technologies such as colorimetry and ion exchange electrode. The IS-FET sensors were characterized by a semiconductor analyzer to assess the performance of the sensors including sensitivity, selectivity, and response time. The target ions are nitrate, phosphate, chloride, and mercury.

Chapter 2 is about the synthesis and transfer of graphene. Graphene was synthesized by the CVD process using several gases including CH_4, H_2, and Ar at high temperatures. The quality of graphene is analyzed by Raman spectroscopy to check the thickness and uniformity of graphene film. Graphene was successfully synthesized through an optimized process. The next topic was the transfer process of graphene to the target substrates. Two different methods were investigated for the graphene transfer. First, PMMA was used in the process, and a single layer of graphene was successfully transferred. Second, thermal release tape is used for the transfer. Although it was hard to

get a perfect graphene film with the thermal release tape, it is much easy to handle the graphene. Therefore, the thermal release tape method has been frequently used in this research work. For the sensor design, two types of sensors were fabricated for the experiment. The first type of sensor is designed for measuring the resistance change of graphene depending on the concentration of solutions. Since the graphene is exposed to the solutions with an applied voltage which can oxidize or reduce graphene, it is hard to get a stable signal from the devices. The phenomena were confirmed by Raman spectroscopy. Another type of sensor was designed and fabricated to solve the oxidation and reduction problems during the test. As a result, the graphene based IS-FET was used for the experiment. Since the IS-FET devices don't need to use a high voltage for the measurement, the oxidation and reduction problems don't exist during the experiment. In Chapter 3, the importance of selectivity in graphene based IS-FET devices is explained, and the principal of the selective membrane is described. In each small chapter, the four different selective membranes are introduced and synthesized by two different methods using ionophore and MIP. Nitrate, mercury and chloride selective membranes were synthesized with the ionophores, and phosphate selective membrane was synthesized with MIP. The synthesized selective membranes were directly coated on the graphene layer, and the sensors were characterized by a semiconductor analyzer to observe the Dirac point shift as changing the solution concentration. The sensor performance was analyzed based on the collected data. We successfully demonstrated the graphene based IS-FET sensors from the fabrication to the performance in this chapter.

In chapter 4, the fabrication of the porous AAO film has been discussed. First, the aluminum plates were electrically polished in the acidic solution to make the surface smooth. Then the polished substrates were oxidized with an applied voltage in the solution. This process is called anodization. There were two anodization steps in the fabrication because it is hard to get the uniform porous structures in the first anodization process. After the first anodization process, the fabricated oxide layer was removed by the oxide etchant to get the uniform dents under the oxide layer. In the second anodization process, the oxide layer starts to grow from the dents to form a more uniform structure. The fabricated porous structures were characterized by SEM. The AAO films were used for applications such as temperature and nitrate sensors. As follow-up research, the graphene based IS-FET was fabricated on the AAO substrate for nitrate detection. We observed the better performance of the sensor in terms of sensitivity and response time compared to the Si based sensors. Another application is about graphene based temperature sensor using an AAO substrate. For the research, graphene was transferred to the AAO substrate with gold electrodes, and the resistance change of the graphene was recorded depending on the temperature. The data from the AAO substrate was compared with the result from a glass substrate. We verified that the graphene based temperature sensor on the AAO substrate has higher sensitivity and faster response time than the sensor in the glass substate. The COMSOL simulation data also supported the experiment result.

In chapter 5, the fabrication of high efficiency perovskite solar cells has been discussed. The working principle and the structure of the perovskite solar cells are introduced. The perovskite layer in solar cells was synthesized by the CVD process. The synthesized layers were characterized by AFM and SEM. The temperature and process time were controlled to get a large grain size of perovskite. After optimizing the process, the glass substrate was changed to the PEN substrate for the flexible solar cells. The structure of the solar cell was also changed from planar to inverted structure because of the material limitations. Although the fabricated flexible solar cells showed lower performance than the conventional structured devices, it is still worthy of an investigation due to its simple, cheap, and fast fabrication process.

6.2 Conclusions

In the research, the graphene based sensors were investigated to detect the specific ions in water including phosphate, nitrate, chloride, and mercury. For the sensing material, the graphene was synthesized by the CVD process, and characterized by Raman spectroscopy. Then the selective membranes were synthesized with ionophore and MIP for the selectivity of the sensors.

First, the ion sensors are prepared and tested with several solutions such as nitrate, sulfate, phosphate, and chloride. In the experiment, the detection limit of sensors was 0.82, 0.87, and 0.26 mg/L for nitrate, chloride and phosphate, respectively. And the response time was about 10 s. In terms of the mercury, the lowest detected concentration

was 1.125 µg/L. For the selectivity test, the sensors are exposed to the solutions which are nitrate, sulfate, phosphate, and chloride. Each sensor only shows a response to the solution matched with its own selective membrane. As continuous research, the graphene based sensor was fabricated on the AAO substrate with uniform porous structures. The structure of AAO makes the sensor more sensitive and faster. In nitrate detection, the detection limit was decreased to 0.32 mg/L, and the response time was 3 s. The AAO substrate was also applied to the temperature sensor. The resistance change of graphene in the AAO substrate was larger and faster than the glass substrate. The average TCR values were -12.4×10^{-4} $^{\circ}C^{-1}$ and -24.1×10^{-4} $^{\circ}C^{-1}$ for the Glass and AAO substrate, respectively. The COMSOL simulation result also shows shorter response time on the AAO substrate.

As a power source for the sensor system, the perovskite solar cells were designed and fabricated. There were two different solar cells with planar and inverted structures. For the planar structure, the device was fabricated on the glass substrate, and the efficiency was about 17 %. Since the inverted structure was planned for the flexible device, PEN was used as the substrate. The best efficiency of the flexible device was 7.6 %.

6.3 Future Recommendations

In the research, CVD graphene was used for the sensing material in the sensor. Although graphene has shown a great response to the target materials, many 2D materials and nanoparticles can be used in the sensor. For example, there have been many studies about

2D semiconductive materials including phosphorene, WSe, MoS_2, etc. There are also famous semiconductive nanoparticles such as ZnO, CdS, CdSe, etc. These materials could be used as a substitute instead of the graphene layer in the device. Therefore, the first available approach for extended research is finding the proper sensing materials which can enhance the sensor performance.

Changing the sensor structure could be another topic of the research. As shown in the research, sensor performance can be enhanced by changing the substrate. Since the performance is closely related to the sensor structure, Changing the sensor structure is a good topic for future research. Each sensor could also be assembled by changing the sensor structure to form the sensor array which can detect several ions at the same time.

Next, several materials have been used for the fabrication of the perovskite solar cells including organic and inorganic materials. There is much ongoing research to find the best material for perovskite solar cells. Therefore, finding the best combination of materials is a critical topic in perovskite solar cells. Since each layer also needs to be fabricated with the optimized process, investigating the optimized condition could enhance the device performance.

Lastly, the sensor part and the power source part were separately designed and fabricated in this research. Therefore, the perovskite solar cells could be assembled with sensors for the self-powered sensing system as future work.

References

[1] F. Chai, C. Wang, T. Wang, L. Li, Z. Su, Colorimetric detection of Pb2+ using glutathione functionalized gold nanoparticles, ACS Appl. Mater. Interfaces. 2 (2010) 1466–1470. doi:10.1021/am100107k.

[2] R. De Marco, G. Clarke, B. Pejcic, Ion-selective electrode potentiometry in environmental analysis, Electroanalysis. 19 (2007) 1987–2001. doi:10.1002/elan.200703916.

[3] A.K. Geim, K.S. Novoselov, The rise of graphene, Nat Mater. 6 (2007) 183–191. http://dx.doi.org/10.1038/nmat1849.

[4] A. Zurutuza, C. Marinelli, Challenges and opportunities in graphene commercialization, Nat. Nanotechnol. 9 (2014) 730–734. doi:10.1038/nnano.2014.225.

[5] R. Wang, X.G. Ren, Z. Yan, L.J. Jiang, W.E.I. Sha, G.C. Shan, Graphene based functional devices: A short review, Front. Phys. 14 (2019) 9–18. doi:10.1007/s11467-018-0859-y.

[6] Y. Sun, Q. Wu, G. Shi, Graphene based new energy materials, Energy Environ. Sci. 4 (2011) 1113–1132. doi:10.1039/c0ee00683a.

[7] J.S. Qi, J.Y. Huang, J. Feng, D.N. Shi, J. Li, The possibility of chemically inert, graphene-based all-carbon electronic devices with 0.8 eV gap, ACS Nano. 5 (2011) 3475–3482. doi:10.1021/nn102322s.

[8] M. Zhang, Y. Wang, L. Huang, Z. Xu, C. Li, G. Shi, Multifunctional Pristine Chemically Modified Graphene Films as Strong as Stainless Steel, Adv. Mater. 27 (2015) 6708–6713. doi:10.1002/adma.201503045.

[9] D. Akinwande, C.J. Brennan, J.S. Bunch, P. Egberts, J.R. Felts, H. Gao, R. Huang, J.S. Kim, T. Li, Y. Li, K.M. Liechti, N. Lu, H.S. Park, E.J. Reed, P. Wang, B.I. Yakobson, T. Zhang, Y.W. Zhang, Y. Zhou, Y. Zhu, A review on mechanics and mechanical properties of 2D materials—Graphene and beyond, Extrem. Mech. Lett. 13 (2017) 42–77. doi:10.1016/j.eml.2017.01.008.

[10] K. Yang, L. Feng, X. Shi, Z. Liu, Nano-graphene in biomedicine: Theranostic applications, Chem. Soc. Rev. 42 (2013) 530–547. doi:10.1039/c2cs35342c.

[11] J. Renteria, D. Nika, A. Balandin, Graphene Thermal Properties: Applications in Thermal Management and Energy Storage, Appl. Sci. 4 (2014) 525–547. doi:10.3390/app4040525.

[12] M.S. Cao, X.X. Wang, W.Q. Cao, J. Yuan, Ultrathin graphene: electrical properties and highly efficient electromagnetic interference shielding, J. Mater. Chem. C. 3 (2015) 6589–6599. doi:10.1039/c5tc01354b.

[13] H. Chang, H. Wu, Graphene-based nanomaterials: Synthesis, properties, and optical and optoelectronic applications, Adv. Funct. Mater. 23 (2013) 1984–1997. doi:10.1002/adfm.201202460.

[14] M. Gmitra, S. Konschuh, C. Ertler, C. Ambrosch-Draxl, J. Fabian, Band-structure topologies of graphene: Spin-orbit coupling effects from first principles, Phys. Rev. B - Condens. Matter Mater. Phys. 80 (2009) 1–5. doi:10.1103/PhysRevB.80.235431.

[15] W. Choi, I. Lahiri, R. Seelaboyina, Y.S. Kang, Synthesis of graphene and its applications: A review, Crit. Rev. Solid State Mater. Sci. 35 (2010) 52–71. doi:10.1080/10408430903505036.
[16] H. Liu, Y. Liu, D. Zhu, Chemical doping of graphene, J. Mater. Chem. 21 (2011) 3335–3345. doi:10.1039/c0jm02922j.
[17] A.T. Murdock, A. Koos, T. Ben Britton, L. Houben, T. Batten, T. Zhang, A.J. Wilkinson, R.E. Dunin-Borkowski, C.E. Lekka, N. Grobert, Controlling the orientation, edge geometry, and thickness of chemical vapor deposition graphene, ACS Nano. 7 (2013) 1351–1359. doi:10.1021/nn3049297.
[18] X. Liang, B.A. Sperling, I. Calizo, G. Cheng, C.A. Hacker, Q. Zhang, Y. Obeng, K. Yan, H. Peng, Q. Li, X. Zhu, H. Yuan, A.R. Hight Walker, Z. Liu, L.M. Peng, C.A. Richter, Toward clean and crackless transfer of graphene, ACS Nano. 5 (2011) 9144–9153. doi:10.1021/nn203377t.
[19] J.D. Caldwell, T.J. Anderson, J.C. Culbertson, G.G. Jernigan, K.D. Hobart, F.J. Kub, M.J. Tadjer, J.L. Tedesco, J.K. Hite, M.A. Mastro, R.L. Myers-Ward, C.R. Eddy, P.M. Campbell, D.K. Gaskill, Technique for the Dry Transfer of Epitaxial Graphene onto Arbitrary Substrates, ACS Nano. 4 (2010) 1108–1114. doi:10.1021/nn901585p.
[20] R.C. Rollings, A.T. Kuan, J.A. Golovchenko, Ion selectivity of graphene nanopores, Nat. Commun. 7 (2016). doi:10.1038/ncomms11408.
[21] R.D. Johnson, L.G. Bachas, Ionophore-based ion-selective potentiometric and optical sensors, Anal. Bioanal. Chem. 376 (2003) 328–341. doi:10.1007/s00216-003-1931-0.
[22] J.J. Belbruno, Molecularly Imprinted Polymers, Chem. Rev. 119 (2019) 94–119. doi:10.1021/acs.chemrev.8b00171.
[23] S. Sharma, K.K. Jain, A. Sharma, Solar Cells: In Research and Applications—A Review, Mater. Sci. Appl. 06 (2015) 1145–1155. doi:10.4236/msa.2015.612113.
[24] M. V. Kovalenko, L. Protesescu, M.I. Bodnarchuk, Properties and potential optoelectronic applications of lead halide perovskite nanocrystals, Science (80-.). 358 (2017) 745–750. doi:10.1126/science.aam7093.
[25] M.A. Green, A. Ho-Baillie, H.J. Snaith, The emergence of perovskite solar cells, Nat. Photonics. 8 (2014) 506–514. doi:10.1038/nphoton.2014.134.
[26] Y. Peng, G. Jing, T. Cui, High-performance perovskite solar cells fabricated by vapor deposition with optimized PbI2 precursor films, RSC Adv. 5 (2015) 95847–95853. doi:10.1039/c5ra19343e.
[27] G. Wu, Z. Dai, X. Tang, Z. Lin, P.K. Lo, M. Meyyappan, K.W.C. Lai, Graphene Field-Effect Transistors for the Sensitive and Selective Detection of Escherichia coli Using Pyrene-Tagged DNA Aptamer, Adv. Healthc. Mater. 6 (2017) 1–9. doi:10.1002/adhm.201700736.
[28] B. Zhan, C. Li, J. Yang, G. Jenkins, W. Huang, X. Dong, Graphene Field-Effect Transistor and Its Application for Electronic Sensing, Small. 10 (2014) 4042–4065. doi:10.1002/smll.201400463.

[29] M. Gautam, A.H. Jayatissa, Graphene based field effect transistor for the detection of ammonia, J. Appl. Phys. 112 (2012). doi:10.1063/1.4752272.
[30] W. Zhu, V. Perebeinos, M. Freitag, P. Avouris, Carrier scattering, mobilities, and electrostatic potential in monolayer, bilayer, and trilayer graphene, Phys. Rev. B - Condens. Matter Mater. Phys. 80 (2009) 1–8. doi:10.1103/PhysRevB.80.235402.
[31] W.E. Morf, E. Lindner, W. Simon, Theoretical Treatment of the Dynamic Response of Ion-Selective Membrane Electrodes, Anal. Chem. 47 (1975) 1596–1601. doi:10.1021/ac60359a002.
[32] Y. Jin, B. Hu, Z. Wei, Z. Luo, D. Wei, Y. Xi, Y. Zhang, Y. Liu, Roles of H2in annealing and growth times of graphene CVD synthesis over copper foil, J. Mater. Chem. A. 2 (2014) 16208–16216. doi:10.1039/c4ta02557a.
[33] M. Losurdo, M.M. Giangregorio, P. Capezzuto, G. Bruno, Graphene CVD growth on copper and nickel: Role of hydrogen in kinetics and structure, Phys. Chem. Chem. Phys. 13 (2011) 20836–20843. doi:10.1039/c1cp22347j.
[34] A.B. Loginov, I. V. Bozhev, S.N. Bokova-Sirosh, E.D. Obraztsova, R.R. Ismagilov, B.A. Loginov, A.N. Obraztsov, Few-layer graphene formation by carbon deposition on polycrystalline Ni surface, Appl. Surf. Sci. 494 (2019) 1030–1035. doi:10.1016/j.apsusc.2019.07.254.
[35] M. Chen, R.C. Haddon, R. Yan, E. Bekyarova, Advances in transferring chemical vapour deposition graphene: A review, Mater. Horizons. 4 (2017) 1054–1063. doi:10.1039/c7mh00485k.
[36] W. Liu, H. Li, C. Xu, Y. Khatami, K. Banerjee, Synthesis of high-quality monolayer and bilayer graphene on copper using chemical vapor deposition, Carbon N. Y. 49 (2011) 4122–4130. doi:10.1016/j.carbon.2011.05.047.
[37] S.D. Costa, A. Righi, C. Fantini, Y. Hao, C. Magnuson, L. Colombo, R.S. Ruoff, M.A. Pimenta, Resonant Raman spectroscopy of graphene grown on copper substrates, Solid State Commun. 152 (2012) 1317–1320. doi:10.1016/j.ssc.2012.05.001.
[38] X. Ling, J. Wu, L. Xie, J. Zhang, Graphene-thickness-dependent graphene-enhanced Raman scattering, J. Phys. Chem. C. 117 (2013) 2369–2376. doi:10.1021/jp310564d.
[39] L.G. Cançado, A. Jorio, E.H.M. Ferreira, F. Stavale, C.A. Achete, R.B. Capaz, M.V.O. Moutinho, A. Lombardo, T.S. Kulmala, A.C. Ferrari, Quantifying defects in graphene via Raman spectroscopy at different excitation energies, Nano Lett. 11 (2011) 3190–3196. doi:10.1021/nl201432g.
[40] H. Kato, N. Itagaki, H.J. Im, Growth and Raman spectroscopy of thickness-controlled rotationally faulted multilayer graphene, Carbon N. Y. 141 (2019) 76–82. doi:10.1016/j.carbon.2018.09.017.
[41] Y.Y. Wang, R.X. Gao, Z.H. Ni, H. He, S.P. Guo, H.P. Yang, C.X. Cong, T. Yu, Thickness identification of two-dimensional materials by optical imaging, Nanotechnology. 23 (2012). doi:10.1088/0957-4484/23/49/495713.
[42] P.K. Ang, W. Chen, A.T.S. Wee, P.L. Kian, Solution-gated epitaxial graphene as pH sensor, J. Am. Chem. Soc. 130 (2008) 14392–14393. doi:10.1021/ja805090z.

[43] S.S. Kwon, J. Yi, W.W. Lee, J.H. Shin, S.H. Kim, S.H. Cho, S. Nam, W. Il Park, Reversible and Irreversible Responses of Defect-Engineered Graphene-Based Electrolyte-Gated pH Sensors, ACS Appl. Mater. Interfaces. 8 (2016) 834–839. doi:10.1021/acsami.5b10183.
[44] S. Pei, Q. Wei, K. Huang, H.M. Cheng, W. Ren, Green synthesis of graphene oxide by seconds timescale water electrolytic oxidation, Nat. Commun. 9 (2018) 1–9. doi:10.1038/s41467-017-02479-z.
[45] A.T. Smith, A.M. LaChance, S. Zeng, B. Liu, L. Sun, Synthesis, properties, and applications of graphene oxide/reduced graphene oxide and their nanocomposites, Nano Mater. Sci. 1 (2019) 31–47. doi:10.1016/j.nanoms.2019.02.004.
[46] M. Sebilo, B. Mayer, B. Nicolardot, G. Pinay, A. Mariotti, Long-term fate of nitrate fertilizer in agricultural soils, Proc. Natl. Acad. Sci. 110 (2013) 18185–18189. doi:10.1073/pnas.1305372110.
[47] S.L. Halliday, M.L. Wolfe, Assessing ground water pollution potential from nitrogen fertilizer using a geographic information system, Water Resour. Bull. 27 (1991) 237–245. doi: 10.1111/j.1752-1688.1991.tb03128.x.
[48] C.A.M. De Klein, L. Barton, R.R. Sherlock, Z. Li, R.P. Littlejohn, Estimating a nitrous oxide emission factor for animal urine from some New Zealand pastoral soils, Aust. J. Soil Res. 41 (2003) 381–399. doi:10.1071/SR02128.
[49] G.F. McIsaac, M.B. David, G.Z. Gertner, D.A. Goolsby, Eutrophication: Nitrate flux in the Mississippi River, Nature. 414 (2001) 166–167. doi:10.1038/35102672.
[50] L. Knobeloch, B. Salna, A. Hogan, J. Postle, H. Anderson, Blue babies and nitrate-contaminated well water, Environ. Health Perspect. 108 (2000) 675–678. doi:10.1289/ehp.00108675.
[51] W.L. Daniel, M.S. Han, J.S. Lee, C. a. Mirkin, AuNP137-Colorimetric Nitrite and Nitrate detection with gold nanoparticle probes and kinetic end points, J. Am. Chem. Soc. 131 (2009) 6362–6363. doi:10.1021/ja901609k.
[52] X. Wang, S. V Dzyadevych, J.-M. Chovelon, N.J. Renault, L. Chen, S. Xia, J. Zhao, Development of a conductometric nitrate biosensor based on Methyl viologen/Nafion® composite film, Electrochem. Commun. 8 (2006) 201–205. doi:https://doi.org/10.1016/j.elecom.2005.11.006.
[53] P.J. Milham, A.S. Awad, R.E. Paull, J.H. Bull, Analysis of plants, soils and waters for nitrate by using an ion-selective electrode, Analyst. 95 (1970) 751–757. doi:10.1039/an9709500751.
[54] K. Maehashi, Y. Sofue, S. Okamoto, Y. Ohno, K. Inoue, K. Matsumoto, Selective ion sensors based on ionophore-modified graphene field-effect transistors, Sensors Actuators, B Chem. 187 (2013) 45–49. doi:10.1016/j.snb.2012.09.033.
[55] J. Kim, S. Shin, Y.-H. Kim, S.-I. Kim, Electrical Coating Method of Graphene Oxide, J. Nanosci. Nanotechnol. 14 (n.d.) 3658–3660. http://www.ingentaconnect.com/content/asp/jnn/2014/00000014/00000005/art00067.

[56] S. Shin, S. Ganorkar, J. Kim, Y.-H. Kim, Y.T. Kim, S.-I. Kim, Design of Circle Array Pattern for Transparent Nanomesh-Type Electrodes, J. Nanosci. Nanotechnol. 15 (2015) 7640–7644. doi:10.1166/jnn.2015.11179.
[57] J. Kim, S. Ganorkar, Y.H. Kim, S. Il Kim, Graphene oxide hole injection layer for high-efficiency polymer light-emitting diodes by using electrophoretic deposition and electrical reduction, Carbon N. Y. 94 (2015) 633–640. doi:10.1016/j.carbon.2015.07.049.
[58] J. Kwon, J. Kim, Fabrication and properties of pn diodes with hybrid 2D layers: Graphene/MoS2, Mater. Express. 8 (2018) 299–303. doi:10.1166/mex.2018.1430.
[59] X. Miao, S. Tongay, M.K. Petterson, K. Berke, A.G. Rinzler, B.R. Appleton, A.F. Hebard, High Efficiency Graphene Solar Cells by Chemical Doping, Nano Lett. 12 (2012) 2745–2750. doi:10.1021/nl204414u.
[60] I. Meric, M.Y. Han, A.F. Young, B. Ozyilmaz, P. Kim, K.L. Shepard, Current saturation in zero-bandgap, top-gated graphene field-effect transistors, Nat. Nanotechnol. 3 (2008) 654–659. doi:10.1038/nnano.2008.268.
[61] H. Zheng, R.K. Smith, Y. -w. Jun, C. Kisielowski, U. Dahmen, A.P. Alivisatos, Observation of Single Colloidal Platinum Nanocrystal Growth Trajectories, Science (80-.). (2009). doi:10.1126/science.1172104.
[62] X. Li, L. Colombo, R.S. Ruoff, Synthesis of Graphene Films on Copper Foils by Chemical Vapor Deposition, Adv. Mater. 28 (2016) 6247–6252. doi:10.1002/adma.201504760.
[63] S.J. Kim, T. Choi, B. Lee, S. Lee, K. Choi, J.B. Park, J.M. Yoo, Y.S. Choi, J. Ryu, P. Kim, J. Hone, B.H. Hong, Ultraclean patterned transfer of single-layer graphene by recyclable pressure sensitive adhesive films, Nano Lett. 15 (2015) 3236–3240. doi:10.1021/acs.nanolett.5b00440.
[64] H.J. Kim, J.W. Hummel, S.J. Birrell, Evaluation of nitrate and potassium ion-selective membranes for soil macronutrient sensing, Trans. ASABE. 49 (2006) 597–606. doi:10.13031/2013.20476.Rights.
[65] E.H. Hwang, S. Adam, S. Das Sarma, Carrier transport in two-dimensional graphene layers, Phys. Rev. Lett. 98 (2007) 2–5. doi:10.1103/PhysRevLett.98.186806.
[66] F. Schedin, A.K. Geim, S. V. Morozov, E.W. Hill, P. Blake, M.I. Katsnelson, K.S. Novoselov, Detection of individual gas molecules adsorbed on graphene, Nat. Mater. 6 (2007) 652–655. doi:10.1038/nmat1967.
[67] R. Ishimatsu, A. Izadyar, B. Kabagambe, Y. Kim, J. Kim, S. Amemiya, Electrochemical mechanism of ion-ionophore recognition at plasticized polymer membrane/water interfaces, J. Am. Chem. Soc. 133 (2011) 16300–16308. doi:10.1021/ja207297q.
[68] E.D. Minot, A.M. Janssens, I. Heller, H.A. Heering, C. Dekker, S.G. Lemay, Carbon nanotube biosensors: The critical role of the reference electrode, Appl. Phys. Lett. 91 (2007) 1–4. doi:10.1063/1.2775090.
[69] L.M. Malard, M.A. Pimenta, G. Dresselhaus, M.S. Dresselhaus, Raman spectroscopy in graphene, Phys. Rep. 473 (2009) 51–87. doi:10.1016/j.physrep.2009.02.003.

[70] Y. Ahn, J. Kim, S. Ganorkar, Y.-H. Kim, S.-I. Kim, Thermal annealing of graphene to remove polymer residues, Mater. Express. 6 (2016) 69–76. doi:10.1166/mex.2016.1272.
[71] B. Philippe, C.L. D., Ion-Selective Electrodes With Ionophore-Doped Sensing Membranes, Supramol. Chem. (2012). doi:doi:10.1002/9780470661345.smc097.
[72] K. Schmoltner, J. Kofler, A. Klug, E.J.W. List-Kratochvil, Electrolyte-gated organic field-effect transistor for selective reversible ion detection, Adv. Mater. 25 (2013) 6895–6899. doi:10.1002/adma.201303281.
[73] E. Bakker, P. Bühlmann, E. Pretsch, Carrier-based ion-selective electrodes and bulk optodes. 1. General characteristics, Chem. Rev. 97 (1997) 3083–3132. doi:10.1021/cr940394a.
[74] B. Fu, E. Bakker, J.H. Yun, V.C. Yang, M.E. Meyerhoff, Response Mechanism of Polymer Membrane-Based Potentiometric Polyion Sensors, Anal. Chem. 66 (1994) 2250–2259. doi:10.1021/ac00086a009.
[75] B. Li, Y. Noda, L. Hu, H. Yoshikawa, M.M. Matsushita, K. Awaga, Highly efficient organic optoelectronic conversion induced by electric double layers in ionic liquids, Appl. Phys. Lett. 100 (2012). doi:10.1063/1.3697988.
[76] P. Lingenfelter, I. Bedlechowicz-Sliwakowska, T. Sokalski, M. Maj-Zurawska, A. Lewenstam, Time-dependent phenomena in the potential response of ion-selective electrodes treated by the Nernst-Planck-Poisson model. 1. Intramembrane processes and selectivity, Anal. Chem. 78 (2006) 6783–6791. doi:10.1021/ac060264p.
[77] W.-L. Cheng, J.-W. Sue, W.-C. Chen, J.-L. Chang, J.-M. Zen, Activated Nickel Platform for Electrochemical Sensing of Phosphate, Anal. Chem. 82 (2010) 1157–1161. doi:10.1021/ac9025253.
[78] S.R. Dickman, R.H. Br Aa, Colorimetric Determination of Phosphate, Z. Anal. Chem. Am. J. Sci. 112 (1938) 633–339.
[79] P. Avouris, C. Dimitrakopoulos, Graphene: Synthesis and applications, Mater. Today. 15 (2012) 86–97. doi:10.1016/S1369-7021(12)70044-5.
[80] D.C. Marcano, D. V. Kosynkin, J.M. Berlin, A. Sinitskii, Z. Sun, A. Slesarev, L.B. Alemany, W. Lu, J.M. Tour, Improved synthesis of graphene oxide, ACS Nano. 4 (2010) 4806–4814. doi:10.1021/nn1006368.
[81] S. V Tkachev, E.Y. Buslaeva, A. V Naumkin, S.L. Kotova, I. V Laure, S.P. Gubin, Reduced graphene oxide, Inorg. Mater. 48 (2012) 796–802. doi:10.1134/S0020168512080158.
[82] X. Li, W. Cai, J. An, S. Kim, J. Nah, D. Yang, R. Piner, A. Velamakanni, I. Jung, E. Tutuc, S.K. Banerjee, L. Colombo, R.S.Ruoff, Large-Area Synthesis of High-Quality and Uniform Graphene Films on Copper Foils, Science 329 (2009) 1312-1314. doi: 10.1126/science.1171245.
[83] M. Her, R. Beams, L. Novotny, Graphene transfer with reduced residue, Phys. Lett. A. 377 (2013) 1455–1458. doi:http://dx.doi.org/10.1016/j.physleta.2013.04.015.
[84] C. Gong, H.C. Floresca, D. Hinojos, S. McDonnell, X. Qin, Y. Hao, S. Jandhyala, G. Mordi, J. Kim, L. Colombo, R.S. Ruoff, M.J. Kim, K. Cho, R.M. Wallace, Y.J.

Chabal, Rapid selective etching of PMMA residues from transferred graphene by carbon dioxide, J. Phys. Chem. C. 117 (2013) 23000–23008. doi:10.1021/jp408429v.
[85] J.T.W. Wang, J.M. Ball, E.M. Barea, A. Abate, J.A. Alexander-Webber, J. Huang, M. Saliba, I. Mora-Sero, J. Bisquert, H.J. Snaith, R.J. Nicholas, Low-temperature processed electron collection layers of graphene/TiO 2 nanocomposites in thin film perovskite solar cells, Nano Lett. 14 (2014) 724–730. doi:10.1021/nl403997a.
[86] S. Shin, J. Kim, Y.-H. Kim, S.-I. Kim, Enhanced performance of organic light-emitting diodes by using hybrid anodes composed of graphene and conducting polymer, Curr. Appl. Phys. 13 (2013) S144–S147. doi:http://dx.doi.org/10.1016/j.cap.2013.01.016.
[87] T.L. Wu, C.H. Yeh, W.T. Hsiao, P.Y. Huang, M.J. Huang, Y.H. Chiang, C.H. Cheng, R.S. Liu, P.W. Chiu, High-Performance Organic Light-Emitting Diode with Substitutionally Boron-Doped Graphene Anode, ACS Appl. Mater. Interfaces. 9 (2017) 14998–15004. doi:10.1021/acsami.7b03597.
[88] Y. Liu, X. Dong, P. Chen, Biological and chemical sensors based on graphene materials, Chem. Soc. Rev. (2012). doi:10.1039/C1CS15270J.
[89] J. Du, L. Zhao, Y. Zeng, L. Zhang, F. Li, P. Liu, C. Liu, Comparison of electrical properties between multi-walled carbon nanotube and graphene nanosheet/high density polyethylene composites with a segregated network structure, Carbon N. Y. 49 (2011) 1094–1100. doi:http://dx.doi.org/10.1016/j.carbon.2010.11.013.
[90] S. Sando, B. Zhang, T. Cui, A low-cost and label-free alpha-fetoprotein sensor based on self-assembled graphene on shrink polymer, in: Proc. IEEE Int. Conf. Micro Electro Mech. Syst., 2015. doi:10.1109/MEMSYS.2015.7050954.
[91] H. Xu, Z. Zhang, H. Xu, Z. Wang, S. Wang, L.M. Peng, Top-gated graphene field-effect transistors with high normalized transconductance and designable dirac point voltage, ACS Nano. 5 (2011) 5031–5037. doi:10.1021/nn201115p.
[92] K.N. Houk, C.A. Hunter, M.J. Krische, J.-M. Lehn, S. V Ley, M. Olivucci, J. Thiem, M. Venturi, P. Vogel, C.-H. Wong, H. Wong, H. Yamamoto, Topics in Current Chemistry, (n.d.).
[93] G. Wulff, Molecular Imprinting in Cross-Linked Materials with the Aid of Molecular Templates— A Way towards Artificial Antibodies, Angew. Chemie Int. Ed. English. (1995). doi:10.1002/anie.199518121.
[94] J. Kim, Layer-Resolved Graphene Transfer via, Science (80-.). 833 (2014) 833–837. doi:10.1126/science.1242988.
[95] J.W. Suk, A. Kitt, C.W. Magnuson, Y. Hao, S. Ahmed, J. An, A.K. Swan, B.B. Goldberg, R.S. Ruoff, Transfer of CVD-grown monolayer graphene onto arbitrary substrates, ACS Nano. (2011). doi:10.1021/nn201207c.
[96] S. Gorantla, A. Bachmatiuk, J. Hwang, H.A. Alsalman, J.Y. Kwak, T. Seyller, J. Eckert, M.G. Spencer, M.H. Rummeli, A universal transfer route for graphene, Nanoscale. 6 (2014) 889–896. doi:10.1039/C3NR04739C.
[97] H. Kim, B. Yoon, J. Sung, D.-G. Choi, C. Park, Micropatterning of thin P3HT films via plasma enhanced polymer transfer printing, (n.d.). doi:10.1039/b807285j.

[98] C. Warwick, A. Guerreiro, E. Wood, J. Kitson, J. Robinson, A. Soares, A molecular imprinted polymer based sensor for measuring phosphate in wastewater samples, Water Sci. Technol. 69 (2014) 48 LP – 54. http://wst.iwaponline.com/content/69/1/48.abstract.
[99] C. Warwick, A. Guerreiro, A. Gomez-Caballero, E. Wood, J. Kitson, J. Robinson, A. Soares, Conductance based sensing and analysis of soluble phosphates in wastewater, Biosens. Bioelectron. (2014). doi:10.1016/j.bios.2013.08.048.
[100] R. Ahmad, N. Tripathy, Y.-B. Hahn, High-performance cholesterol sensor based on the solution-gated field effect transistor fabricated with ZnO nanorods, Biosens. Bioelectron. 45 (2013) 281–286. doi:http://dx.doi.org/10.1016/j.bios.2013.01.021.
[101] Q. Zhang, F. Wei, S. Zhang, J.-Q. Huang, H.-J. Peng, X.-Y. Liu, W.-Z. Qian, Showcasing research from Prof Title: Ionic shield for polysulfi des towards highly-stable lithium–sulfur batteries As featured in: Ionic shield for polysulfides towards highly-stable lithium–sulfur batteries, (n.d.). www.rsc.org/ees.
[102] A.C. Ferrari, J.C. Meyer, V. Scardaci, C. Casiraghi, M. Lazzeri, F. Mauri, S. Piscanec, D. Jiang, K.S. Novoselov, S. Roth, A.K. Geim, Raman spectrum of graphene and graphene layers, Phys. Rev. Lett. 97 (2006) 1–4. doi:10.1103/PhysRevLett.97.187401.
[103] S.B. Papp, K.S. Choi, H. Deng, P. Lougovski, S.J. van Enk, H.J. Kimble, Characterization of Multipartite Entanglement for One Photon Shared Among Four Optical Modes, Science (80-.). (2009). doi:10.1126/science.1172260.
[104] W. Regan, N. Alem, B. Alemán, B. Geng, Ç. Girit, L. Maserati, F. Wang, M. Crommie, A. Zettl, A direct transfer of layer-area graphene, Appl. Phys. Lett. 96 (2010) 2008–2011. doi:10.1063/1.3337091.
[105] R. Suedee, W. Intakong, F.L. Dickert, Molecularly imprinted polymer-modified electrode for on-line conductometric monitoring of haloacetic acids in chlorinated water, Anal. Chim. Acta. 569 (2006) 66–75. doi:http://dx.doi.org/10.1016/j.aca.2006.03.081.
[106] G.T. Nagami, Hipercloremia: por qué y cómo, Nefrologia. 36 (2016) 347–353. doi:10.1016/j.nefro.2016.04.001.
[107] M. Lyczewska, M. Wojciechowski, E. Bulska, E.A.H. Hall, K. Maksymiuk, A. Michalska, Chloride-selective electrodes with poly(n-butyl acrylate) based membranes, Electroanalysis. 19 (2007) 393–397. doi:10.1002/elan.200603721.
[108] J. Kim, L. Wang, T. Bourouina, T. Cui, Ion sensitive field effect transistor based on graphene and ionophore hybrid membrane for phosphate detection, Microsyst. Technol. 25 (2019). doi:10.1007/s00542-018-4200-z.
[109] A. Jernelöv, H. Lann, A. Jernelov, Mercury Accumulation in Food Chains, Oikos. 22 (1971) 403. doi:10.2307/3543865.
[110] R.A. Bernhoft, Mercury toxicity and treatment: A review of the literature, J. Environ. Public Health. 2012 (2012). doi:10.1155/2012/460508.
[111] M.P. Da Silva, J.R. Procopio, L. Hernández, Reversed-phase high-performance liquid chromatography of pyrrolidinedithiocarbamate complexes of mercuric species

using amperometric and coulometric detection, J. Chromatogr. A. 761 (1997) 139–146. doi:10.1016/S0021-9673(96)00821-7.
[112] H. Wu, C. Fang, B. Du, C. Zhao, Original Paper Flow injection on-line preconcentration coupled to hydride generation atomic fluorescence spectrometry for ultra-trace amounts of cadmium determination in seawater, (2008) 173–178. doi:10.1007/s00604-007-0808-x.
[113] N.A. Panichev, S.E. Panicheva, Determination of total mercury in fish and sea products by direct thermal decomposition atomic absorption spectrometry, Food Chem. 166 (2015) 432–441. doi:10.1016/j.foodchem.2014.06.032.
[114] C. Wan, C. Chen, S. Jiang, Determination of Mercury Compounds in Water Samples by Liquid Chromatography – Inductively Coupled Plasma Mass Spectrometry With an In Situ Nebulizer / Vapor Generator, 12 (1997) 683–687.
[115] S.J. Hecnar, Acute and chronic toxicity of ammonium nitrate fertilizer to amphibians from southern ontario, Environ. Toxicol. Chem. 14 (1995) 2131–2137. doi:10.1002/etc.5620141217.
[116] J.W. Blum, C. Morel, H.M. Hammon, R.M. Bruckmaier, A. Jaggy, A. Zurbriggen, T. Jungi, High constitutional nitrate status in young cattle, Comp. Biochem. Physiol. - A Mol. Integr. Physiol. 130 (2001) 271–282. doi:10.1016/S1095-6433(01)00390-7.
[117] B.T. Croll, C.R. Hayes, Nitrate and water supplies in the United Kingdom, Environ. Pollut. 50 (1988) 163–187. doi:10.1016/0269-7491(88)90190-X.
[118] A. Elmidaoui, F. Elhannouni, M.A. Menkouchi Sahli, L. Chay, H. Elabbassi, M. Hafsi, D. Largeteau, Pollution of nitrate in Moroccan ground water: Removal by electrodialysis, Desalination. 136 (2001) 325–332. doi:10.1016/S0011-9164(01)00195-3.
[119] M.F. Khanfar, W. Al-Faqheri, A. Al-Halhouli, Low cost lab on chip for the colorimetric detection of nitrate in mineral water products, Sensors (Switzerland). 17 (2017) 1–9. doi:10.3390/s17102345.
[120] K.K. Choi, K.W. Fung, Determination of nitrate and nitrite in meat products by using a nitrate ion-selective electrode, Analyst. 105 (1980) 241–245. doi:10.1039/an9800500241.
[121] H. Masuda, M. Satoh, Fabrication of gold nanodot array using anodic porous alumina as an evaporation mask, Japanese J. Appl. Physics, Part 2 Lett. 35 (1996). doi:10.1143/JJAP.35.L126.
[122] S.Y. Yang, I. Ryu, H.Y. Kim, J.K. Kim, S.K. Jang, T.P. Russell, Nanoporous membranes with ultrahigh selectivity and flux for the filtration of viruses, Adv. Mater. 18 (2006) 709–712. doi:10.1002/adma.200501500.
[123] G. Gorokh, A. Mozalev, D. Solovei, V. Khatko, E. Llobet, X. Correig, Anodic formation of low-aspect-ratio porous alumina films for metal-oxide sensor application, Electrochim. Acta. 52 (2006) 1771–1780. doi:10.1016/j.electacta.2006.01.081.
[124] Q. Wang, W. Han, Y. Wang, M. Lu, L. Dong, Tape nanolithography: a rapid and simple method for fabricating flexible, wearable nanophotonic devices, Microsystems Nanoeng. 4 (2018). doi:10.1038/s41378-018-0031-4.

[125] D. Chen, W. Zhao, T.P. Russell, P3HT nanopillars for organic photovoltaic devices nanoimprinted by AAO templates, ACS Nano. 6 (2012) 1479–1485. doi:10.1021/nn2043548.
[126] S. Kim, S. Shin, T. Kim, H. Du, M. Song, C.W. Lee, K. Kim, S. Cho, D.H. Seo, S. Seo, Robust graphene wet transfer process through low molecular weight polymethylmethacrylate, Carbon N. Y. 98 (2016) 352–357. doi:10.1016/j.carbon.2015.11.027.
[127] C. Carey, Plasticizer effects in the PVC membrane of the dibasic phosphate selective electrode, Chemosensors. 3 (2015) 284–294. doi:10.3390/chemosensors3040284.
[128] K. Melzer, A.M. Münzer, E. Jaworska, K. Maksymiuk, A. Michalska, G. Scarpa, Selective ion-sensing with membrane-functionalized electrolyte-gated carbon nanotube field-effect transistors, Analyst. 139 (2014) 4947–4954. doi:10.1039/c4an00714j.
[129] I. Alessandri, J.R. Lombardi, Enhanced Raman Scattering with Dielectrics, Chem. Rev. 116 (2016) 14921–14981. doi:10.1021/acs.chemrev.6b00365.
[130] U. Schaller, E. Bakker, U.E. Spichiger, E. Pretsch, Ionic Additives for Ion-Selective Electrodes Based on Electrically Charged Carriers, Anal. Chem. 66 (1994) 391–398. doi:10.1021/ac00075a013.
[131] J. Kim, Q. Liu, T. Cui, Solution-gated nitrate sensitive field effect transistor with hybrid film: CVD graphene/polymer selective membrane, Org. Electron. 78 (2020) 105551. doi:10.1016/j.orgel.2019.105551.
[132] J.M.S. Pearce, A brief history of the clinical thermometer, QJM An Int. J. Med. 95 (2002) 251–252. doi:10.1093/qjmed/95.4.251.
[133] H. Rodríguez, M. Williams, J.S. Wilkes, R.D. Rogers, Ionic liquids for liquid-in-glass thermometers, Green Chem. 10 (2008) 501–507. doi:10.1039/B800366A.
[134] M. Harada, Minamata Disease: Methylmercury Poisoning in Japan Caused by Environmental Pollution, Crit. Rev. Toxicol. 25 (1995) 1–24. doi:10.3109/10408449509089885.
[135] G. Bosson, F. Gutmann, L.M. Simmons, A Relationship between Resistance and Temperature of Thermistors, J. Appl. Phys. 21 (1950) 1267–1268. doi:10.1063/1.1699586.
[136] Y. Zhu, S. Murali, W. Cai, X. Li, J.W. Suk, J.R. Potts, R.S. Ruoff, Graphene and Graphene Oxide: Synthesis, Properties, and Applications, Adv. Mater. 22 (2010) 3906–3924. doi:10.1002/adma.201001068.
[137] X. Li, H. Zhu, K. Wang, A. Cao, J. Wei, C. Li, Y. Jia, Z. Li, X. Li, D. Wu, Graphene-On-Silicon Schottky Junction Solar Cells, Adv. Mater. 22 (2010) 2743–2748. doi:10.1002/adma.200904383.
[138] S.S. Li, K.H. Tu, C.C. Lin, C.W. Chen, M. Chhowalla, Solution-processable graphene oxide as an efficient hole transport layer in polymer solar cells, ACS Nano. 4 (2010) 3169–3174. doi:10.1021/nn100551j.

[139] B.R. Lee, J.W. Kim, D. Kang, D.W. Lee, S.J. Ko, H.J. Lee, C.L. Lee, J.Y. Kim, H.S. Shin, M.H. Song, Highly efficient polymer light-emitting diodes using graphene oxide as a hole transport layer, ACS Nano. 6 (2012) 2984–2991. doi:10.1021/nn300280q.
[140] J. Kim, Q. Liu, T. Cui, Solution-gated ion-sensitive field effect transistor with polymer selective membrane for nitrate detection, in: ASME Int. Mech. Eng. Congr. Expo. Proc., 2018. doi:10.1115/IMECE2018-87918.
[141] T. Ono, Y. Kanai, K. Inoue, Y. Watanabe, S.I. Nakakita, T. Kawahara, Y. Suzuki, K. Matsumoto, Electrical Biosensing at Physiological Ionic Strength Using Graphene Field-Effect Transistor in Femtoliter Microdroplet, Nano Lett. 19 (2019) 4004–4009. doi:10.1021/acs.nanolett.9b01335.
[142] F. Xing, Z.B. Liu, Z.C. Deng, X.T. Kong, X.Q. Yan, X.D. Chen, Q. Ye, C.P. Zhang, Y.S. Chen, J.G. Tian, Sensitive real-time monitoring of refractive indexes using a novel graphene-based optical sensor, Sci. Rep. 2 (2012) 1–7. doi:10.1038/srep00908.
[143] L. Wang, J. Kim, T. Cui, Self-assembled graphene and copper nanoparticles composite sensor for nitrate determination, Microsyst. Technol. 24 (2018) 3623–3630. doi:10.1007/s00542-018-3792-7.
[144] Z. Qian, Y. Hui, F. Liu, S. Kang, S. Kar, M. Rinaldi, Graphene–Aluminum nitride NEMS resonant infrared detector, Microsystems Nanoeng. 2 (2016). doi:10.1038/micronano.2016.26.
[145] J.C. Meyer, A.K. Geim, M.I. Katsnelson, K.S. Novoselov, T.J. Booth, S. Roth, The structure of suspended graphene sheets, Nature. 446 (2007) 60–63. doi:10.1038/nature05545.
[146] E. Choudhary, V. Szalai, Two-step cycle for producing multiple anodic aluminum oxide (AAO) films with increasing long-range order, RSC Adv. 6 (2016) 67992–67996. doi:10.1039/c6ra13830f.
[147] V. Skákalová, A.B. Kaiser, J.S. Yoo, D. Obergfell, S. Roth, Correlation between resistance fluctuations and temperature dependence of conductivity in graphene, Phys. Rev. B. 80 (2009) 153404. doi:10.1103/PhysRevB.80.153404.
[148] X.-Y. Fang, X.-X. Yu, H.-M. Zheng, H.-B. Jin, L. Wang, M.-S. Cao, Temperature- and thickness-dependent electrical conductivity of few-layer graphene and graphene nanosheets, Phys. Lett. A. 379 (2015) 2245–2251. doi:https://doi.org/10.1016/j.physleta.2015.06.063.
[149] D. Yoon, Y.W. Son, H. Cheong, Negative thermal expansion coefficient of graphene measured by raman spectroscopy, Nano Lett. 11 (2011) 3227–3231. doi:10.1021/nl201488g.
[150] N. Mounet, N. Marzari, First-principles determination of the structural, vibrational and thermodynamic properties of diamond, graphite, and derivatives, Phys. Rev. B. 71 (2005) 205214. doi:10.1103/PhysRevB.71.205214.
[151] W. Gao, R. Huang, Thermomechanics of monolayer graphene: Rippling, thermal expansion and elasticity, J. Mech. Phys. Solids. 66 (2014) 42–58. doi:10.1016/j.jmps.2014.01.011.

[152] P.L. de Andres, F. Guinea, M.I. Katsnelson, Bending modes, anharmonic effects, and thermal expansion coefficient in single-layer and multilayer graphene, Phys. Rev. B. 86 (2012) 144103. doi:10.1103/PhysRevB.86.144103.
[153] U. Sassi, R. Parret, S. Nanot, M. Bruna, S. Borini, D. De Fazio, Z. Zhao, E. Lidorikis, F.H.L. Koppens, A.C. Ferrari, A. Colli, Graphene-based mid-infrared room-temperature pyroelectric bolometers with ultrahigh temperature coefficient of resistance, Nat. Commun. 8 (2017) 14311. https://doi.org/10.1038/ncomms14311.
[154] X. Zhang, L. Wang, J. Xin, B.I. Yakobson, F. Ding, Role of hydrogen in graphene chemical vapor deposition growth on a copper surface, J. Am. Chem. Soc. 136 (2014) 3040–3047. doi:10.1021/ja405499x.
[155] T.H. Han, Y. Lee, M.R. Choi, S.H. Woo, S.H. Bae, B.H. Hong, J.H. Ahn, T.W. Lee, Extremely efficient flexible organic light-emitting diodes with modified graphene anode, Nat. Photonics. 6 (2012) 105–110. doi:10.1038/nphoton.2011.318.
[156] J. Kim, S. Ganorkar, J. Choi, Y.H. Kim, S. Il Kim, Fabrication of well-ordered, anodic aluminum oxide membrane using hybrid anodization, J. Nanosci. Nanotechnol. 17 (2017) 761–765. doi:10.1166/jnn.2017.12572.
[157] A.N. Sidorov, G.W. Sławiński, A.H. Jayatissa, F.P. Zamborini, G.U. Sumanasekera, A surface-enhanced Raman spectroscopy study of thin graphene sheets functionalized with gold and silver nanostructures by seed-mediated growth, Carbon N. Y. 50 (2012) 699–705. doi:10.1016/j.carbon.2011.09.030.
[158] P. Sahatiya, S.K. Puttapati, V.V.S.S. Srikanth, S. Badhulika, Graphene-based wearable temperature sensor and infrared photodetector on a flexible polyimide substrate, Flex. Print. Electron. 1 (2016). doi:10.1088/2058-8585/1/2/025006.
[159] B. Abad, J. Maiz, M. Martin-Gonzalez, Rules to Determine Thermal Conductivity and Density of Anodic Aluminum Oxide (AAO) Membranes, J. Phys. Chem. C. 120 (2016) 5361–5370. doi:10.1021/acs.jpcc.6b00643.
[160] Y. Peng, G. Jing, T. Cui, A hybrid physical-chemical deposition process at ultra-low temperatures for high-performance perovskite solar cells, J. Mater. Chem. A. 3 (2015) 12436–12442. doi:10.1039/c5ta01730k.
[161] J. Zhang, L.J. Xu, P. Huang, Y. Zhou, Y.Y. Zhu, N.Y. Yuan, J.N. Ding, Z.G. Zhang, Y.F. Li, A simple and dopant-free hole-transporting material based on (2-ethylhexyl)-9H-carbazole for efficient planar perovskite solar cells, J. Mater. Chem. C. 5 (2017) 12752–12757. doi:10.1039/c7tc03683c.
[162] D. Yang, R. Yang, S. Priya, S. (Frank) Liu, Recent Advances in Flexible Perovskite Solar Cells: Fabrication and Applications, Angew. Chemie - Int. Ed. 58 (2019) 4466–4483. doi:10.1002/anie.201809781.
[163] A. Elschner, F. Bruder, H.W. Heuer, F. Jonas, A. Karbach, S. Kirchmeyer, S. Thurm, R. Wehrmann, PEDT/PSS for efficient hole-injection in hybrid organic light-emitting diodes, Synth. Met. 111 (2000) 139–143. doi:10.1016/S0379-6779(99)00328-8.
[164] B. Ecker, J.C. Nolasco, J. Pallarés, L.F. Marsal, J. Posdorfer, J. Parisi, E. Von Hauff, Degradation effects related to the hole transport layer in organic solar cells, Adv. Funct. Mater. 21 (2011) 2705–2711. doi:10.1002/adfm.201100429.

[165] C. Xu, Z. Liu, E.C. Lee, High-performance metal oxide-free inverted perovskite solar cells using poly(bis(4-phenyl)(2,4,6-trimethylphenyl)amine) as the hole transport layer, J. Mater. Chem. C. 6 (2018) 6975–6981. doi:10.1039/C8TC02241K.